

ABSTRACT

Title of Thesis: THE EFFECT OF LASER SHOCK PEENING
ON DISLOCATION MORPHOLOGY AND
MICROSTRUCTURAL EVOLUTION OF
AA5083-H116

Alice Uanchian Tsao, Master of Science, 2019

Thesis Directed By: Professor Sreeramamurthy Ankem
Department of Materials Science and Engineering,

The AA5083-H116 aluminum alloys (Al-4.7Mg-0.62Mn-0.29Fe-0.15Si-0.099Cr-0.094Zn-0.036Cu-0.018Ti-0.086Other) are lightweight structural materials for marine applications. Due to the high magnesium content ($> 3\text{wt.}\%$), the sensitization of Al_3Mg_2 β -phase and susceptibility for intergranular stress corrosion cracking (IGSCC) in AA5083-H116 significantly increases under thermal exposure. The effects of laser-shock peening (LSP) on the kinetics of β -phase were studied via accelerated sensitization heat treatments between 70-175°C for times between 5-3,600 hours. Optical microscopy, transmission electron microscopy (TEM), and finite element method (FEM) modeling were utilized to study the effect of LSP on AA5083-H116 microstructural evolution, dislocation morphology, and stress-strain distribution. FEM results showed LSP induces plastic compressive deformation near the surface. TEM observations confirmed the models, showing dislocation density increased by a

factor of ~ 4.7 , with residual tensile stresses throughout the thickness. The kinetics of β -phase precipitation and coarsening were not impacted by LSP; however, it is recommended that its influence on IGSCC should be investigated further.

THE EFFECT OF LASER SHOCK PEENING ON DISLOCATION
MORPHOLOGY AND MICROSTRUCTURAL EVOLUTION OF AA5083-H116

by

Alice Uanchian Tsao

Thesis submitted to the Faculty of the Graduate School of the
University of Maryland, College Park, in partial fulfillment
of the requirements for the degree of
Master of Science
2019

Advisory Committee:

Professor Sreeramamurthy Ankem, Chair; University of Maryland
Professor Mohamad Al-Sheikhly; University of Maryland
Dr. Matthew Draper; Naval Surface Warfare Center Carderock Division

© Copyright by
Alice Uanchian Tsao
2019

Acknowledgements

The journey of this research study was both joyful and challenging, where sometimes the research went smoothly without any problem and sometimes there were obstacles that took weeks to resolve. However, with the numerous help, guidance, and support from all the people I have encountered during this project, I was able to successfully complete my research. This research not only enriched me with the knowledge related to the laser shock peening process on AA5083-H116 but also provided me the skills to become a better researcher. Therefore, I would like to first express my sincere gratitude to Naval Surface Warfare Center (NSWC) for supporting and funding this research under the contract number N0016719P0129. Without this project, I would not be able to pursue my master's degree. Moreover, I would like to thank Dr. Charles Roe and the NSWC personnel for their interest, assistance, and encouragement during this research.

Second, I would also like to express my sincere gratitude to my esteemed advisor, Dr. Sreeramamurthy Ankem for his endless support, guidance, and encouragement throughout this research.

Third, I would like to acknowledge the contribution of transmission electron microscopy sample preparation, imaging and analysis by Dr. Ramasis Goswami at the U.S. Naval Research Laboratory.

Fourth, I would like to thank Dr. Matthew Draper, Dr. Samuel Schwarm, Dr. Matthew McMahon, and Matthew Frichtl for their help and guidance during this project.

Fifth, I would like to show my greatest appreciation to John Galuardi for all the help, discussions, and debates during this research, for supporting and believing in me the entire time throughout this research, and for editing my thesis.

Sixth, I would like to express my gratitude to my committee members for taking their time to review and provide insightful comments and suggestions to this thesis.

Seventh, I would like to thank all the people I have encountered during this project. Without their help, this thesis would not have been possible.

Last but not least, I would like to express my deepest gratitude to my mother, Angela Lee, my father, Tsanyeh Tsao, and my brother, Bojiun Tsao for all the continuous support, numerous discussions, and endless love and encouragement throughout my entire life and during this research. Because of them, I can reach and achieve my goals. I would also like to thank my parents for their financial support throughout my entire education years. Thank you!

Table of Contents

Acknowledgements.....	ii
Table of Contents.....	iv
List of Tables	vi
List of Figures.....	vii
Chapter 1: Introduction.....	1
Chapter 2: Literature Review.....	7
• 2.1. Brief Overview of Aluminum.....	7
• 2.2. Aluminum Alloys.....	8
• 2.3. AA5083-H116 Background Information.....	12
• 2.4. Sensitization of 5xxx Series Aluminum Alloys.....	14
• 2.5. Magnesium Segregation and Enrichment.....	14
• 2.6. Al ₃ Mg ₂ Beta (β) Phase	16
• 2.7. Laser Shock Peening Technology.....	20
Chapter 3: Experimental Methods and Results.....	22
• 3.1. Testing Materials	22
• 3.2. Laser Shock Peening Process.....	25
• 3.3. Heat Treatments.....	26
• 3.4. Material Characterization.....	30
○ 3.4.1. <i>Optical Microscopy</i>	30
○ 3.4.2. <i>Optical Microscopy Results</i>	33
○ 3.4.3. <i>Average Grain Size Measurement</i>	39
○ 3.4.4. <i>Average Grain Size Measurement Results</i>	42
○ 3.4.5. <i>Transmission Electron Microscopy (TEM)</i>	45
○ 3.4.6. <i>Transmission Electron Microscopy Results</i>	48
○ 3.4.7. <i>Dislocation Density Measurement</i>	51
○ 3.4.8. <i>Dislocation Density Measurement Results</i>	52
Chapter 4: Finite Element Method (FEM) Modeling.....	53

- 4.1. Assumptions and Modeling Procedures..... 53
- 4.2. Validation..... 67
 - 4.2.1. *Test 1: Elastic Modulus Check (Large Region)*..... 67
 - 4.2.2. *Test 2: Zero Deformation, Stress, and Strain Check (Large Region)* 69
 - 4.2.3. *Test 3: Zero Deformation, Stress, and Strain Check (Small Region)* 71
- 4.3. Results..... 73
 - 4.3.1. *Step 1 Results: Force Applied at the Center* 74
 - 4.3.2. *Step 2 Results: Force Applied at the Center then Surrounding*..... 81
 - 4.3.3. *Step 3 Results: Force Applied at the Center, then Surrounding, and Back to Center*..... 87
 - 4.3.4. *Step 4 Results: Force Applied at the Center, then Surrounding, Back to Center and Back to Surrounding* 94
 - 4.3.5. *Summary of All FEM Results*..... 102
- Chapter 5: Discussion 106
 - 5.1. Optical Microscopy..... 106
 - 5.2. Transmission Electron Microscopy 107
 - 5.2.1. *Thermal Effect from Laser Shock Peening Process*..... 107
 - 5.2.2. *Al₃Mg₂ β Phase Precipitates* 108
 - 5.2.3. *Dislocation Morphology* 109
 - 5.3. Finite Element Method Modeling..... 110
- Chapter 6: Conclusions 115
 - 6.1. Summary and Conclusions 115
 - 6.2. Future Works 119
- Chapter 7: References..... 121

List of Tables

Table 1. Aluminum wrought alloy series and its principal alloying element.	8
Table 2. Aluminum casting alloy series and its principal alloying element.	8
Table 3. Chemical composition of AA5083.....	13
Table 4. Mechanical properties of AA5083.....	13
Table 5. Dimensions of testing samples.....	24
Table 6. Average chemical composition of AA5083-H116.....	24
Table 7. Reported initial time for each β phase morphology to appear at each temperature.....	27
Table 8. Sample sensitizing temperature and time and sample ID	29
Table 9. Grain size measurements for laser shock peened and unpeened samples....	43
Table 10. Average dislocation density of U10 and P18.....	52
Table 11. List of software used and the purpose for the FEM modeling.....	54
Table 12. Dimensions of the actual and modeling sample and the laser shock peening affected area.....	56
Table 13. Inputted AA5083 – H116 mechanical properties.....	57
Table 14. Applied force and corresponding time for Step 1 to Step 4.....	63
Table 15. Validation test 1 FEM results.....	68
Table 16. FEM results of step 1 in the loading condition.....	74
Table 17. FEM results of Step 1 in the unloading condition.....	78
Table 18. FEM results of Step 2 in the loading condition.....	81
Table 19. FEM results of Step 2 in the unloading condition.....	84
Table 20. FEM results of Step 3 in the loading condition.....	87
Table 21. FEM results of Step 3 in the unloading condition.....	91
Table 22. FEM results of Step 4 in the loading condition.....	94
Table 23. FEM results of Step 4 in the unloading condition.....	98
Table 24. FEM results for all steps loading and unloading conditions.....	102

List of Figures

Figure 1. Binary phase diagram of aluminum and magnesium.	16
Figure 2. AA5083-H131 β phase morphology evolution at 175 °C. (a) Unaged β phase, (b) Discontinuous β phase at 1 hour of ageing time, (c) Semi-continuous β phase at 50 hours of ageing time, (d) Continuous β phase at 240 hours of aging time.....	19
Figure 3. Laser shock peening process.	21
Figure 4. (a) As-received laser shock peened AA5083-H116 samples, (b) As-received no laser shock peened AA5083-H116 samples, and (c) Total 28 AA5083-H116 samples with 18 laser shock peened samples (left) and 10 no laser shock peened samples (right).....	23
Figure 5. Two layers application for laser shock peening process.	26
Figure 6. Thermo Scientific Thermolyne furnace FB1400 at UMD. (a) Furnace 1 (F1) and Furnace 2 (F2) from left to right and (b) Furnace 3 to Furnace 6 (F3 to F6) from right to left.	28
Figure 7. Sample cutting directions: Longitudinal (L) – rolling direction, Transverse (T) direction, and Short transverse (S) direction.	30
Figure 8. Schematic view of sample under the optical microscope.....	32
Figure 9. Al_3Mg_2 β phase increases as the aging temperature increases and under a constant aging time. (a) Sample U3 aged at 100 °C for 168 hours. (b) Sample U7 aged at 150 °C for 168 hours	34
Figure 10. Al_3Mg_2 β phase increases as the aging time increases and under the same aging temperature. (a) Sample U3 aged at 100 °C for 168 hours. (b) Sample U4 aged at 100 °C for 550 hours. c) Sample U5 aged at 100 °C for 1100 hours.	34
Figure 11. Al_3Mg_2 β phase increases as the aging temperature increases and under a constant aging time. (a) Sample P4 aged at 100 °C for 168 hours. (b) Sample P13 aged at 150 °C for 168 hours.....	35
Figure 12. Al_3Mg_2 β phase increases as the aging time increases and under the same aging temperature. (a) Sample P4 aged at 100 °C for 168 hours. (b) Sample	

P6 aged at 100 °C for 550 hours. (c) Sample P8 aged at 100 °C for 1100 hours.	35
Figure 13. Pre-existing Al ₃ Mg ₂ β phase. (a) Sample P18 unaged and laser shock peened. (b) Sample U10 unaged and not laser shock peened.	36
Figure 14. Grain size and morphology variations in the sample. (a) Grains appear to have a more circular and equiaxial shape near the sample surface region. (b) Grains appear to have a more elongated and oblong shape in the sample middle region.....	37
Figure 15. Grain size and morphology variations in both laser shock peened and unpeened samples. (a) Sample P7 near the sample surface region. (b) Sample P7 in the sample middle region. (c) Sample U2 near the sample surface region. (d) Sample U2 in the sample middle region.....	38
Figure 16. (a) Planimetric Method. Measures the grain size by counting the number of grains inside (blue) and on (green) the drawn circle (red). (b) Circular Intercept Method. Measures the grain size by counting the number of grain boundaries intercept (blue) the three drawn circles (red).....	41
Figure 17. (a) TEM brightfield dislocation image for U10 sample with a [112] zone axis. (b) TEM brightfield dislocation image for P18 sample with a [011] zone axis.	48
Figure 18. (a) Randomly orientated dislocations for sample U10. (b) Preferential dislocations direction (marked with red arrow) for sample P18.	49
Figure 19. (a) Al-Mn-Fe type of dispersoids pinned dislocation in the U10 sample. (b) Fine Al ₃ Mg ₂ β phase precipitates on dislocation.	50
Figure 20. Melt pool from the penetration of laser beam appears in the P18 sample surface.	50
Figure 21. Dislocation density measurement by using the line-intercept method.	51
Figure 22. The array of circles appears on the laser shock peened sample surface. The diameter of each circle is about 6.35mm (0.25in).....	54
Figure 23. The actual sample and the modeling sample. The modeling sample is 1/8 of the actual sample. The diameter of the laser shock peening affected area is 6.35mm (0.25in).	55

Figure 24. AA5083-H116 engineering stress – strain curve.....	58
Figure 25. Mesh application and mesh size distribution.....	59
Figure 26. Model constraints.	60
Figure 27. Two-layer laser shock peening process in four steps.	62
Figure 28. Graphical representations of applied force (N) and corresponding time (s) for Step 1 to Step 4.	65
Figure 29. Validation Test 1: Z stress result.	69
Figure 30. Validation Test 1: Z strain result.	69
Figure 31. Validation Test 2: Deformation in Z direction after the load is removed.	70
Figure 32. Validation Test 2: Stress in Z direction after the load is removed.	70
Figure 33. Validation Test 2: Strain in Z direction after the load is removed.	70
Figure 34. Force applied at a small region.	71
Figure 35. Validation Test 3: Deformation in Z direction after the load is removed.	71
Figure 36. Validation Test 3: Stress in Z direction after the load is removed.	72
Figure 37. Validation Test 3: Strain in Z direction after the load is removed.	72
Figure 38. YZ section plane and place of insertion.	74
Figure 39. FEM results for Step 1 loading condition. (a) Z direction displacement, (b) Z direction displacement section view, (c) Z stress, (d) Z stress section view, (e) Z strain, (f) Z strain section view, (g) von-Mises stress, and (h) von-Mises stress section view.	77
Figure 40. FEM results for Step 1 unloading condition. (a) Z direction displacement, (b) Z direction displacement section view, (c) Z strain, (d) Z strain section view, (e) von-Mises stress, and (f) von-Mises stress section view.	80
Figure 41. FEM results for Step 2 loading condition. (a) Z direction displacement, (b) Z direction displacement section view, (c) Z stress, (d) Z stress section view, (e) Z strain, (f) Z strain section view, (g) von-Mises stress, and (h) von-Mises stress section view.	84
Figure 42. FEM results for Step 2 unloading condition. (a) Z direction displacement, (b) Z direction displacement section view, (c) Z strain, (d) Z strain section view, (e) von-Mises stress, and (f) von-Mises stress section view.	87

Figure 43. FEM results for Step 3 loading condition. (a) Z direction displacement, (b) Z direction displacement section view, (c) Z stress, (d) Z stress section view, (e) Z strain, (f) Z strain section view, (g) von-Mises stress, and (h) von-Mises stress section view. 90

Figure 44. FEM results for Step 3 unloading condition. (a) Z direction displacement, (b) Z direction displacement section view, (c) Z strain, (d) Z strain section view, (e) von-Mises stress, and (f) von-Mises stress section view. 93

Figure 45. FEM results for Step 4 loading condition. (a) Z direction displacement, (b) Z direction displacement section view, (c) Z stress, (d) Z stress section view, (e) Z strain, (f) Z strain section view, (g) von-Mises stress, (h) von-Mises stress section view, (i) Hydrostatic stress, and (j) Hydrostatic stress section view. 97

Figure 46. FEM results for Step 4 unloading condition. (a) Z direction displacement, (b) Z direction displacement section view, (c) Z strain, (d) Z strain section view, (e) von-Mises stress, (f) von-Mises stress section view, (g) Hydrostatic stress, and (h) Hydrostatic stress section view. 101

Figure 47. Tensile and compressive residual stress distribution..... 112

Figure 48. Graphical representations of (a) hydrostatic stress, (b) Z-direction strain, and (c) von-Mises stress changed through the sample thickness with the elastic and plastic deformation interaction. 114

Chapter 1: Introduction

Aluminum alloys are highly attractive to many different industries due to their high strength-to-weight ratio and adjustable chemical compositions. This thesis will mainly focus on the 5xxx series of aluminum alloys, specifically the 5083-H116 aluminum alloy. The 5xxx series aluminum alloys are great structural materials that have been widely used in many lightweight applications, especially marine applications. The 5xxx series has great corrosion resistance, mechanical properties, weldability, and formability due to a high magnesium content (4.0 wt. % to 4.9 wt. %). The drawback of high percentage of magnesium content (> 3 wt. %) in the aluminum alloys is sensitization of Al_3Mg_2 beta (β) phase. Sensitization can easily occur under thermal exposure and increase the susceptibility to intergranular corrosion (IGC) and intergranular stress corrosion cracking (IGSCC) in a corrosive sea water [1-3]. These intergranular attacks in sea water are strongly associated with the Al_3Mg_2 β phase formation along the grain boundaries [2]. Al_3Mg_2 β phase has a high selective-dissolution rate in chloride solutions, such as sea water, due to the β phase's anodic behavior with the aluminum matrix [2, 3]. The effective sensitization temperature can be as low as 50°C (122°F) to initiate the precipitation of β phase both along the grain boundaries and inside the grains [2, 3]. Sensitization, IGC, and IGSCC cause detrimental impacts on the performance of 5xxx series aluminum alloys in marine environments. Laser shock peening has been proposed as a method of combating sensitization, IGC, and IGSCC as a response to these issues.

The application of laser shock peening on aluminum alloys surfaces is not a new concept. There is a lot of research that shows laser shock peened aluminum alloys have better fatigue properties than unpeened alloys. However, the belief that laser shock peening will help reduce sensitization and IGSCC for aluminum alloys is a novel claim and requires further investigation and understanding to verify.

As previously mentioned about the major concerns of Al_3Mg_2 β phase precipitates along grain boundaries and the proposed idea about the benefit and solution of using the laser shock peening process to help resolving the sensitization and intergranular attack problems in the 5xxx series aluminum alloys, this research focuses on the effect of laser shock peening on sensitized and un-sensitized AA5083-H116 samples. To understand the effects of laser shock peening on the alloy, materials characterization and computational analysis were performed on both laser shock peened and unpeened specimen, both before and after various heat treatments.

The specific objectives of this research:

1. In order to understand the past and current studies of the sensitization effect on 5xxx series aluminum alloys, a literature review of magnesium atomic segregation and enrichment, Al_3Mg_2 β phase formation, and laser shock peening technology is performed.
2. Based on the findings from the literature reviews, a detailed plan on the heat treatment conditions and schedule is created.
3. Carry out the experiment according to the plan, which included heat treating both peened and unpeened samples at four different temperatures and several different thermal-aging time intervals.
4. For microstructural analysis, optical microscope is used to observe the Al_3Mg_2 β phase formation and microstructural changes between different heat treatments, aging times, and laser shock peening conditions.
5. Transmission electron microscopy (TEM) is used to characterize the difference in dislocation morphology between unaged peened and unpeened samples.
6. Perform finite element method (FEM) modeling by simulating the laser shock peening effect on AA5083-H116 and predict the stress distribution and behavior induced by the laser shock peening process.
7. Interpret and analyze the results and data generated from the experiment and the FEM models.

The outline of this thesis:

- Chapter 1 Introduction: This chapter provides a general overview of the research topic and goals for this research.
- Chapter 2 Literature Review: This chapter contains specific literature review for the following topics,
 - 2.1. Brief overview of aluminum: provides the basic information on and properties of aluminum.
 - 2.2. Aluminum alloys: discusses the different aluminum alloy series and gives a general overview on each series.
 - 2.3. Al 5083-H116 background information: provides the materials properties and compositions of AA5083-H116.
 - 2.4. Sensitization of 5xxx series aluminum alloys: provides the concepts of sensitization in aluminum alloys.
 - 2.5. Magnesium segregation and enrichment: discusses type of segregation and provides findings from literature that shows magnesium enrichment along grain boundaries and on free surfaces of aluminum.
 - 2.6. Al_3Mg_2 β phase: discusses the aluminum and magnesium binary phase diagram and detailed descriptions of Al_3Mg_2 β phase formation.
 - 2.7. Laser shock peening technology: details the theory and process of laser shock peening technology.

- Chapter 3 Experimental Methods and Results: This chapter provides a detailed plan for the experiment, which includes experiment set-up, sample preparation, testing procedures, measuring methods, and results.
 - 3.1. Testing Materials: provides testing specimens information.
 - 3.2. Laser Shock Peening process: summarizes the application of laser shock peening on the specimen.
 - 3.3. Heat Treatments: provides a detailed plan for thermal treatment and aging times based on the literature review findings, and explains the experimental set-up and procedures for the artificial sensitization process.
 - 3.4. Material Characterization: provides sample preparation steps, testing procedures and results to the following material characterization methods.
 - 3.4.1. Optical Microscopy
 - 3.4.2. Optical Microscopy Results
 - 3.4.3. Average Grain Size Measurement
 - 3.4.4. Average Grain Size Measurement Results
 - 3.4.5. Transmission Electron Microscopy (TEM)
 - 3.4.6. Transmission Electron Microscopy Results
 - 3.4.7. Dislocation Density Measurement
 - 3.4.8. Dislocation Density Measurement Results
- Chapter 4 Finite Element Method (FEM) Modeling: This chapter discusses the concept of finite element analysis, the instructions for

developing the models, the validation of the models, and the results from the model.

- Chapter 5 Results and Discussion: This chapter discusses the effect of laser shock peening process observed with optical microscopy, TEM, and FEM modeling. The discussion is mainly focus on the changes in microstructure, dislocation morphology, and $\text{Al}_3\text{Mg}_2 \beta$ phase formation in AA5083-H116.
 - 5.1. Light Optical Microscopy
 - 5.2. Transmission Electron Microscopy
 - 5.2.1. Thermal Effect from Laser Shock Peening Process
 - 5.2.2. $\text{Al}_3\text{Mg}_2 \beta$ Phase Precipitates
 - 5.2.3. Dislocation Morphology
 - 5.3. Finite Element Method Modeling
- Chapter 6 Conclusions: This chapter summarizes the research, results, and discussions from the investigation into the effects of laser shock peening on AA5083-H116 and provides suggestions for future work on the topic.

Chapter 2: Literature Review

- 2.1. Brief Overview of Aluminum

Aluminum is a soft, ductile, and paramagnetic metal with an appearance of silvery – white color. The chemical element symbol for aluminum is Al with an atomic number 13. It is located on the right side of the periodic table and is the second element in the boron group. Aluminum is the most abundant metal in the Earth's crust, and it can be mostly found in bauxite, an aluminum-rich ore for commercial aluminum extraction [4]. Aluminum has several attractive properties to many industries, and it is used in many applications. These properties include low density, high ductility, corrosion resistance, high electrical and thermal conductivity, and adjustable chemical compositions that can provide different mechanical properties. Aluminum's corrosion resistance comes from a naturally forming oxide layer that passivates the surface and blocks further oxidation. However, pure aluminum is too soft, too ductile, and has limited mechanical properties, making it suitable for only a few applications. To improve the properties and performance of aluminum, different kinds of alloying elements are added to improve mechanical properties, especially strength. This makes aluminum usable in many applications.

- 2.2. Aluminum Alloys

With aluminum's light-weight properties and the growth of aluminum fabrication processes, many industries seek to increase its mechanical properties and use aluminum as an alternative material for steel in many applications. To increase aluminum's mechanical properties, alloying elements such as copper, manganese, silicon, magnesium, and zinc are added. Aluminum can be cast or wrought, and the addition of different principal alloying elements are categorized in different series, which shows in Table 1 and Table 2 [5].

Table 1. Aluminum wrought alloy series and its principal alloying element.

Aluminum Alloy Series	Principal Alloying Element
1xxx	Minimum 99.00% of Aluminum content (Commercially Pure Aluminum)
2xxx	Copper
3xxx	Manganese
4xxx	Silicon
5xxx	Magnesium
6xxx	Magnesium + Silicon
7xxx	Zinc
8xxx	Other Elements (ex. Iron)

Table 2. Aluminum casting alloy series and its principal alloying element.

Aluminum Alloy Series	Principal Alloying Element
1xx.0	Minimum 99.00% of Aluminum content (Commercially Pure Aluminum)
2xx.0	Copper
3xx.0	Silicon with copper and/or magnesium

4xx.0	Silicon
5xx.0	Magnesium
6xx.0	Unused
7xx.0	Zinc
8xx.0	Tin
9xx.0	Other

Eight different wrought aluminum series can be further separated into heat treatable and non-heat treatable aluminum alloys. The following lists provide general characteristics of each principle alloying element in its wrought aluminum series. This information was gathered from ASM International handbooks [4, 5].

- *1xxx Series Aluminum Alloys (Non-heat Treatable)*

This series of aluminum alloys are non-heat treatable and can only be strain hardened to acquire optimal mechanical properties. 1xxx series aluminum alloys have a minimum of 99.00% aluminum, and it is considered to be commercially pure aluminum. With at least 99.00% of aluminum, 1xxx series aluminum alloys have great corrosion resistance, electrical and thermal conductivity, and formability.

- *2xxx Series Aluminum Alloys (Heat Treatable)*

Copper is the major alloying element in this series of aluminum alloys. They are heat treatable and are strengthened by precipitation hardening. They have high strength

at both room temperature and elevated temperature with yield strengths that can reach 455 MPa, or 66ksi.

- *3xxx Series Aluminum Alloys (Non-heat Treatable)*

Manganese is the major alloying element in this series of aluminum alloys. They are hardened by strain hardening. They have medium strength with great formability and corrosion resistance. Typical applications include architectural applications, beverage and food containers, and various products.

- *4xxx Series Aluminum Alloys (Non-heat Treatable)*

Silicon is the principal alloying element in this series of aluminum alloys. They have great flow characteristics and medium strength. With great flow property, 4xxx series aluminum alloys are mostly used at soldering and brazing.

- *5xxx Series Aluminum Alloys (Non-heat Treatable)*

Magnesium is the major alloying element in this series of aluminum alloys. 5xxx series aluminum alloys are largely used in marine applications as they are strain hardenable and have exceptional corrosion resistance, strength, toughness, and weldability. However, they are susceptible to intergranular attack when exposed to elevated temperatures for prolonged periods of time.

- *6xxx Series Aluminum Alloys (Heat Treatable)*

Magnesium and silicon are both major alloying elements for this series of aluminum alloys. They have great corrosion resistance, strength, and excellent extrudability. This series of aluminum alloys are commonly used in architectural and automotive extrusion components.

- *7xxx Series Aluminum Alloys (Heat Treatable)*

Zinc is the principal alloying element for this series of aluminum. They have outstanding strength and toughness, and they are mechanically joined together.

- *8xxx Series Aluminum Alloys (Heat Treatable)*

The principal alloying elements are other elements that are not covered in other series. They are heat treatable and have great strength, hardness, and conductivity.

- 2.3. AA5083-H116 Background Information

This research focuses on AA5083-H116, and it is important to know the background information about AA5083-H116 alloys.

The 5xxx series aluminum alloys are wrought and non-heat treatable aluminum alloys that contain a majority of magnesium alloying element. AA5083 contains about 4.0 wt. % to 4.9 wt. % of magnesium, and less than 1 wt.% of other alloying elements [6 – 8]. Table 3 contains full details on the chemical compositions of AA5083. This series of aluminum alloys has the highest strength within the non-heat treatable aluminum alloys series, and the strength can be further enhanced by using cold work strain hardening and solute hardening due to its high magnesium content [9, 10]. Table 4 further shows the general mechanical properties of AA5083 [8, 11]. Aluminum alloys that are in the H temper category means the aluminum alloys are subjected to strain hardening. Hence, the letter and number “H1” after AA5083 indicates that the AA5083 aluminum has been strain hardened only without any other process to enhance its mechanical properties. AA5083 has been highly attractive for marine applications and ship building [9, 10, 12, 13]. However, there is a major drawback for having a large alloying content of magnesium (> 3 wt. %), as this will significantly increase the susceptibility of intergranular corrosion under thermal exposure [14 – 18]. Intergranular attack has been strongly associated with the Al_3Mg_2 β phase formation along the grain boundaries and the β phase’s high selective-dissolution rate in chloride solution [9, 10, 19 – 21]. More information and literature review on sensitization, magnesium segregation, and Al_3Mg_2 β phase formation, are presented in Section 2.4., Section 2.5., Section 2.6., and Section 2.7.

Table 3. Chemical composition of AA5083.

AA 5083	
Alloys	Weight Percent (wt. %)
Magnesium (Mg)	4.0-4.9
Silicon (Si)	0.40
Iron (Fe)	0.40
Copper (Cu)	0.10
Manganese (Mn)	0.40-1.0
Chromium (Cr)	0.05-0.25
Zinc (Zn)	0.25
Titanium (Ti)	0.15
Others	0.15
Aluminum (Al)	Balance

Table 4. Mechanical properties of AA5083

Density	$2770 \frac{kg}{m^3}$
Hardness, Rockwell A	36.5
Yield Strength	228 MPa
Ultimate Tensile Strength	317 MPa
Elongation at Break	16 %
Modulus of Elasticity	71 GPa
Fatigue Strength	159 MPa
Shear Modulus	26.4 GPa

- 2.4. Sensitization of 5xxx Series Aluminum Alloys

Sensitization is a process where chemical elements diffuse out of the matrix and precipitates at the grain boundaries. The precipitates along grain boundaries heavily promote the material's susceptibility to intergranular corrosion and stress corrosion cracking. The sensitization of 5xxx series aluminum alloys refers to the precipitation of magnesium-rich beta phase along the grain boundaries under thermal exposure. Precipitation of Al_3Mg_2 β phase has been suspected with magnesium segregation and enrichment at the grain boundary [22, 23]. Sensitization for 5xxx series aluminum alloy can occur from 50°C to 200°C in three different Al_3Mg_2 β phase configurations: discontinuous, semi-continuous, and continuous [24 – 29]. Al_3Mg_2 β phase configurations are further discussed in Section 2.6.

- 2.5. Magnesium Segregation and Enrichment

Grain boundaries and grain interiors have different structural properties that can lead to an energy difference. Energy imbalance will cause chemical partitioning and segregation. Element segregation can be separated into two categories: equilibrium segregation and non-equilibrium segregation. Both equilibrium and non-equilibrium segregation can significantly influence a material's mechanical and chemical properties.

Equilibrium segregation occurs when there are energy differences due to lattice disorder at the interfaces, and solute atoms will partition and deposit themselves to minimize the free energy of the system. Therefore, the main driving force for

equilibrium segregation is the reduction of surface free energy as the solute atoms diffuse to grain boundaries, interfaces, and free surfaces [30, 31].

Non-equilibrium segregation is mostly observed during cooling processes, where complex diffusion occurs between vacancies and impurities. Atomic segregation happens at vacancy sinks (i.e. grain boundaries) and free surfaces. There will be a concentration difference between the segregated sites and the bulk grain before and after the cooling process. Thus, the processing history causes non-equilibrium segregation [30 – 32]. Unlike equilibrium segregation, atomic segregation increases with temperature [30].

For 5xxx series aluminum alloys, magnesium segregation and enrichment has both equilibrium and non-equilibrium segregation processes that allows magnesium atoms to diffuse to both the grain boundaries and free surfaces of aluminum during natural and/or artificial aging processes [33 – 39]. According to Vetrano et al., the enrichment ratio of magnesium at grain boundary triple point junction to magnesium in matrix is 3:1, and the enrichment ratio of magnesium along grain boundary to magnesium in matrix is 2.5:1 [33]. Lea et al. and Esposito et al. both observed a great increase of magnesium enrichment on the free surface of aluminum (110) plane under high temperature [34, 35]. Magnesium enrichment on aluminum (110) plane ratio is 12:1 at 200°C [34], and 31:1 at 227°C [35]. Magnesium segregation and enrichment has been suspected to be associated with the formation of Al_3Mg_2 β phase and promoted intergranular corrosion.

- 2.6. Al₃Mg₂ Beta (β) Phase

During the process of manufacturing the 5xxx series aluminum alloys, the metal is heated above the solvus temperature for the alloying additions to solutionize it, creating single phase homogeneous solid solution. The aluminum is then quickly cooled below the solvus temperature to form a supersaturated solid solution of magnesium in the aluminum matrix. Below the solvus temperature, both the α solid solution phase and the β (Al₃Mg₂) intermetallic-compound phase are present in the equilibrium state. Figure 1 shows the binary phase diagram of aluminum and magnesium [40]. The vertical red line represents the range of magnesium content in AA5083 (4.0 wt. % to 4.9 wt. %), and the blue line indicates the solvus line. The solvus line on a binary phase diagram determines the solid solubility limit for the two solid phases, and the line is highly temperature dependent.

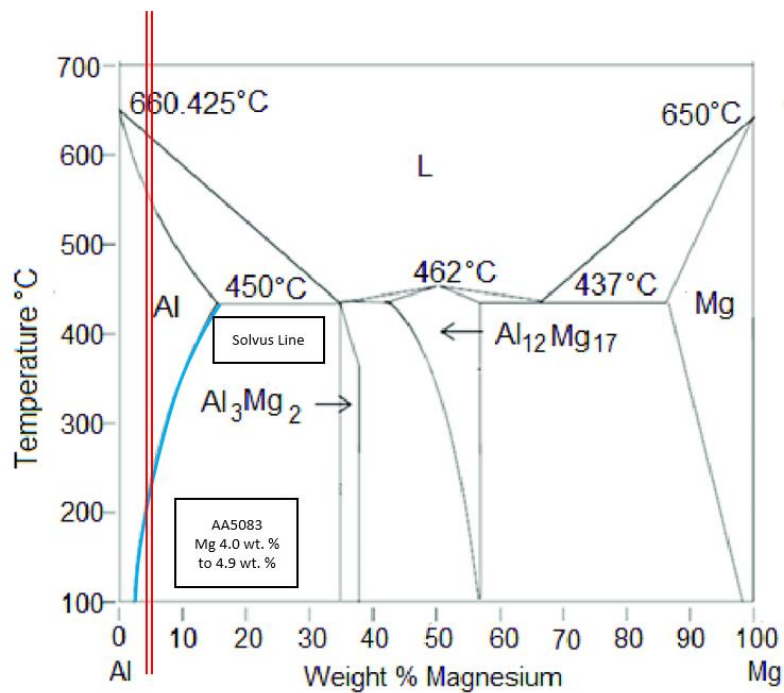


Figure 1. Binary phase diagram of aluminum and magnesium.

As the alloy is naturally and/or artificially aged below the solvus temperature, magnesium segregation occurs, and magnesium diffuses to the grain boundaries and the free surfaces of aluminum. Fine dispersed β' nucleates at the grain boundaries and later transform into β phase. In general, when the alloy is sensitized at lower sensitization temperature and for a long period of time, the formation of Al_3Mg_2 β phase follows the following stages [41 – 48]:

*Supersaturated Solid Solution (α) \rightarrow GP Zones \rightarrow β'' phases \rightarrow β' phases
 \rightarrow β phases*

Some studies have reported that when sensitization temperature exceeds 90°C, Guinier-Preston (GP) zones and β'' phases do not appear during the Al_3Mg_2 β phase formation [42, 45, 46]. This is due to the fact that GP zones and β'' phase have low dissolution temperatures, and higher temperatures provide greater diffusion rates for magnesium atoms [42, 45, 46]. So, when the sensitization temperature is above the GP zone and β'' dissolution temperatures, β' phases will form as the beginning of the Al_3Mg_2 β phase formation sequence. The following stage sequence is for high temperature Al_3Mg_2 β phase formation:

Supersaturated Solid Solution (α) \rightarrow β' phases \rightarrow β phases

The first stage of Al_3Mg_2 β phase formation is developed during the manufacturing process of the 5xxx series aluminum alloys. With heat treatments above the solvus temperature and rapid quenching, a supersaturated solid solution (α) of magnesium forms in the aluminum matrix. After the first stage, as the temperature starts

to rise, nanometer size magnesium rich clusters begin to form. These create the Guinier-Preston (GP) zones [42, 43, 45 – 48]. The third β'' stage is similar to the GP zones that contain clusters of magnesium rich regions but with a more order and coherent arrangement with the matrix. The main composition for β'' phase is Al_3Mg with an L_{12} structure, and it has a spherical morphology [42, 45].

As the duration of thermal exposure continues to increase, the GP zones and β'' phases stages dissolve and semi-coherent β' phases precipitate at the grain boundaries to lower the free energy in material [42, 43, 45, 49]. The initial preferred precipitation location is grain boundary triple point junction, along the grain boundaries, and at the interface between aluminum matrix and Al_6Mn dispersoids [33, 37]. β' is an intermediate phase with the approximate composition of Al_3Mg_2 . β' phase has a hexagonal structure with lattice parameters of $a = 1.002\text{nm}$ and $c = 1.636\text{nm}$ [42, 43, 45].

Equilibrium β phase forms through the transformation of β' phase. β phase has a composition of Al_3Mg_2 with a complex face center cubic (f.c.c.) structure and lattice parameter $a = 2.824\text{nm}$ [37, 42 – 46, 49]. The β phase precipitates have a distinguishable orientation relationship with the aluminum matrix (α), but the actual orientation is still unclear. Bernole et al. has reported that at 200°C the orientation relationship is $(111)_\beta \parallel (001)_\alpha$ and at 300°C the orientation relationship is $[110]_\beta \parallel [010]_\alpha$ [50]. However, Kubota has observed a different orientation relationship between β phase and aluminum matrix (α) at 240°C [43]. For coarse globular β phase precipitates, the orientation relationships with (α) matrix are $(1\bar{1}1)_\beta \parallel (1\bar{1}1)_\alpha$ and

$[011]_{\beta} \parallel [0\bar{1}\bar{1}]_{\alpha}$. For smaller spheroidal β phase precipitates, the orientation relationships with (α) matrix are $(100)_{\beta} \parallel (100)_{\alpha}$ and $[001]_{\beta} \parallel [001]_{\alpha}$.

During the sensitization process, β phase can undergo three different morphologies as aging time increases [24 – 29]. The images presented in Figure 2 (a), (b), (c), and (d) are from R.L. Holtz et al. shows the morphological evolution of β phase at 175°C with increasing aging time [28]. Initially, β phase will be discontinuous, and as time goes on, β phase will change to semi-continuous and continuous. Some studies have observed that after an extremely long thermal exposure, β phase will break up and become discontinuous phase [26 – 28].

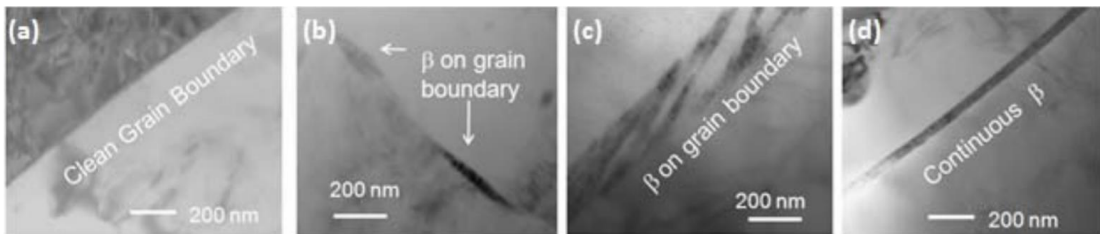


Figure 2. AA5083-H131 β phase morphology evolution at 175°C. (a) Unaged β phase, (b) Discontinuous β phase at 1 hour of ageing time, (c) Semi-continuous β phase at 50 hours of ageing time, (d) Continuous β phase at 240 hours of aging time.

Even though the precipitation of Al_3Mg_2 β phase has been the subject of much research, the nucleation, kinetics, transformations, lattice structure, phase orientations and interactions between magnesium atoms, vacancies, and other defects during each stage of Al_3Mg_2 β phase formation are still subjects of debate.

- 2.7. Laser Shock Peening Technology

The earliest studies of laser shock peening process were back in the 1960s and lasted until the beginning of the 1980s at Battelle Institute in Columbus, Ohio, USA. Some data of laser shock peening showed promising effects on fatigue properties and demonstrated the potential to be an alternative process for the conventional shot- and hammer-peening treatments. Laser shock peening research and development stopped around 1981, but relevant research was continued in the 2000s [51].

Laser shock peening is a cold work, mechanical surface enhancement process that uses a high energy, short pulse laser beam with $4 \frac{GW}{cm^2}$ to $10 \frac{GW}{cm^2}$ to strike the sample surface [52 – 54]. This creates shock waves that can plastically deform the sample surface and propagate into the sample introducing residual compressive stresses that can modify material properties [52 – 55]. During the laser shock peening process, to effectively form a high temperature plasma on the sample, an opaque black overlay is added on top of the sample surface. The black overlay has low vaporization temperature that can easily absorb the high energy pulses and heat up to form a plasma gas. Additionally, water overlay is added on top of the opaque overlay to limit the thermal expansion of plasma gas and avoid thermally changing the sample properties and microstructure. The black opaque and water overlays help to trap the plasma gas in between the water layer and the sample surface, which will build up a very high gas pressure. The high gas pressure produced from each pulse of the laser beam will generate a shock wave that can travel into the sample and create compressive stresses [51 – 55]. Figure 3 shows the general process for laser shock peening [56].

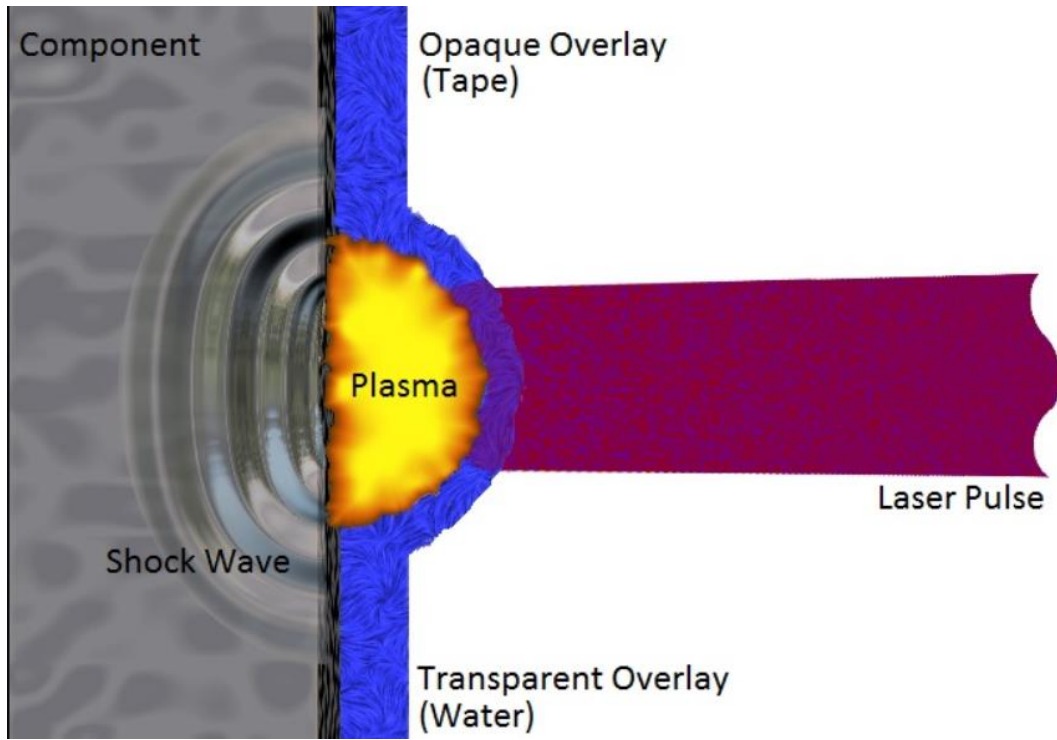


Figure 3. Laser shock peening process.

Chapter 3: Experimental Methods and Results

- 3.1. Testing Materials

All the testing samples used in this research are provided by the Naval Surface Warfare Center, Carderock Division (NSWCCD). The testing samples are AA5083-H116. There is a total of 28 square AA5083-H116 samples, where 10 of the samples were not laser shock peened and 18 of the samples were laser shock peened. Figure 4 (a), (b), and (c) show the as-received laser shock peened samples and as-received no laser shock peened samples. The rolling direction is marked on the sides of each sample with an arrow pointing in the rolling direction. Samples were rolled on the square surface. The surface texture of laser shock peened samples is different than the surface texture of no laser shock peened samples. For the laser shock peened sample, its surface texture is rough, and a small array of circular deformations caused by the laser shock peening can be easily observed on the sample surface, shown in Figure 4 (a). The samples without laser shock peening have a smooth surface, shown in Figure 4 (b). Both top and bottom square surfaces of the laser shock peened samples were laser shock peened, but not the sides (rectangular surfaces).

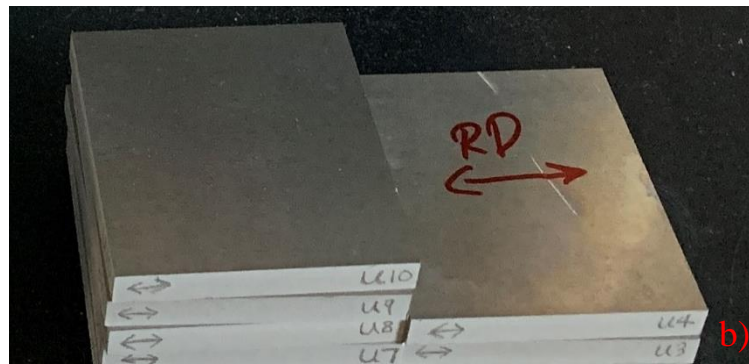


Figure 4. (a) As-received laser shock peened AA5083-H116 samples, (b) As-received no laser shock peened AA5083-H116 samples, and (c) Total 28 AA5083-H116 samples with 18 laser shock peened samples (left) and 10 no laser shock peened samples (right).

All 28 square AA5083-H116 samples have roughly the same dimensions with some small variation in length and width due to cutting (about $\pm 3.175\text{mm}$ ($\pm 0.125\text{in}$)). The sample thickness is the same without significant variation because they were cut from the same aluminum plate. The dimensions are listed in Table 5. The average chemical composition of testing samples can be found in Table 6. The nomenclatures for the samples are:

- P1 to P18 stands for laser shock peened sample 1 to 18
- U1 to U10 are for no laser shock peened (unpeened) sample 1 to 10.

Table 5. Dimensions of testing samples.

Length	76.2mm \pm 3.175mm 3in \pm 0.125in
Width	76.2mm \pm 3.175mm 3in \pm 0.125in
Thickness	9.53mm 0.375in

Table 6. Average chemical composition of AA5083-H116.

Elements	Cu	Mg	Mn	Si	Zn
wt. %	0.03670	4.771	0.6196	0.1553	0.09438
Elements	Cr	Fe	Ti	Others	Al
wt. %	0.09917	0.2925	0.01865	0.08652	93.83

- 3.2. Laser Shock Peening Process

The laser shock peening process was carried out by LSP Technologies, Inc., and the general sample preparation procedures were provided by the company. The following information is summarized from the laser shock peening report given by LSP Technologies, Inc.

In order to minimize material waste and maximize the process efficiency during laser shock peening process, all the samples were carefully measured and cut into desired holding shape for easier clamping during process. During the process, the sample surface is coated with an opaque black overlay and covered with water, and then bombarded with high energy laser pulses. The laser intensity was $4 \frac{GW}{cm^2}$ and the pulse duration was 20ns. Both the top and bottom surfaces were laser shock peened twice with the two-layer of application. The laser shock peening moving direction was perpendicular to the rolling direction, and it is constant throughout all the samples. Schematic views of the two-layer laser shock peening application and laser shock peening moving direction are shown in Figure 5. The two-layer application allows each surface to get laser peened twice. The sample is first laser shock peened on one side (side 1), starting from the bottom and going from left to right. After the row is completed, the next row starts above the previous, with this movement perpendicular to the rolling direction. Once the laser shock peening reaches the top, the sample is flipped to the other side (side 2). This time the laser shock peening starts at the top while still moving from left to right and shifting down perpendicular to the rolling direction. Then, the same side (side 2) is laser shock peened again from the bottom to

the top with the same moving method. Last, the sample is flipped back to the starting side (side 1), and laser shock peened from top to bottom with the same moving method.

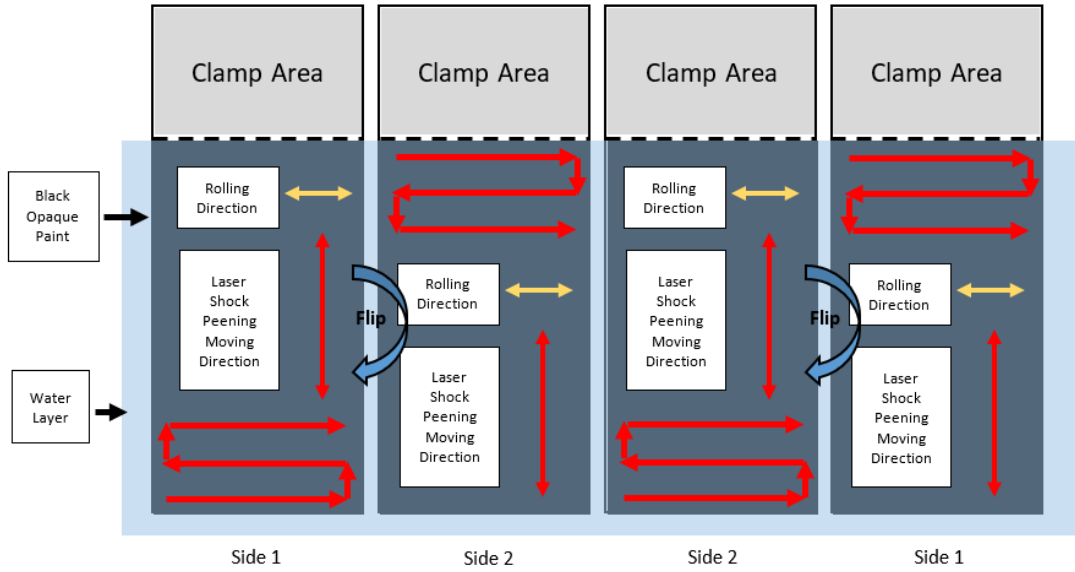


Figure 5. Two layers application for laser shock peening process.

After the laser shock peening process, samples are cut by using a wire electrical discharge machine (EDM) into $76.2\text{mm} \times 76.2\text{mm} \times 9.53\text{mm}$ ($3\text{in} \times 3\text{in} \times 0.375\text{in}$) $\pm 3.175\text{mm}$ ($\pm 0.125\text{in}$).

- 3.3. Heat Treatments

Many studies have shown different morphologies of $\text{Al}_3\text{Mg}_2 \beta$ phase at different sensitization temperatures and aging times. It has been observed that as the aging time increases, $\text{Al}_3\text{Mg}_2 \beta$ will go through four stages of transformation. The four stages are discontinuous, semi-continuous, continuous, and discontinuous beta phase. Table 7 shows the reported time and temperature from several studies for each beta phase morphology to appear [57 – 62].

Table 7. Reported initial time for each β phase morphology to appear at each temperature.

	Discontinuous β	Semi-Continuous β (Ribbon-like)	Continuous β	Discontinuous β
70 °C	480 hrs (20 days) [57]		3000 hrs (125 days) [58, 59]	
100 °C	72 hrs to 336 hrs (3 days to 14 days) [59, 60]		1080 hrs (45 days) [58 – 60]	2000 hrs (83.3 days) [59]
150 °C	82.5 hrs (3.44 days) [61]		189 hrs (7.87 days) [60, 61]	262 hrs (11 days) [60, 61]
175 °C	1 hrs (0.0417 days) [59, 60, 62]	50 hrs (2.083 days) [59, 62]	200 – 240 hrs (8.33 days to 10 days) [58 – 60, 62]	

Based on the reported sensitization times and temperatures for each β phase morphology, the following heat treatment schedule was created, shown in Table 8. There are more samples heat treated at 100°C with several aging time as a way to see the trend of β phase morphology changes. Since there are fewer unpeened samples, only the sensitization time and temperature for discontinuous and continuous β phase are tested. For each unpeened samples, there will be a laser shock peened sample that undergoes the same heat-treating condition. This allows the examination of the effect of laser shock peening on the material. The sample heat treatment was carried out at University of Maryland, College Park (UMD), and the furnaces used for this heat treatment are Thermo Scientific Thermolyne Furnace FB1400, shown in Figure 6 (a) and (b).



Figure 6. Thermo Scientific Thermolyne furnace FB1400 at UMD. (a) Furnace 1 (F1) and Furnace 2 (F2) from left to right and (b) Furnace 3 to Furnace 6 (F3 to F6) from right to left.

Table 8. Sample sensitizing temperature and time and sample ID

Temp	Heating Conditions	Specimen (peened)	Specimen (unpeened)	Furnace Number
70°C	1. Discontinuous phase: 23 days (550 hours)	P1	U1	F5
	2. Continuous phase: 150 days (3600 hours)	P2	U2	F2
100°C	3. Discontinuous phase: 3 days (72 hours)	P3		F6
	4. <i>Discontinuous phase: 7 days (168 hours)</i>	P4	U3	F6
	5. <i>Discontinuous phase: 15 days (360 hours)</i>	P5		F6
	6. Semi-continuous phase: 23 days (550 hours)	P6	U4	F6
	7. <i>Semi-continuous phase: 35 days (840 hours)</i>	P7		F6
	8. Continuous phase: 46 days (1100 hours)	P8	U5	F5
	9. <i>Continuous phase: 67 days (1608 hours)</i>	P9		F4
	10. Discontinuous phase: 88 days (2112 hours)	P10		F3
	11. <i>Discontinuous phase: 150 days (3600 hours)</i>	P11		F1
	150°C	12. Discontinuous phase: 3 days (72 hours)	P12	U6
13. Continuous phase: 7 days (168 hours)		P13	U7	F6
14. Discontinuous phase: 12 days (288 hours)		P14		F6
175°C	15. Discontinuous phase: 5 hours	P15	U8	F6
	16. Semi-continuous phase: 3 days (72 hours)	P16		F6
	17. Continuous phase: 12 days (288 hours)	P17	U9	F6
Total:		17	9	
None	No Heat Treatment Sample	P18	U10	
Overall Total:		18	10	

- 3.4. Material Characterization

- *3.4.1. Optical Microscopy*

Before the sample was observed under the optical microscope, sample was cut into smaller sizes and mounted in an acrylic mixture. First, the sample was cut into approximately $25.4\text{mm} \times 25.4\text{mm} \times 9.53\text{mm}$ ($1\text{in} \times 1\text{in} \times 0.375\text{in}$) in the L-T and T-L directions. Then, the sample was further cut down into approximately $10\text{mm} \times 10\text{mm} \times 9.53\text{mm}$ ($0.394\text{in} \times 0.394\text{in} \times 0.375\text{in}$) in the L-T and T-L directions with the Allied HTP TechCut4 Precision Low Speed Diamond Saw at UMD. Sample cutting directions can be visualized in Figure 7 [63].

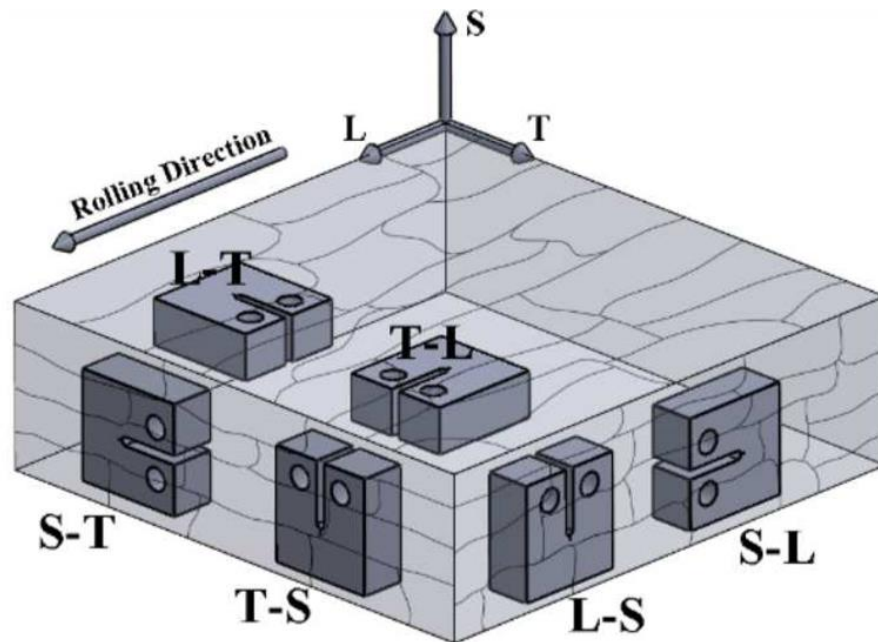


Figure 7. Sample cutting directions: Longitudinal (L) – rolling direction, Transverse (T) direction, and Short transverse (S) direction.

Next, the samples were cold-mounted with the Allied QuickSet acrylic mixture for 24 hours to ensure the acrylic mount had completely hardened. Afterwards, the mounted

samples were mechanically ground and polished with the Struers Teframin-30 sample polisher at NSWCCD. To obtain a smooth and mirror-like surface, the samples were ground and polished with the following steps.

Sample Grinding and Polishing Steps

1. Removed sample surface scratches with the Struers 320 (P-400), 600 (P-1200), 800 (P-2400), and 1200 (P-4000) grit silicon carbide abrasive papers. Finer scratches and smoother surface were achieved as the silicon carbide abrasive paper grit size increased.
2. Polished sample surface first with the Struers $9\mu\text{m}$ diamond suspension on the Struers MD-Plan polyester polishing cloth, and then with the Struers $3\mu\text{m}$ diamond suspension on the Struers MD-Mol wool polishing cloth.
3. Final polished sample surface with the Struers OP-U $0.04\mu\text{m}$ colloidal silica suspension on the Struers MD-Chem porous neoprene plate.

To observe the $\text{Al}_3\text{Mg}_2\beta$ phase precipitates in the sample microstructure, phosphoric acid (H_3PO_4) was used as the etchant to highlight just the $\text{Al}_3\text{Mg}_2\beta$ phase precipitates.

The sample was etched in the following steps.

Sample Etching Steps

1. Phosphoric acid was prepared with deionized (DI) water into 40 vol. % of H_3PO_4 and 60 vol. % of DI water.
2. H_3PO_4 solution was heated up to 35°C before etching the sample.
3. Sample was soaked in 35°C H_3PO_4 solution for 3 minutes

After the sample was etched, the images of Al_3Mg_2 β phase precipitates with different magnifications were captured by using the ZEISS Axio Observer MAT light optical microscope with the ZEISS AxioCam HRc camera attached at NSWCCD. All the micrograph images were taken and viewed in the short transverse direction to the sample rolling direction. Schematic view of the sample viewing surface with respect to the sample rolling direction is shown in Figure 8.

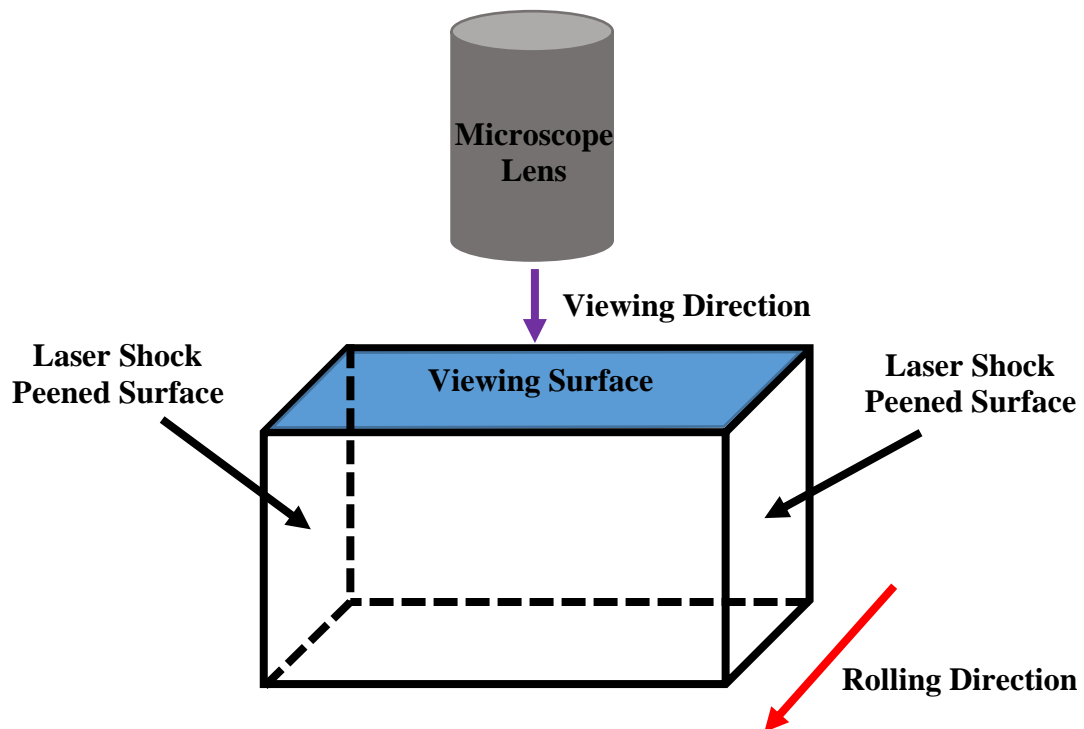


Figure 8. Schematic view of sample under the optical microscope.

○ 3.4.2. *Optical Microscopy Results*

The optical micrographs of AA5083-H116 present a clear association between $\text{Al}_3\text{Mg}_2 \beta$ phase formation and aging temperature and time. With the phosphoric acid etchant, only the $\text{Al}_3\text{Mg}_2 \beta$ phase is highlighted (dark lines and small spots), allowing for the direct comparison of $\text{Al}_3\text{Mg}_2 \beta$ phase formation with the influence of aging temperature and time. In Figure 9 (a) and (b), $\text{Al}_3\text{Mg}_2 \beta$ phase precipitates increase as the aging temperature increases from 100°C to 150°C with a constant aging time (168 hours) in the unpeened (no laser shock peened) samples. Figure 9 (b) shows not only the $\text{Al}_3\text{Mg}_2 \beta$ phase precipitated at the grain boundaries but also heavily precipitated in the aluminum free surfaces. In Figure 10 (a), (b), and (c), under the same aging temperature (100°C), $\text{Al}_3\text{Mg}_2 \beta$ phase increases in the unpeened samples as the aging time changes from 168 hours to 1100 hours. In both cases, a similar trend is observed, where the amount of $\text{Al}_3\text{Mg}_2 \beta$ phase precipitates increase as the aging temperature and time increase.

The same phenomenon of $\text{Al}_3\text{Mg}_2 \beta$ phase increasing with aging temperatures and times have also been observed in the laser shock peened samples, shown in Figure 11 (a), (b) and Figure 12 (a), (b), (c). Moreover, the micrographs of unaged samples have shown the appearance of $\text{Al}_3\text{Mg}_2 \beta$ phase in the AA5083-H116 alloys before any heat treatment had begun. Figure 13 (a) and (b) show the $\text{Al}_3\text{Mg}_2 \beta$ phase precipitates in laser shock peened and unpeened samples prior to the heat treatment process. The prior precipitation of $\text{Al}_3\text{Mg}_2 \beta$ phase could possibly be introduced during the aluminum alloys preprocessing and manufacturing processes.

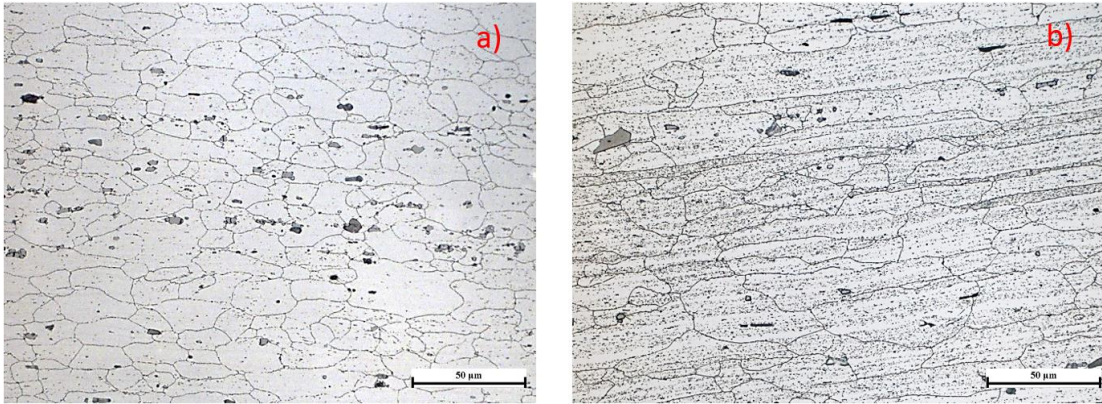


Figure 9. Al₃Mg₂ β phase increases as the aging temperature increases and under a constant aging time. (a) Sample U3 aged at 100°C for 168 hours. (b) Sample U7 aged at 150°C for 168 hours

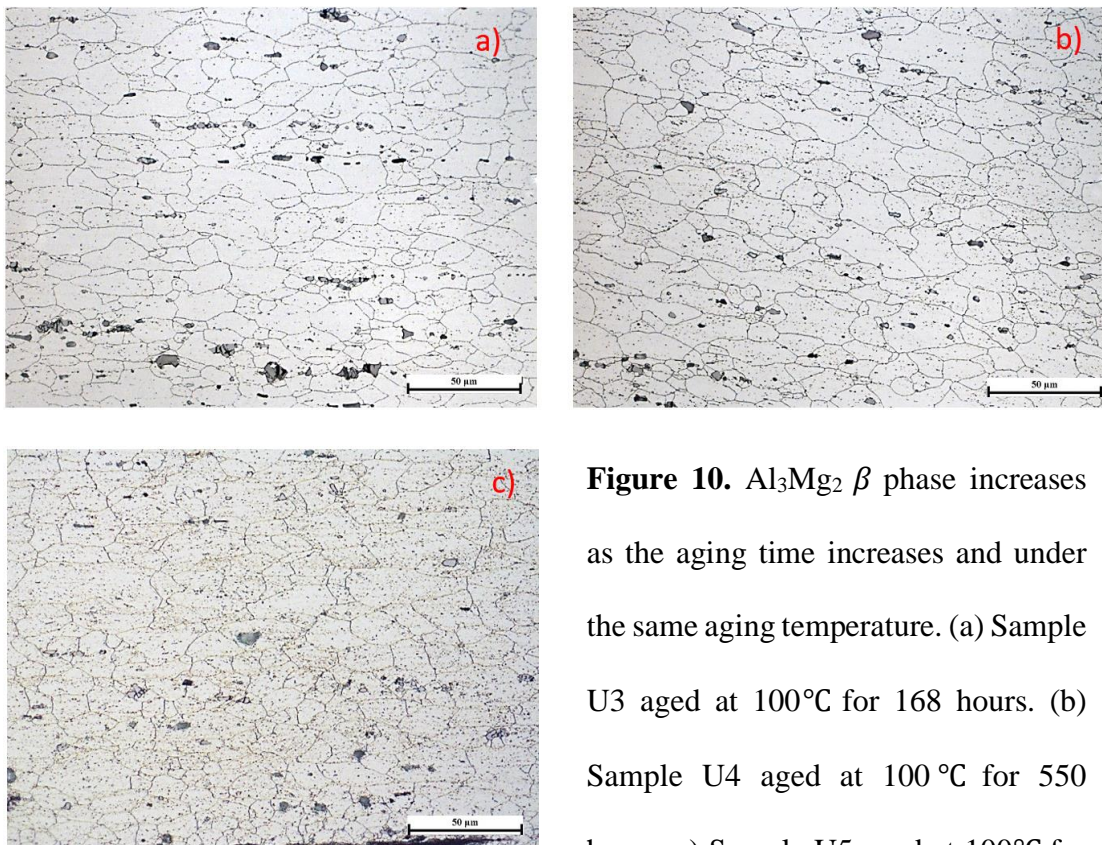


Figure 10. Al₃Mg₂ β phase increases as the aging time increases and under the same aging temperature. (a) Sample U3 aged at 100°C for 168 hours. (b) Sample U4 aged at 100 °C for 550 hours. (c) Sample U5 aged at 100°C for 1100 hours.

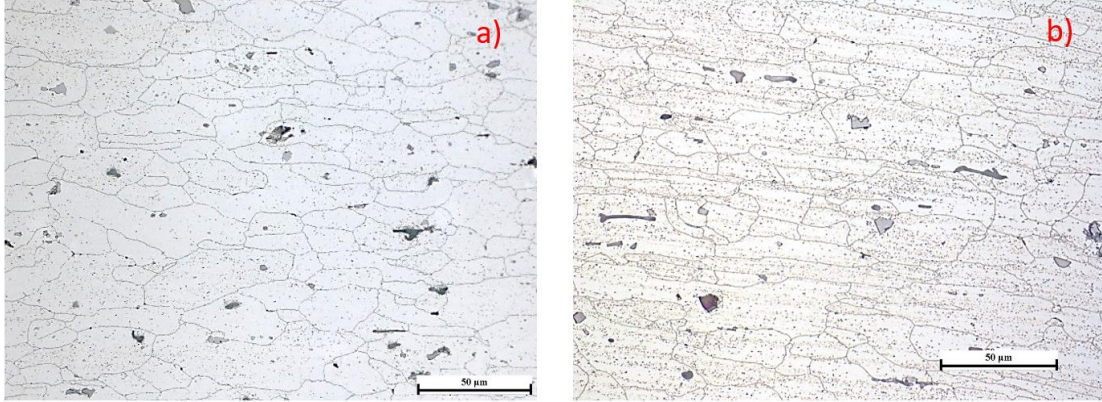


Figure 11. Al₃Mg₂ β phase increases as the aging temperature increases and under a constant aging time. (a) Sample P4 aged at 100°C for 168 hours. (b) Sample P13 aged at 150°C for 168 hours

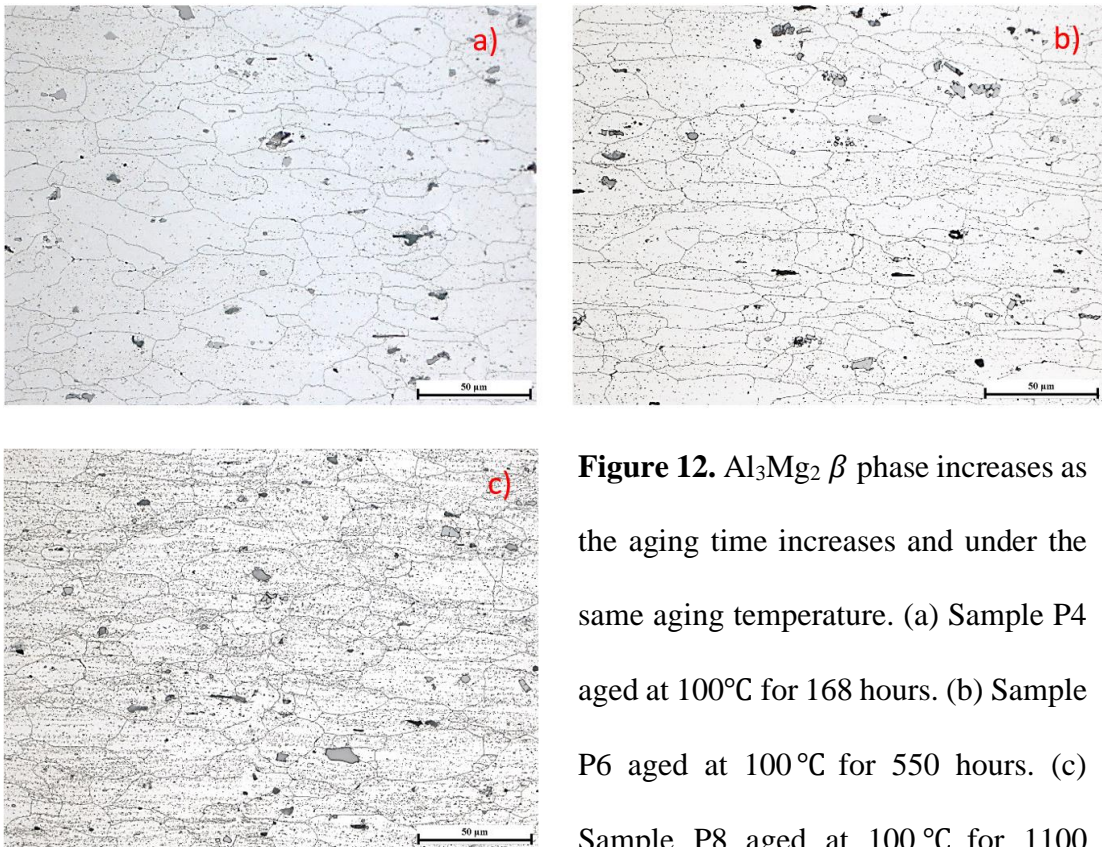


Figure 12. Al₃Mg₂ β phase increases as the aging time increases and under the same aging temperature. (a) Sample P4 aged at 100°C for 168 hours. (b) Sample P6 aged at 100°C for 550 hours. (c) Sample P8 aged at 100 °C for 1100 hours.

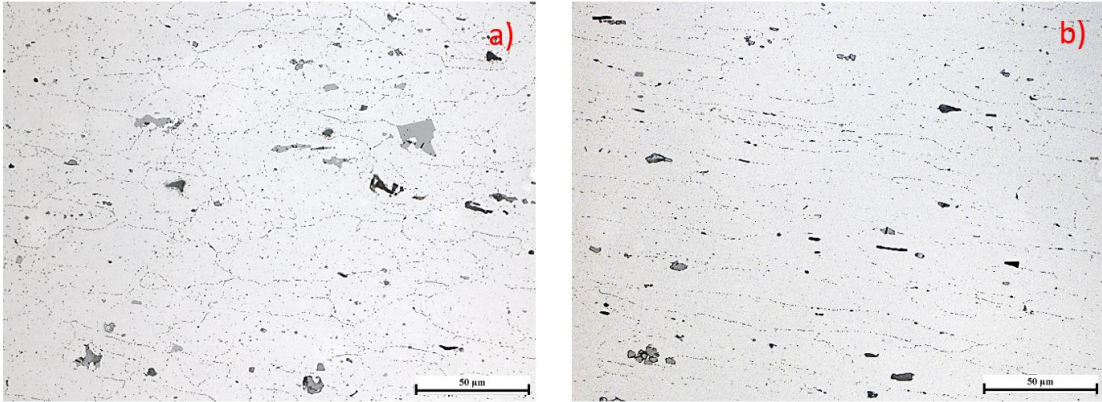


Figure 13. Pre-existing $\text{Al}_3\text{Mg}_2 \beta$ phase. (a) Sample P18 unaged and laser shock peened. (b) Sample U10 unaged and not laser shock peened.

The grain size and morphology variations between both sample surface regions and sample middle region can be noticed from micrographs. From Figure 14 (a) and (b), it appears that the grains near the sample surface region is smaller compares to the grains in the sample middle region. The grains near the surface region have a more circular and equiaxial shape, whereas the grains in the middle region have a more elongated and oblong shape. The differences in grain size and morphology between the sample surface and middle region is consistent throughout all samples despite different aging times and temperatures. Additionally, the variations of grain size and morphology at different sample regions appear in both laser shock peened and unpeened samples. Figure 15 (a), (b), (c), and (d) show the grain size and morphology variations near the sample surface and middle region are the same for both laser shock peened and unpeened samples.

In order to quantitatively proof the grain size between sample surface and middle region and the grain size between laser shock peened and un-peened samples are the same, ASTM E112, Standard Test Methods for Determining Average Grain

Size, was used, and the detailed grain size calculation procedures and results are discussed in the following section.

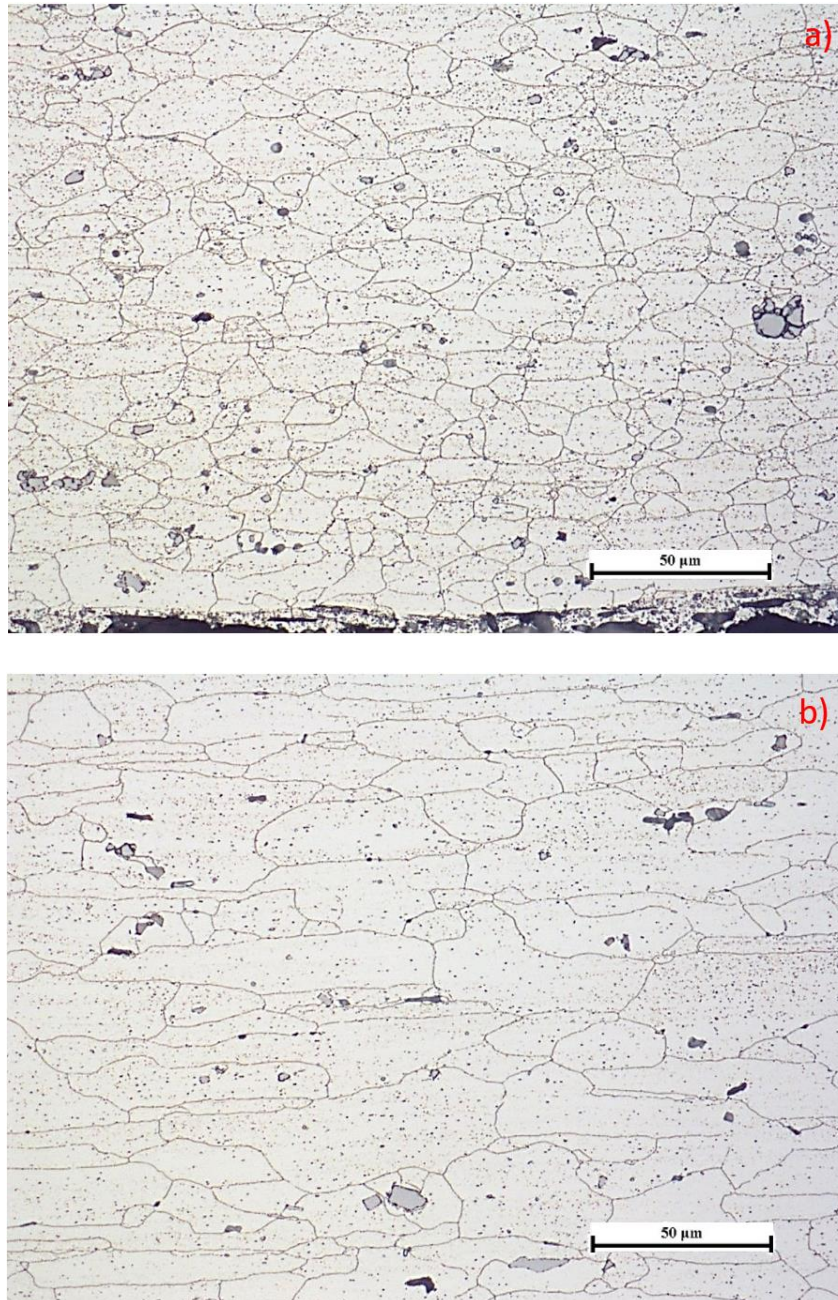


Figure 14. Grain size and morphology variations in the sample. (a) Grains appear to have a more circular and equiaxed shape near the sample surface region. (b) Grains appear to have a more elongated and oblong shape in the sample middle

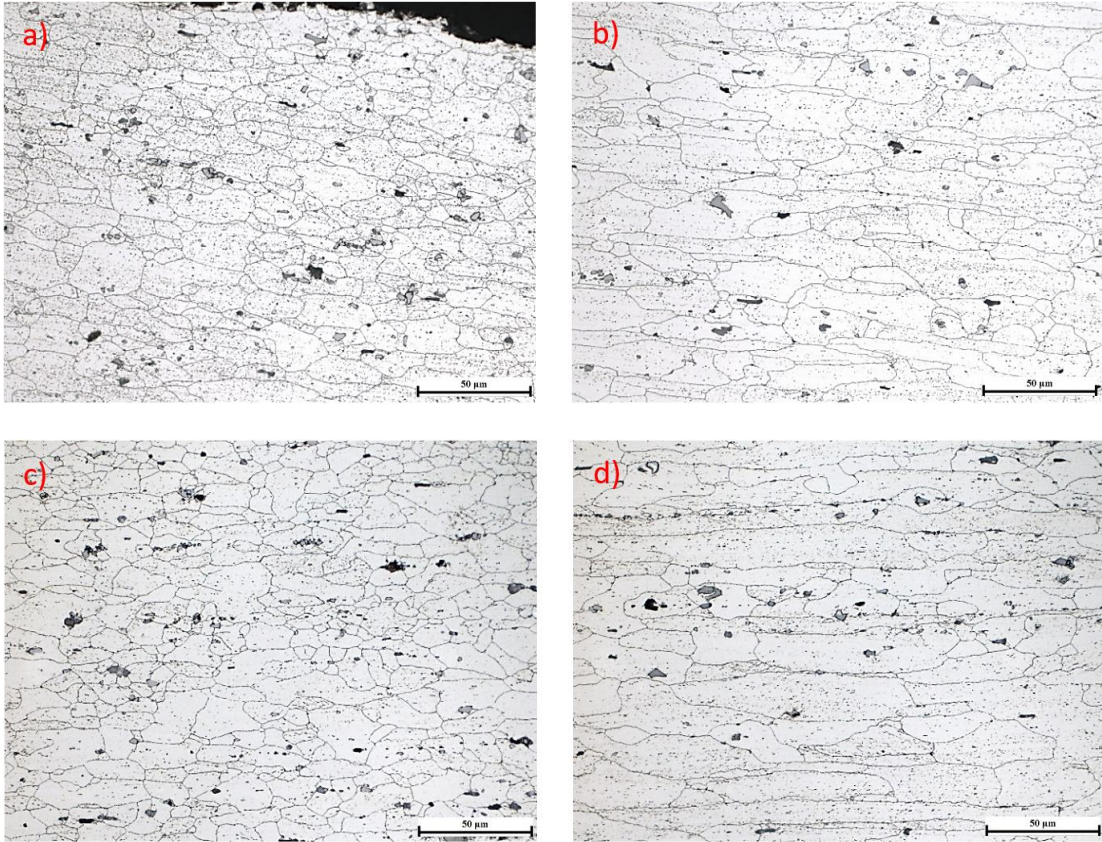


Figure 15. Grain size and morphology variations in both laser shock peened and un-peened samples. (a) Sample P7 near the sample surface region. (b) Sample P7 in the sample middle region. (c) Sample U2 near the sample surface region. (d) Sample U2 in the sample middle region.

○ 3.4.3. Average Grain Size Measurement

To determine the average grain size of the sample, ASTM E112, Standard Test Methods for Determining Average Grain Size, was performed. Both the Planimetric Method and Circular Intercept Method were used to give a more accurate grain size calculation. The differences between the Planimetric Method and Circular Intercept Method are for the Planimetric Method, all the grains completely inside the drawn circle (N_{Inside}) and all the grains intercepted the drawn circle ($N_{Intercepted}$) are being counted. The amount of grains per millimeter squared at 1X (N_A), N_A can be calculated by using Equation (1).

$$N_A = f \left(N_{Inside} + \frac{N_{Intercepted}}{2} \right) \quad (1)$$

f is the Jeffries' multiplier, which can be calculated based on the magnification used (M), shown in Equation (2).

$$f = 0.0002 M^2 \quad (2)$$

After knowing the value of N_A , the ASTM grain size number (G) can be determined by using Equation (3).

$$G = (3.321928 \log_{10} N_A) - 2.954 \quad (3)$$

For the Circular Intercept Method, only the grains (N) or grain boundaries (P) intercepted by the three drawn circles are being counted. When counting grain boundary intersections, a triple point junction is counted as 1.5 grain boundaries intersection and grain boundaries that are tangent to the circle line are counted as 0.5 grain boundary intersections. To obtain the ASTM grain size number for this method, the mean linear intercept value (ℓ) needs to be determined first. ℓ can be calculated by using Equation (4).

$$\ell = \frac{L}{N_i M} = \frac{L}{P_i M} \quad (4)$$

N_i and P_i are the total number of grains and grain boundaries intercepted the drawn circles. L is the total length (circumference) of the test lines and M is the magnification used. Equation (5) calculates the ASTM grain size number (G) for the Circular Intercept Method.

$$G = (-6.643856 \log_{10} \ell) - 3.288 \quad (5)$$

Visual representatives of both grain size measuring methods are shown in Figure 16 (a) and b). The conversion chart of ASTM grain size number (G) to average grain diameter is included in the ASTM E112 document. Besides using both grain size measuring methods to increase the accuracy of determining the sample average grain size, five different locations within the measured region were chosen to calculate the average grain size. In addition, statistical analysis was performed, including the calculation of the standard deviation, 95% confidence interval, and percent relative accuracy. Equation (6), Equation (7), and Equation (8) are equations for calculating the standard deviation (SD), 95% confidence interval (95% CI), and percent relative accuracy ($\%RA$)

$$SD = \left[\frac{\sum (X_i - \bar{X})^2}{n-1} \right]^{\frac{1}{2}} \quad (6)$$

$$95\% CI = \frac{(t)(SD)}{\sqrt{n}} \quad (7)$$

$$\%RA = \frac{95\% CI}{\bar{X}} \times 100 \quad (8)$$

X_i is each individual value of the data, \bar{X} is the mean of X_i , and n is the total number of data measurements. t in Equation (7) is the 95% CI multipliers, which the values of

t is based on the number of fields used in the measurement. The table of value t can be looked up in ASTM E112 document.

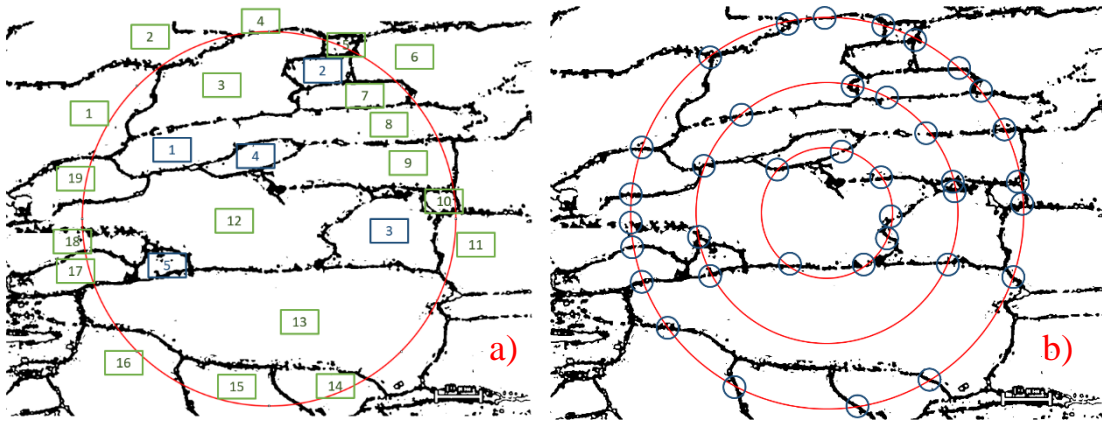


Figure 16. (a) Planimetric Method. Measures the grain size by counting the number of grains inside (blue) and on (green) the drawn circle (red). (b) Circular Intercept Method. Measures the grain size by counting the number of grain boundaries intercept (blue) the three drawn circles (red).

- *3.4.4. Average Grain Size Measurement Results*

To further confirm the grain size variations at the sample surface and middle region, average grain size measurement was performed according to the ASTM E112 guidelines. From the calculation of average grain size, the average grain diameter is smaller near the surface region as compared to the average grain diameter in the middle region. Larger the ASTM grain size number, the smaller the average grain diameter. There are some differences between the grain size calculated from the Planimetric Method and the Circular Intercept Method. However, the differences between the two methods are small enough that won't significantly affect the results interpretation.

The grain size variations at the sample surface and middle region are appeared in both laser shock peened and unpeened samples. The grain diameter at the sample surface region is very similar for both laser shock peened and unpeened samples. Same thing for the grain diameter at sample middle region in laser shock peened and unpeened samples. The average grain size measurements of laser shock peened and unpeened samples are provided in Table 9. The four chosen samples are laser shock peened and unpeened pair samples that have the same aging conditions for each pair. Sample U2 and Sample P2 are laser shock peened (P) and unpeened (U) pair samples with aging temperature at 70°C and 3600 hours of aging time. Sample U9 and Sample P17 are laser shock peened (P) and unpeened (U) pair samples with aging temperature at 175°C and 288 hours of aging time. For the statistical analysis, all the %RAs are less than 10%, which the grain size measurement performed is considered within the acceptable precision. 10% RA is the maximum tolerance for most intended

applications. Briefly, the ASTM average grain size calculation agrees with the grain size variations trend observed in optical micrographs.

Table 9. Grain size measurements for laser shock peened and unpeened samples.

Planimetric Method (Surface Region)				
	U2	P2	U9	P17
ASTM Grain Size Number	9.5	10	10.5	10
Average Grain Diameter (mm)	0.0133	0.0112	0.0094	0.0112
Standard Deviation	0.1716	0.1624	0.1054	0.0623
95% CI	0.2130	0.2016	0.1309	0.077
% RA	2.2055	2.0353	1.2291	0.758

Planimetric Method (Middle Region)				
	U2	P2	U9	P17
ASTM Grain Size Number	8.5	8.5	9	9
Average Grain Diameter (mm)	0.0189	0.0189	0.0159	0.0159
Standard Deviation	0.6243	0.3079	0.2306	0.1960
95% CI	0.7750	0.3823	0.2863	0.2433
% RA	9.1331	4.4145	3.1362	2.7739

Circular Intercept Method (Surface Region)				
	U2	P2	U9	P17
ASTM Grain Size Number	10	10.5	10	10.5
Average Grain Diameter (mm)	0.0112	0.0094	0.0112	0.0094
Standard Deviation	0.3993	0.4271	0.1218	0.1228
95% CI	0.4957	0.5303	0.1512	0.1525
% RA	4.9117	5.0993	1.4843	1.4589

Circular Intercept Method (Middle Region)				
	U2	P2	U9	P17
ASTM Grain Size Number	9	9.5	9	9.5
Average Grain Diameter (mm)	0.0159	0.0133	0.0159	0.0133
Standard Deviation	0.4673	0.4569	0.1823	0.4498
95% CI	0.5802	0.5672	0.2263	0.5585
% RA	6.3098	6.0220	2.5574	5.8394

○ 3.4.5. *Transmission Electron Microscopy (TEM)*

The sample preparation for Transmission Electron Microscopy (TEM) had been performed at UMD, NSWCCD, and the U.S. Naval Research Laboratory (NRL) facilities. The first part of the TEM sample preparation was done at both UMD and NSWCCD, which the preparation involved manually ground and polished sample and mechanically punched out a 3mm disk for the standard TEM sample holder. The main goal for doing the TEM analysis is to observe the effect caused by the laser shock peening process. Thus, in order to directly compare the laser shock peening effect, only the as-received unaged sample (U10) and laser shock peened unaged sample (P18) were prepared and used in the TEM analysis. The following list provides the general procedures for the first part of TEM sample preparation.

Part 1: TEM Sample Preparation at UMD and NSWCCD

1. Used the sample that was left from preparing optical microscope sample and sliced the sample as thin as possible with the Allied HTP TechCut4 Precision Low Speed Diamond Saw at UMD.
2. The thin sample slice was cutting in the S-L direction near the laser shock peened surface for the laser shock peened sample, and the unpeened sample was also cut in the S-L direction near the unpeened surface.
3. The thin sample slice was cold-mounted with the Allied QuickSet acrylic mixture for 24 hours with the cut surface facing down (the cut surface was not covered by the acrylic solution, and the laser shock peened surface was embedded in the acrylic solution).

4. Manually ground the sample with the Struers 320 (P-400) and 600 (P-1200) grit silicon carbide abrasive papers to thin the sample further down to about 100 – 200 μ m, and polished the surface with the Struers 1200 (P-2400) silicon carbide abrasive papers. The grinding and polishing machine for this step is Struers PlanoPol-2 at NSWCCD.
5. Mounted sample was left in the acetone solution for 24 hours to dissolve the acrylic mount and remove the sample.
6. Cleaned the residual acrylic from thinned sample with acetone, then rinsed off with water and ethanol.
7. Mechanically punched five thinned specimens from each sample out from a 3mm disk puncher.

After all the samples were prepared into 3mm disks, they were placed into a sample holder with a clear label on the sample holder. Next, all the samples were shipped to NRL for the second part of sample preparation and TEM analysis. The second part of the TEM sample preparation was performed by Dr. Ramasis Goswami at NRL, who generously agreed to help finalized the TEM sample preparation and performed the TEM analysis. Dr. Goswami is an expert on TEM analysis, especially with aluminum alloys. He has published numerous scientific papers on aluminum sensitization that included the use of TEM analysis. His works have been greatly cited by other researchers. Part 2 of the TEM sample preparation involved using a polisher to further mechanically thin the sample. The final thinning was performed by ion milling. The following steps describe Part 2 of the TEM sample preparation in more detail.

Part 2: TEM Sample Preparation at NRL

1. Mechanically polished the 3mm disc thickness down to around $30\mu m$.
For the laser shock peened sample, it was polished from the no laser shock peened side to preserve the laser shock peened area.
2. Final thinning of the 3mm disc using the Gatan Precision Model 691 Ion Mill with a gun voltage of 4kV and a sputtering angle of 10° at low temperature.

To characterize the effect of laser shock peening on the $Al_3Mg_2 \beta$ precipitation, dislocation density, dislocation configuration, and grain boundary precipitation, the Tecnai Analytical Transmission Electron Microscope was used.

○ 3.4.6. *Transmission Electron Microscopy Results*

The TEM analysis and imaging was performed by Dr. Goswami. He observed several differences, such as dislocation density, dislocation configuration, preferred precipitation site, and thermal effect between the as-received unpeened (U10) and laser shock peened (P18) unaged samples. First, based on observing the dislocation images taken at multiple sites within both samples, he pointed out that there is an increase in dislocation density between U10 and P18 samples, shown in Figure 17 (a) and (b). To confirm the increase of dislocation density, a quantitative study measuring the dislocation density of each sample was conducted and is discussed in Section 3.4.7 and Section 3.4.8.

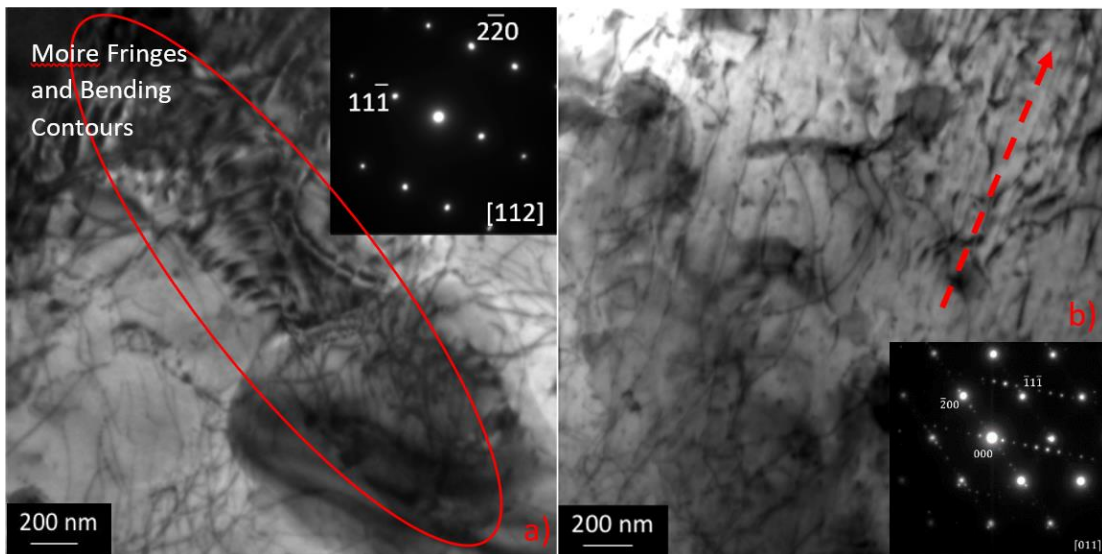


Figure 17. (a) TEM brightfield dislocation image for U10 sample with a [112] zone axis. (b) TEM brightfield dislocation image for P18 sample with a [011] zone axis.

The dislocation configuration, shown in Figure 18 (a) and (b), has a preferential dislocation direction (red arrow) for the P18 sample. The U10 sample has apparently randomly oriented dislocations. The TEM dislocation configurations can also be seen in Figure 17 (a) and (b).

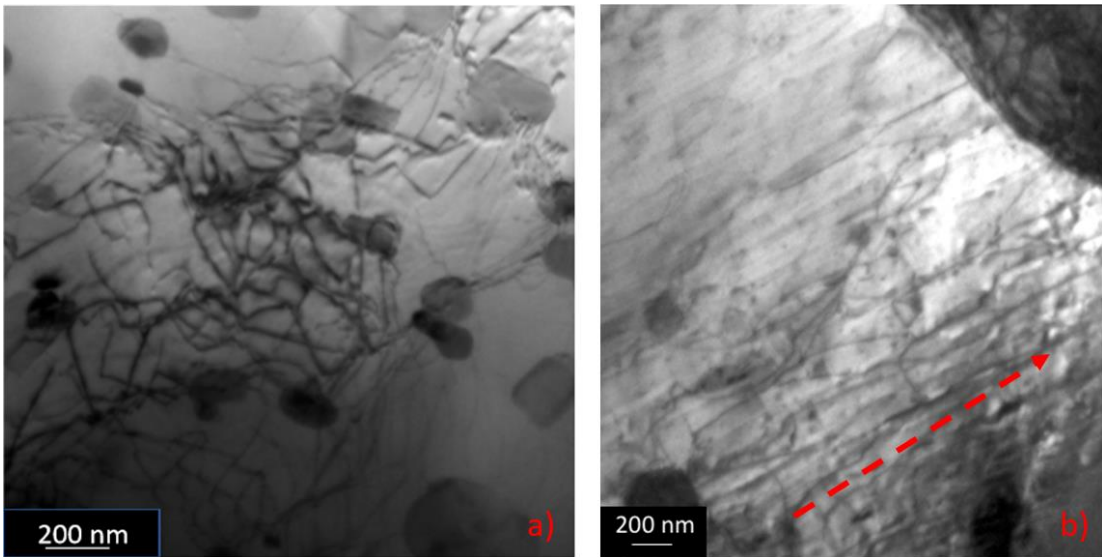


Figure 18. (a) Randomly orientated dislocations for sample U10. (b) Preferential dislocations direction (marked with red arrow) for sample P18.

Fine precipitations on dislocations are only observed in the P18 samples and not on dislocations in the U10 sample. Those fine precipitations could possibly be the Al_3Mg_2 β phase precipitates. Further analysis is required to confirm the chemical composition of the fine precipitations. Furthermore, in both U10 and P18 samples, Al-Mn-Fe type of dispersoids are found located near dislocations and appear to pin the dislocation. Figure 19 (a) shows the Al-Mn-Fe type dispersoids pinning the dislocations in the U10 sample, and in Figure 19 (b), the fine precipitates on dislocations.

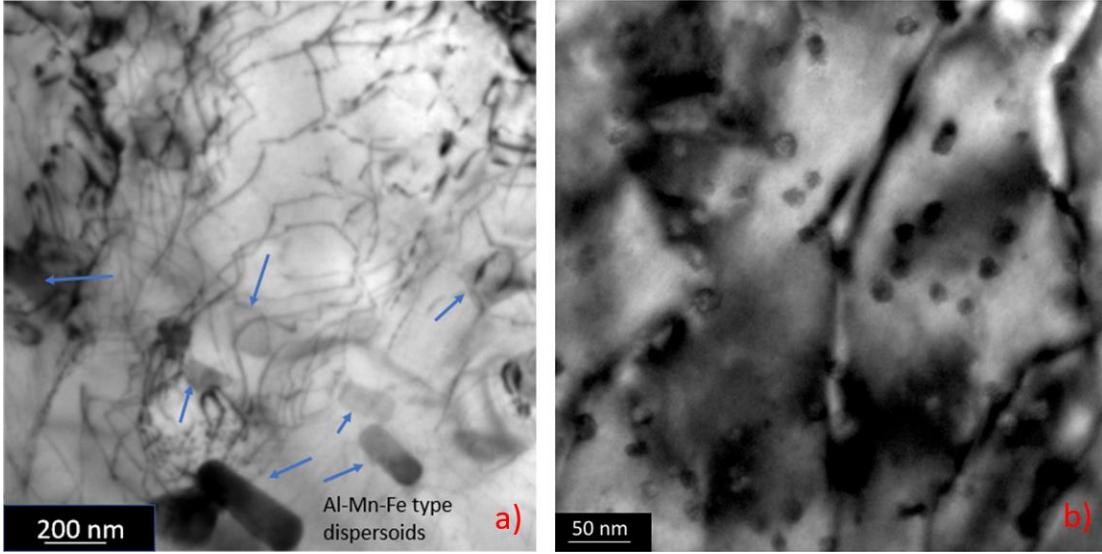


Figure 19. (a) Al-Mn-Fe type of dispersoids pinned dislocation in the U10 sample.
 (b) Fine precipitates on dislocation.

The melt pool caused by the penetration of laser beam from laser shock peening process has been observed on the P18 sample surface, shown in Figure 20. The affected melting spot has a horizontal diameter of 934.11nm and a vertical diameter of 900.36nm. The melt pools have been consistently found on the P18 sample surface.

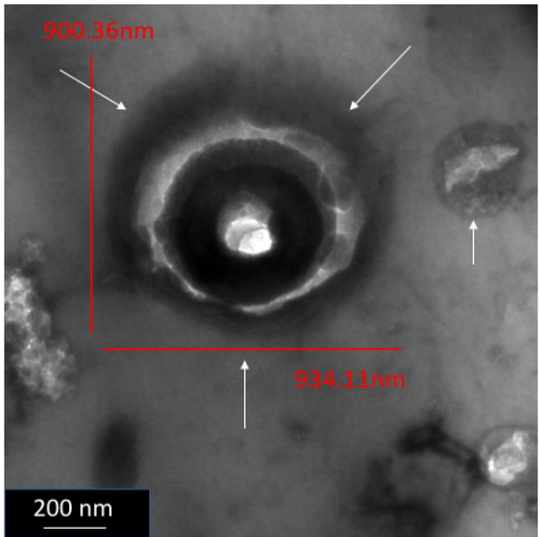


Figure 20. Melt pool from the penetration of laser beam appears in the P18 sample surface.

○ 3.4.7. Dislocation Density Measurement

The line-intercept method is the most commonly used method to measure the dislocation density in a TEM image [64, 65]. Line-intercept method involves placing five randomly drawn lines on a TEM image and counts the total number of intersections the drawn lines make with dislocations. An example of line-intercept method is shown in Figure 21.

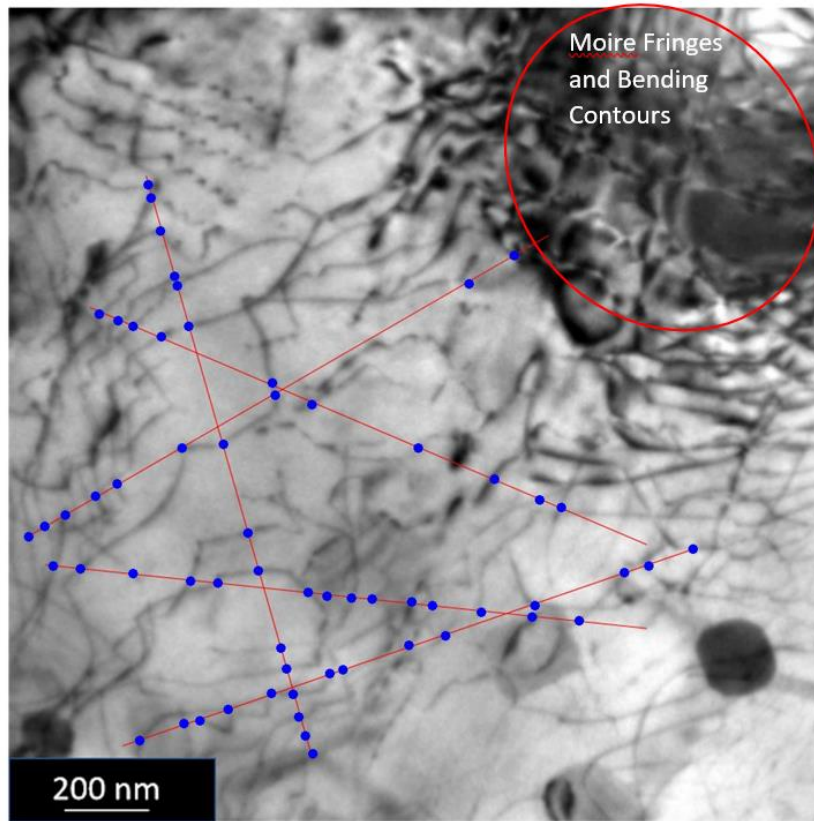


Figure 21. Dislocation density measurement by using the line-intercept method.

The dislocation density ($\rho_{dislocation}$) can be calculated by using Equation (9).

$$\rho_{dislocation} = \frac{N}{Lt} \quad (9)$$

N is the total number of intersections between dislocations and the five drawn lines, L is the total length of all the drawn lines, and t is the thickness of the specimen. The

TEM sample thickness used for calculating the dislocation density is approximately 100nm. Moreover, to minimize possible bias during measurement, five different TEM dislocation images for both unaged laser shock peened and unpeened samples were measured.

○ 3.4.8. Dislocation Density Measurement Results

The line-intercept method was used to measure the dislocation density in the unaged laser shock peened and unpeened samples. Dislocation density measurements were performed at five different locations within each sample. The values of average dislocation density for each sample are listed in Table 10.

Table 10. Average dislocation density of U10 and P18.

Sample	Average Dislocation Density	TEM Sample Thickness
U10 (Unaged and no laser shock peened)	7.9534×10^{-5} per nm^2 7.9534×10^{13} per m^2	About 100nm
P18 (Unaged and laser shock peened)	3.7773×10^{-4} per nm^2 3.7773×10^{14} per m^2	About 100nm

Based on the measurements, the unaged laser shock peened sample has a higher dislocation density than the unaged unpeened sample. The difference between unaged laser shock peened and unpeened samples is by a factor of 4.7.

Chapter 4: Finite Element Method (FEM) Modeling

Finite element method (FEM) modeling is used in this study to simulate the effect of impact force from the laser shock peening process on AA5083-H116 aluminum alloy surface. FEM modeling is widely used in different kinds of engineering applications as it can provide rapid results and predictions. Utilizing FEM modeling can significantly reduce the amount of time, energy, cost, and material usage during actual experimental testing and provide valuable simulation of material behavior in both macroscopic and microscopic scales. In order to understand the behavior of surface deformation during laser shock peening process, stress and strain distributions and deformation depth changes of the sample were modeled.

- 4.1. Assumptions and Modeling Procedures

Prior to the creation of a FEM model, sample dimensions and the laser shock pulse effective area are carefully measured to provide accurate simulations and results. Moreover, a few assumptions have to be made in order for this project to be feasible within the given time frame, resources and computing power. The first assumption is that during the application of the laser shock peening process, each laser shock pulse did not overlap with the previous laser shock peened areas. The second assumption is that each laser shock peened affected area has a perfect circular shape with the same diameter. The last assumption is that the material properties have an isotropic linear elastic and bilinear plasticity behavior.

During the FEM modeling process several modeling software were used. Table 11 lists the software names and usage in this FEM modeling.

Table 11. List of software used and the purpose for the FEM modeling.

Software Name	Usage Description
SolidWorks 2019	Creating 3D geometry model
ANSYS 19.4 Workbench	Mechanical properties simulation

SolidWorks 2019 was the preprocessor that was used to create the 3-Dimensional (3D) geometry structure for the FEM modeling. Due to the actual sample being highly symmetrical, the FEM modeling geometry only have to simulate 1/8 of the actual sample. The laser shock pulse affected area was measured from the actual sample surface, where there are small arrays of aligned circles with an approximate diameter of 6.35mm (0.25in). The array of aligned circles on the actual sample surface is shown in Figure 22.



Figure 22. The array of circles appears on the laser shock peened sample surface. The diameter of each circle is about 6.35mm (0.25in).

To simulate the effect of the laser shock peening process with the two-layer application, a total of seven solid circular tube bodies are generated at the center of the modeling sample to represent the laser shock pulses. The seven solid circular tube bodies form into a shape where there is a central solid circular tube body surrounded by six other solid circular tube bodies (packed like a (111) plane in the f.c.c. structure). This shape will allow the FEM model to simulate not only the effect of laser shock pulse but also the interaction between the surrounding laser shock peened areas. Figure 23 shows the relation between the actual sample geometry, the modeling sample geometry, and the affected laser shock peening area created in SolidWorks 2019. The dimensions of the actual sample, the modeling sample, and laser shock peening affected area are listed in Table 12.

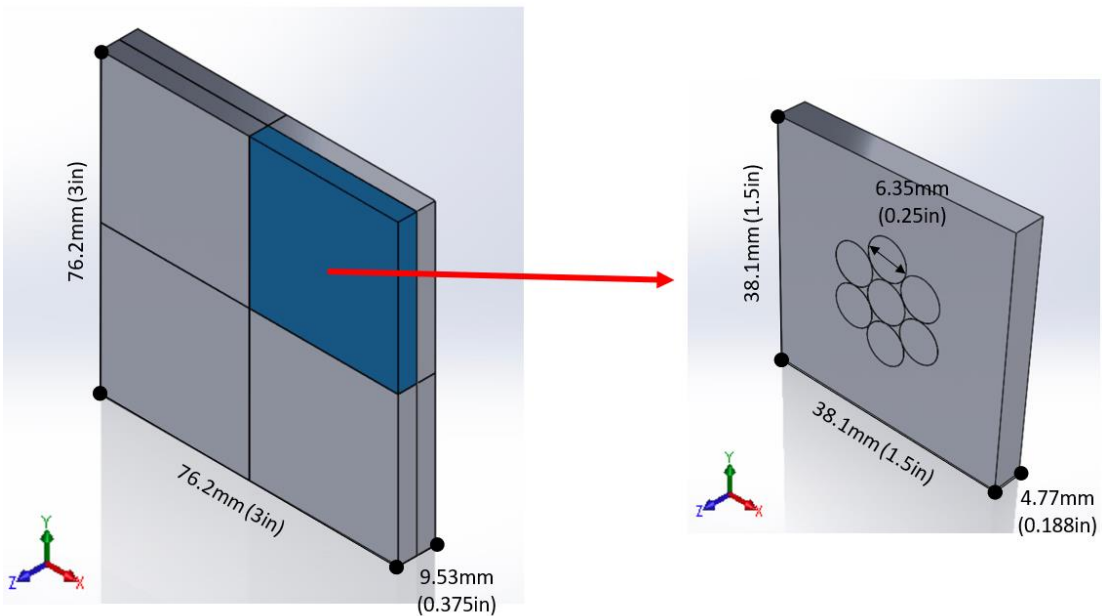


Figure 23. The actual sample and the modeling sample. The modeling sample is 1/8 of the actual sample. The diameter of the laser shock peening affected area is 6.35mm (0.25in).

Table 12. Dimensions of the actual and modeling sample and the laser shock peening affected area.

	Actual Sample	Modeling Sample
Length	76.2mm (3in)	38.1mm (1.5in)
Width	76.2mm (3in)	38.1mm (1.5in)
Thickness	9.53mm (0.375in)	4.77mm (0.188in)
Laser Shock Peening Affected Area		
Diameter	6.35mm (0.25in)	
Area	$31.67mm^2$ ($0.04909in^2$)	

After the 3D model was created, the file was imported into ANSYS 19.4 Workbench as an Initial Graphics Specification (IGS) file.

The mechanical FEM analysis was performed in ANSYS 19.4 Workbench. The laser shock peening process simulated in the FEM model followed the same laser shock peening process for the real sample. The water and opaque black overlays were not included in the model because this FEM simulation was purely testing the mechanical behavior of the material, and the thermal effect was neglected. In ANSYS 19.4 Workbench, the analysis system is categorized in the transient analysis because laser shock peening process is a work done on the sample surface as a function of time. The transient structural analysis can capture the effect of laser shock peening on the sample within each time frame or time step. Next, the material properties of AA5083-H116 were added to the software's Engineering Data. The material properties entered are listed in Table 13 [11, 66].

Table 13. Inputted AA5083 – H116 mechanical properties.

AA5083 – H116	
Density	$2770 \frac{kg}{m^3}$
<i>Linear Elasticity</i>	
Elastic Modulus	$7.1 \times 10^{10} Pa$
Poisson's Ratio	0.33
<i>Non-Linear Elasticity – Bilinear Isotropic Hardening</i>	
Proportional Limit	$2.75 \times 10^8 Pa$
Tangent Modulus	$1.08 \times 10^9 Pa$

It is critical to know when and where the material start to plastically deform, so the proportional limit for yield strength was used instead of the 0.2% offset. The proportional limit and tangent modulus were gathered from the AA5083-H116 engineering stress – strain curve, shown in Figure 24 [66].

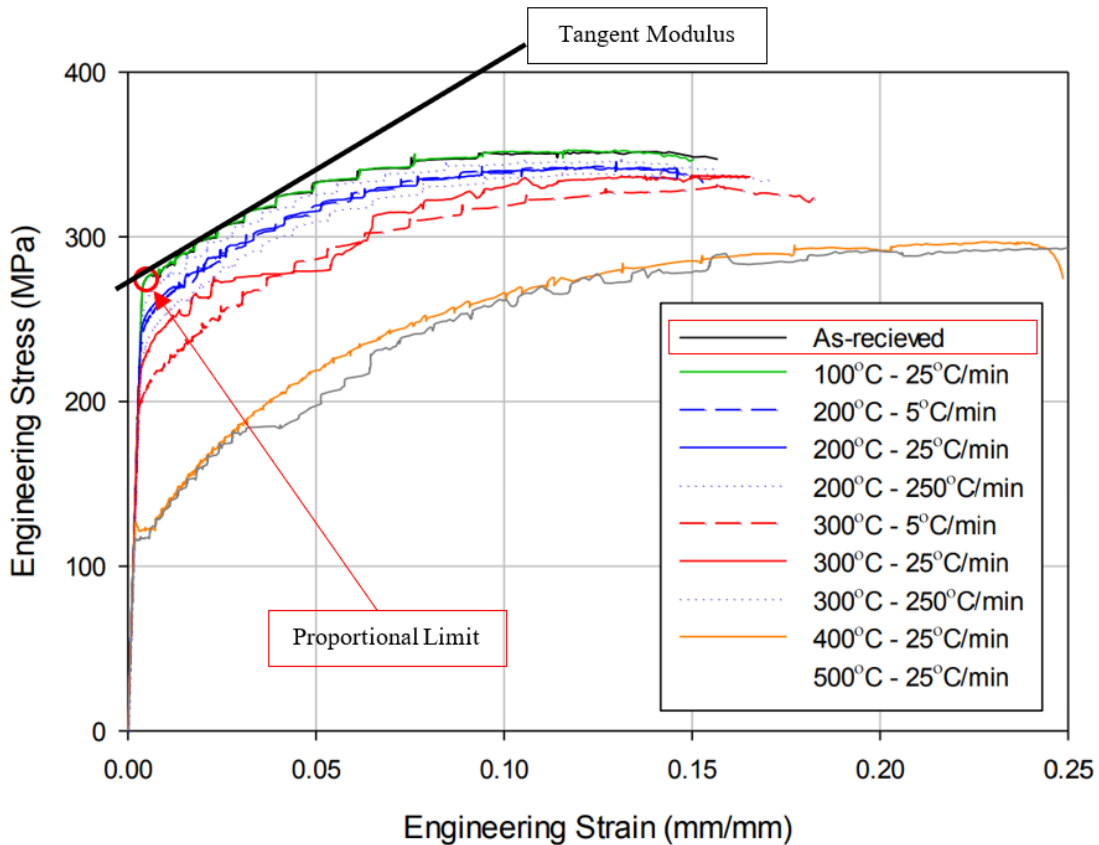


Figure 24. AA5083-H116 engineering stress – strain curve.

After entering the material properties into the ANSYS Workbench Engineering Data, the IGS file with 3D structure created from SolidWorks 2019 was imported into ANSYS 19.4 Workbench. The next step was to open the ANSYS Workbench Mechanical and made sure each 3D bodies created in SolidWorks correctly showed up in ANSYS Workbench. Next, all the 3D bodies were assigned with the correct material properties from the Engineering Data. Sometime when transferring 3D geometry from SolidWorks to ANSYS Workbench, the bodies were not correctly bonded. Thus, it is important to make sure the connection between each body is bonded correctly.

Next, the mesh is applied. The mesh near the circular tubes region is finer than the mesh around the region far away from the circular tubes. This kind of mesh application will provide more accurate results while keeping the calculation time short. The finer the mesh, the more accurate the result as more data points are interpreted and calculated. Figure 25 shows the mesh application on the modeling geometry.

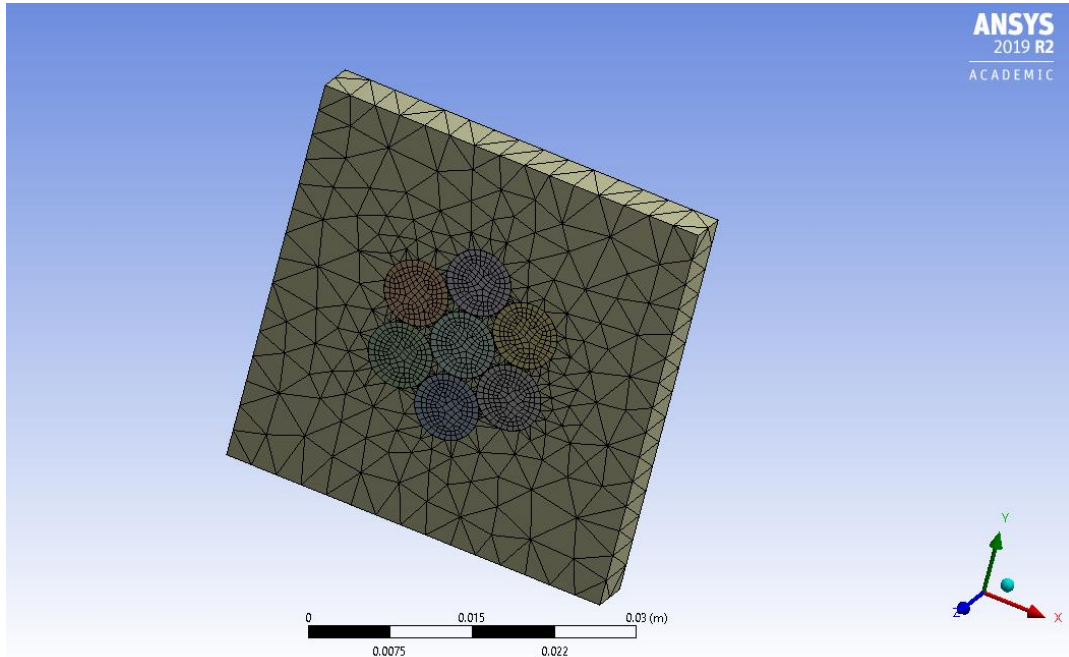


Figure 25. Mesh application and mesh size distribution.

The three constraints were applied on the model:

- On the back XY plane ($x, y, 0$) with $Z = 0$ mm displacement
- On the bottom XZ plane ($x, 0, z$) with $Y = 0$ mm displacement
- On the left YZ plane ($0, y, z$) with $X = 0$ mm displacement

This allows the structure to move freely in the X and Y direction on the (x, y, 0) plane, in the X and Z direction on the (x, 0, z) plane, and in the Y and Z direction on the (0, y, z) plane. Figure 26 provides a schematic view of the constraints.

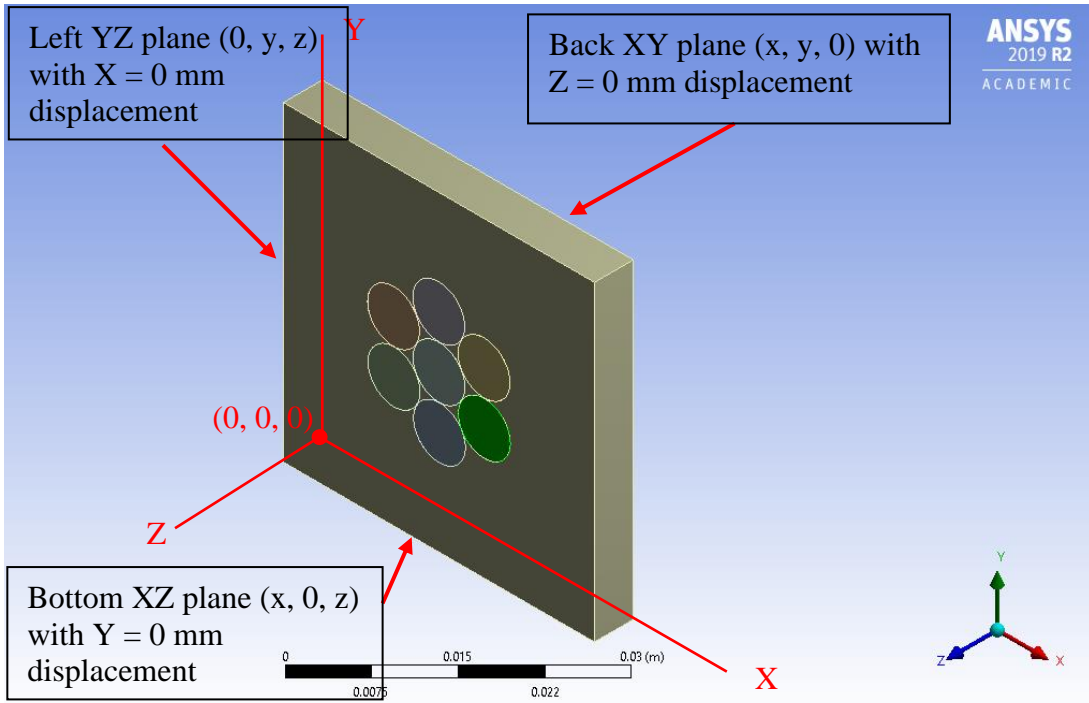


Figure 26. Model constraints.

The last step of setting up the FEM model was to assign the calculated force to the correct time steps in the Analysis Setting. The value of force used in this simulation was calculated based on Equation (1), Equation (2), and Equation (3) [67].

$$Pressure \text{ (GPa)} = 0.01 \sqrt{\frac{\alpha}{\alpha+3}} \sqrt{Z} \sqrt{I_0} \quad (1)$$

α is the fraction of the internal energy devoted to the thermal energy, and it is typically about 0.25. I_0 is the incident power density. Z is the reduced shock impedance between the target and the confining water, which can be found by using Equation 2.

$$\frac{2}{Z} = \frac{1}{Z_{water}} + \frac{1}{Z_{target}} \quad (2)$$

$$Z_{water} = 0.165 \times 10^6 \frac{g}{cm^2 s^{-1}}$$

$$Z_{Al} = 1.5 \times 10^6 \frac{g}{cm^2 s^{-1}}$$

$$Pressure = \frac{Force}{Area} \quad (3)$$

Therefore, by using Equation 1, Equation 2, and $4 \frac{GW}{cm^2}$ for the incident power density, the maximum pressure generated during the laser shock peening process is 3.0245 GPa. To convert pressure to force, apply Equation 3 with the affected laser shock peening area of $3.167 \times 10^{-5} m^2$ and get $-95,785N$ for the force generated on one laser shock peening affected area. The applied force is negative to indicate the force is applied into the target. In order to properly assign the force to the corresponding time step, it is important to understand each step during the two-layer application of laser shock peening process. The two-layer application laser shock peening process can be seen as 4 steps:

1. Step 1: The laser shock pulse only applied in one area
2. Step 1 + Step 2: The laser shock pulse first applied at the Step 1 area and then applied separately to each of the surrounding areas
3. Step 1 + Step 2 + Step 3: The laser shock pulse first applied at the Step 1 area, then applied separately to each of the surrounding areas, and reapplied back to the Step 1 area

4. Step 1 + Step 2 + Step 3 + Step 4: The laser shock pulse first applied at the Step 1 area, then applied separately to each of the surrounding areas, reapplied back to the Step 1 area, and reapplied separately to each surrounding areas

Figure 27 illustrates Step 1 to Step 4 of the two-layer application laser shock peening process.

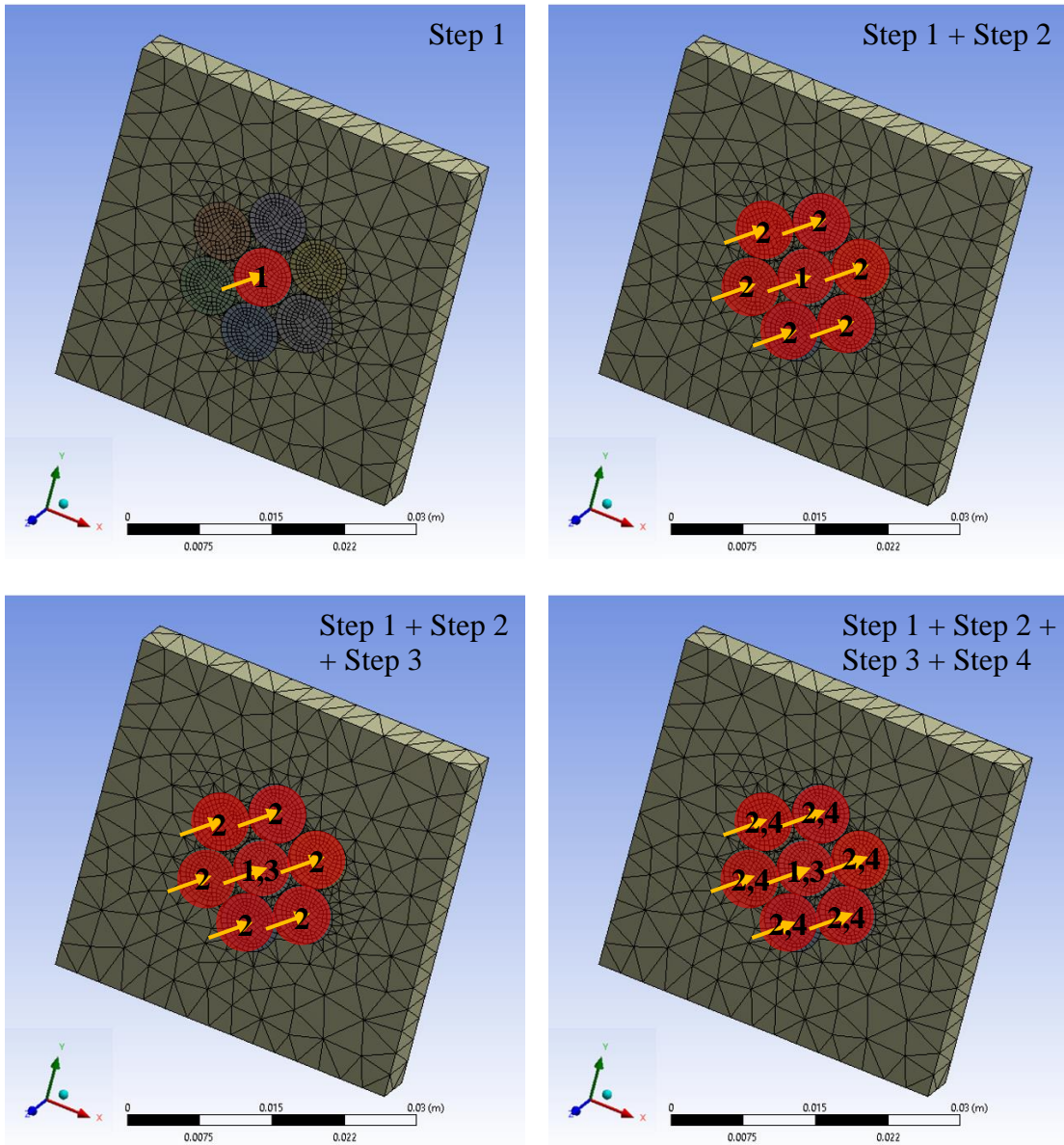


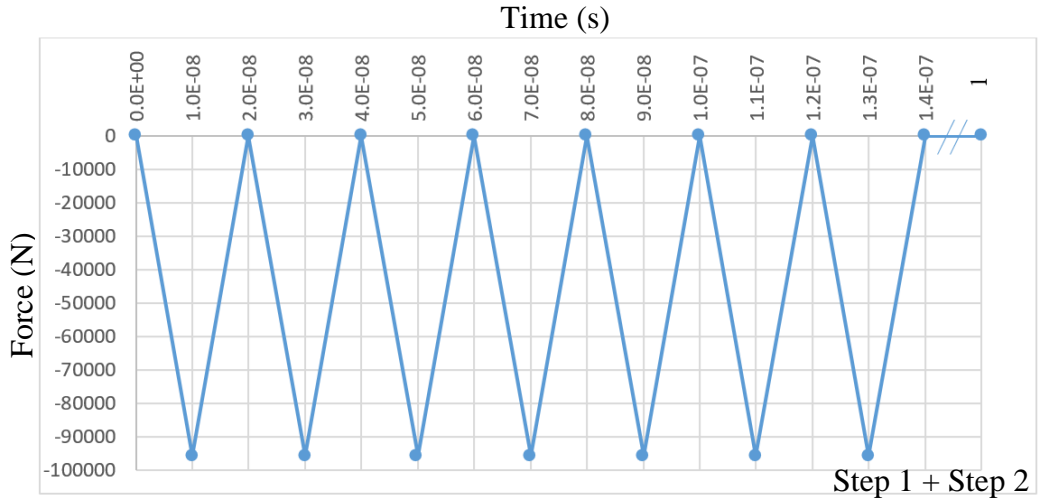
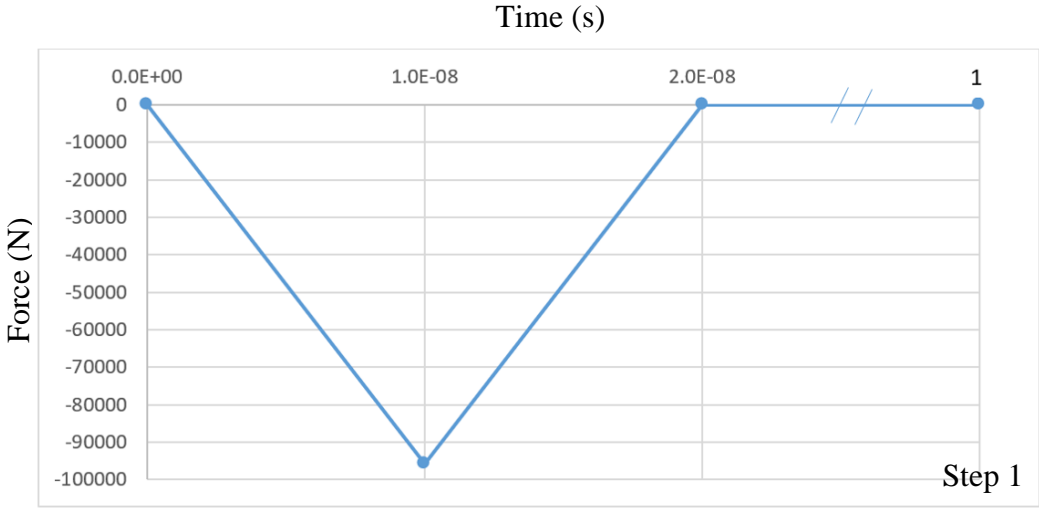
Figure 27. Two-layer laser shock peening process in four steps.

The duration of each laser shock peen is 20ns, and this FEM simulation neglected the time for the laser machine to move from one spot to another as the distance between each laser shock peening spot is small. The applied force and corresponding time for Step 1 to Step 4 of the laser shock peening process is shown in Table 14 (orange = loading condition and green = unloading condition) and graphical representation is shown in Figure 28.

Table 14. Applied force and corresponding time for Step 1 to Step 4.

Time (s)	Step 1 Force (N)	Step 1 + 2 Force (N)	Step 1 + 2 +3 Force (N)	Step 1 + 2 + 3 + 4 Force (N)
0	0	0	0	0
1E-08	-95783	-95783	-95783	-95783
2E-08	0	0	0	0
3E-08	0	-95783	-95783	-95783
4E-08	0	0	0	0
5E-08	0	-95783	-95783	-95783
6E-08	0	0	0	0
7E-08	0	-95783	-95783	-95783
8E-08	0	0	0	0
9E-08	0	-95783	-95783	-95783
1E-07	0	0	0	0
1.1E-07	0	-95783	-95783	-95783
1.2E-07	0	0	0	0
1.3E-07	0	-95783	-95783	-95783
1.4E-07	0	0	0	0
1.5E-07	0	0	-95783	-95783
1.6E-07	0	0	0	0
1.7E-07	0	0	0	-95783
1.8E-07	0	0	0	0
1.9E-07	0	0	0	-95783
2E-07	0	0	0	0
2.1E-07	0	0	0	-95783
2.2E-07	0	0	0	0
2.3E-07	0	0	0	-95783
2.4E-07	0	0	0	0
2.5E-07	0	0	0	-95783
2.6E-07	0	0	0	0
2.7E-07	0	0	0	-95783

2.8E-07	0	0	0	0
1	0	0	0	0



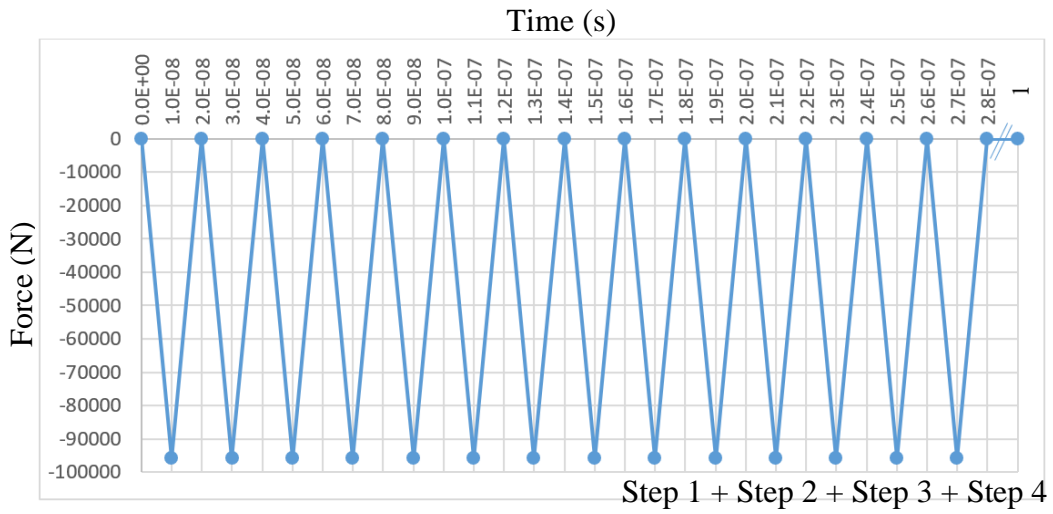
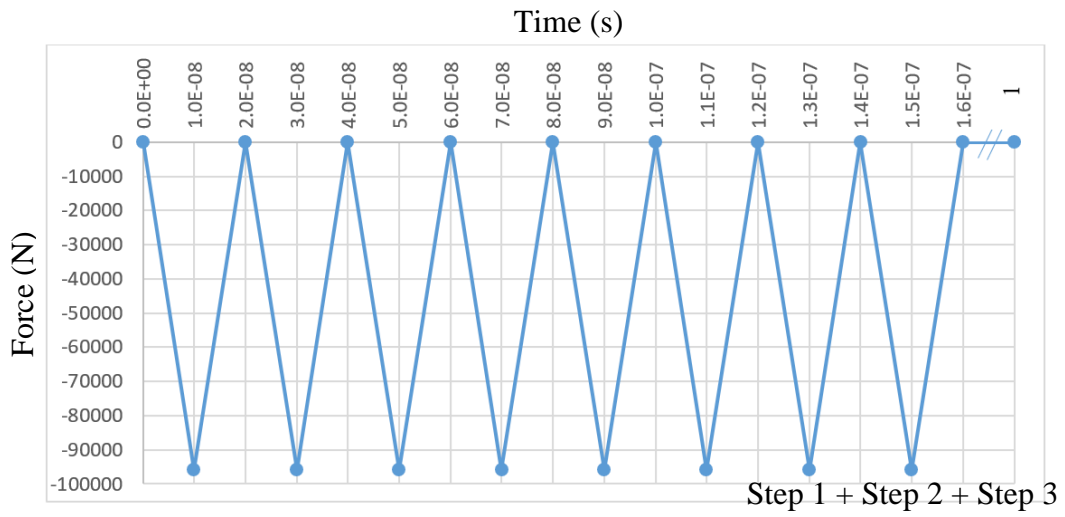


Figure 28. Graphical representations of applied force (N) and corresponding time (s) for Step 1 to Step 4.

The model was solved and used obtained the von-Mises Stress, Z-axis displacement, Z-axis normal stress and strain, and the hydrostatic stress. Since ANSYS Workbench does not have hydrostatic stress preprogrammed as one of the results, hydrostatic stress had to be defined. Hydrostatic stress can be calculated based Equation (4).

$$\sigma_{Hydrostatic} = \frac{\sigma_x + \sigma_y + \sigma_z}{3} \quad (4)$$

σ_x , σ_y , and σ_z are stress in the x, y, and z direction, respectively. To show hydrostatic stress results in ANSYS Workbench, Equation (4) had to be manually added as $\frac{(\sigma_x + \sigma_y + \sigma_z)}{3}$ to the “User Defined Results” option.

The following list provides the general steps for setting up and performed the laser shock peening process FEM simulation in ANSYS 19.4 Workbench.

1. Select Transient Structural analysis system
2. Input AA5083-H116 mechanical properties into Engineering Data
3. Import the IGS file of 3D structure created from SolidWorks 2019
4. Assign the material properties from Engineering Data to the 3D structure
5. Create a mesh profile for the 3D structure (Finer mesh near the circular tubes)
6. Apply constraints at the back XY plane with Z = 0mm displacement, bottom XZ plane with Y = 0mm displacement, and left YZ plane with X = 0mm displacement
7. Assign appropriate time, time steps, and calculated force in the Analysis Setting
8. Solve and view the von-Mises Stress, Z-axis displacement, Z-axis normal Stress and strain, and the hydrostatic stress.

- 4.2. Validation

To ensure the FEM models and results generated from the software were accurate, three validation tests were performed prior to running the actual models. All three validation tests were testing the material's mechanical properties within the elastic region. In the material's elastic region, any deformation, stress, and strain must return to zero once the applied load is removed and the material is not experiencing any load. Moreover, under the elastic loading condition, the stress the material experiences are divided by the strain the material experiences and should return the material's elastic modulus. The following sections describe the three validation testing conditions and results.

- *4.2.1. Test 1: Elastic Modulus Check (Large Region)*

The first FEM model validation check was applying a known, calculated compressive stress, σ , on the entire front XY plane where $Z \neq 0$. The applied compressive stress was calculated by multiplying the elastic strain, ϵ , (gathered from Figure 24 the stress-strain curve) with material's elastic modulus, E. By using the elastic strain to calculate the applied stress, the model should behave elastically. The following calculation shows the process of obtaining the applied stress.

$$\epsilon = 0.003 \frac{mm}{mm} \text{ (gathered from the stress – strain curve)}$$

$$E = 7.1 \times 10^{10} Pa$$

$$\sigma = E\epsilon = (7.1 \times 10^{10})(0.003) = -2.13 \times 10^8 Pa$$

(The negative sign was added to indicate it is a compressive stress)

The model was constrained the same way as previously mentioned in Section 4.1. Back XY plane (x, y, 0) with Z = 0 mm displacement, bottom XZ plane (x, 0, z) with Y = 0 mm displacement, and left YZ plane (0, y, z) with X = 0 mm displacement. After all the material properties, constraints, and compressive stress were correctly assigned to the model, the model was solved for the stress and strain in the Z direction during loading.

The validity of the model was checked by first compared the maximum Z direction stress value to the applied compressive stress value, which the values are very similar. Then, the elastic modulus was calculated by dividing the average Z direction stress by the average Z direction strain. The calculated elastic modulus is the same as the actual material elastic modulus. Table 15 shows the FEM results and calculated values. Figure 29 and Figure 30 are visual diagrams of the results.

Table 15. Validation test 1 FEM results.

Z Stress	$-2.13 \times 10^8 \text{ Pa}$
Z Strain	$-2.9998 \times 10^{-3} \frac{m}{m}$
Calculated Elastic Modulus from FEM Results	$E = \frac{-2.13 \times 10^8}{-2.9998 \times 10^{-3}} = 7.1 \times 10^{10} \text{ Pa}$

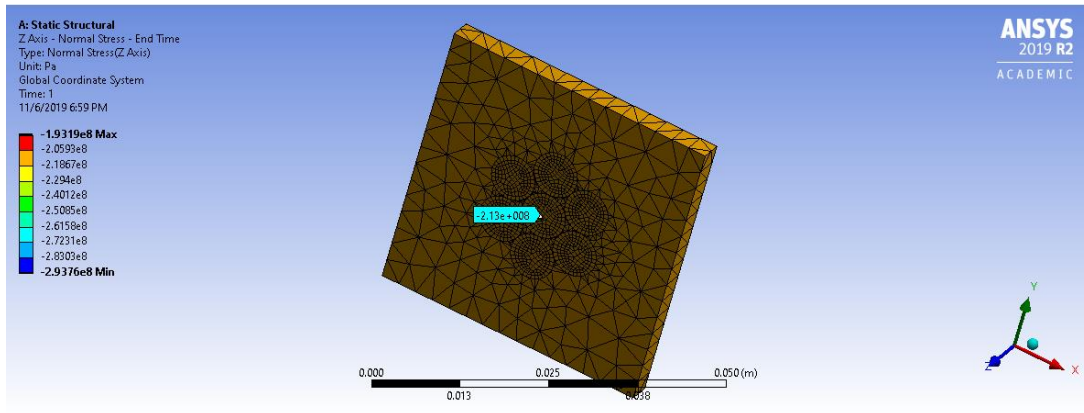


Figure 29. Validation Test 1: Z stress result.

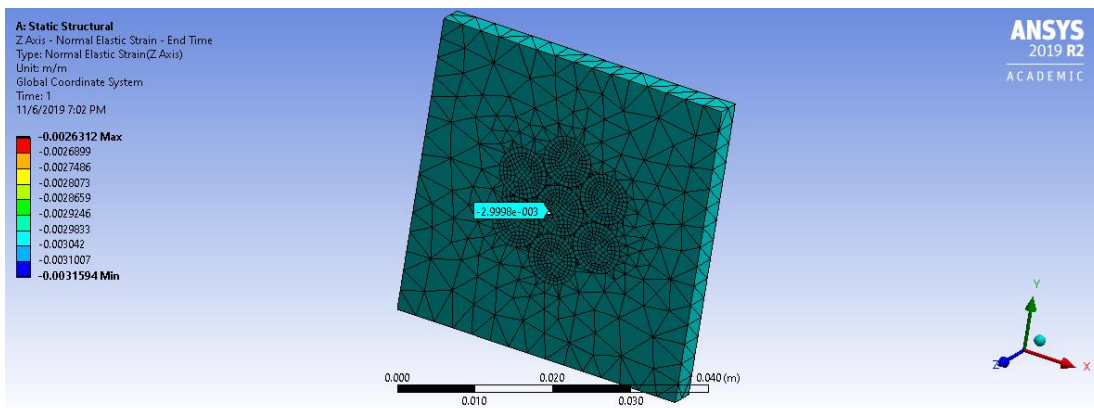


Figure 30. Validation Test 1: Z strain result.

○ 4.2.2. Test 2: Zero Deformation, Stress, and Strain Check (Large Region)

The second validation test is based on the setting from Test 1 and removed the applied stress from the material. The main goal is to check if the material comes back to its original shape with zero stress and strain remain in the material. As Test 1 was testing within the elastic region, the structure should not experience any permanent deformation and plastic strain. Figure 31, Figure 32, and Figure 33 show no permanent deformation and zero stress and strain in Z direction in the material after the applied stress is removed.

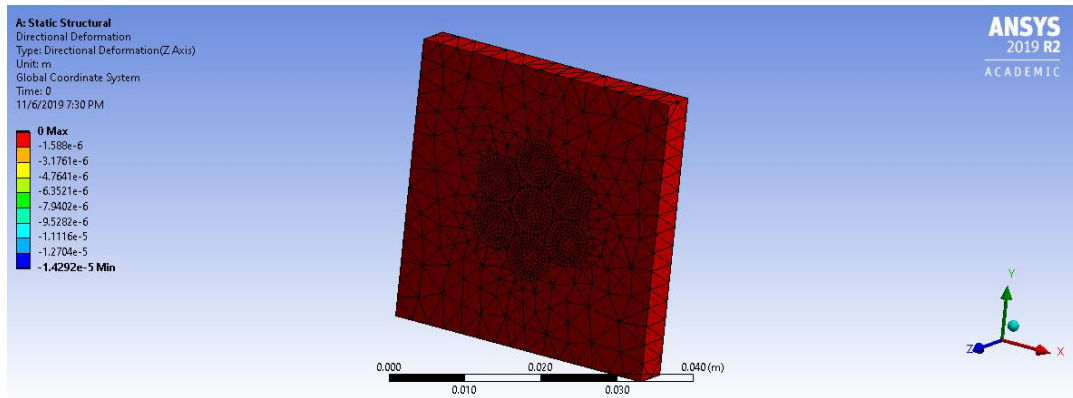


Figure 31. Validation Test 2: Deformation in Z direction after the load is removed.

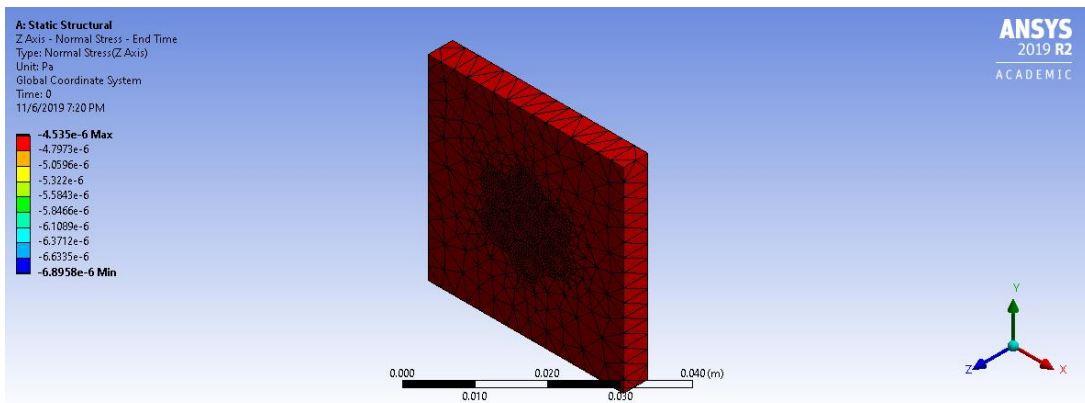


Figure 32. Validation Test 2: Stress in Z direction after the load is removed.

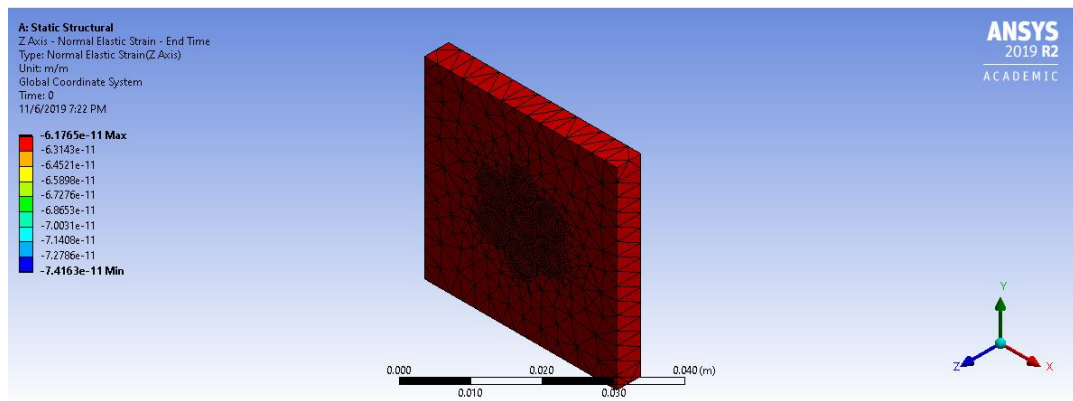


Figure 33. Validation Test 2: Strain in Z direction after the load is removed.

○ 4.2.3. Test 3: Zero Deformation, Stress, and Strain Check (Small Region)

The third validation test is to check if the model will behave the same way as Test 2 when the same amount of compressive stress from Test 1 is applied on a smaller region. A compressive stress of $-2.13 \times 10^8 \text{ Pa}$ was applied at the center circular area on the front XY plane with $Z \neq 0$, shown in Figure 34. After the load is removed, both the load applied area and the entire surface region were checked to see if the model came back to its original shape and with no plastic deformation and strain remaining in the structure. Figure 35, Figure 36, and Figure 37 shows that there is no plastic deformation, stress, and strain remained in the material after the load is removed from the small applied region.

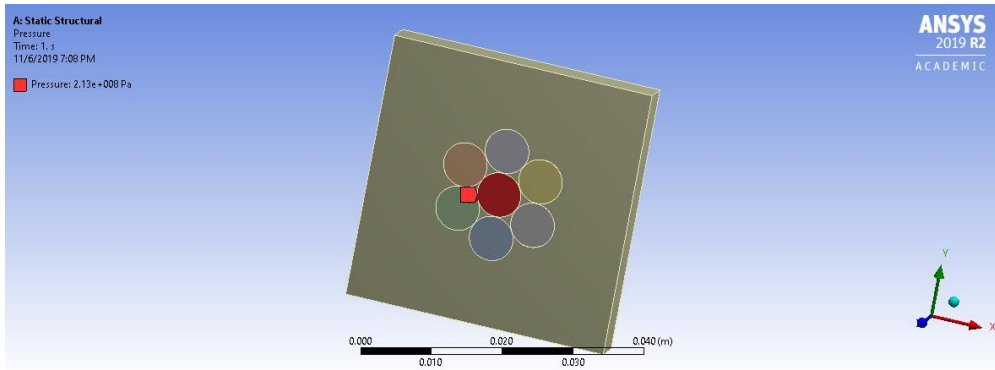


Figure 34. Force applied at a small region.

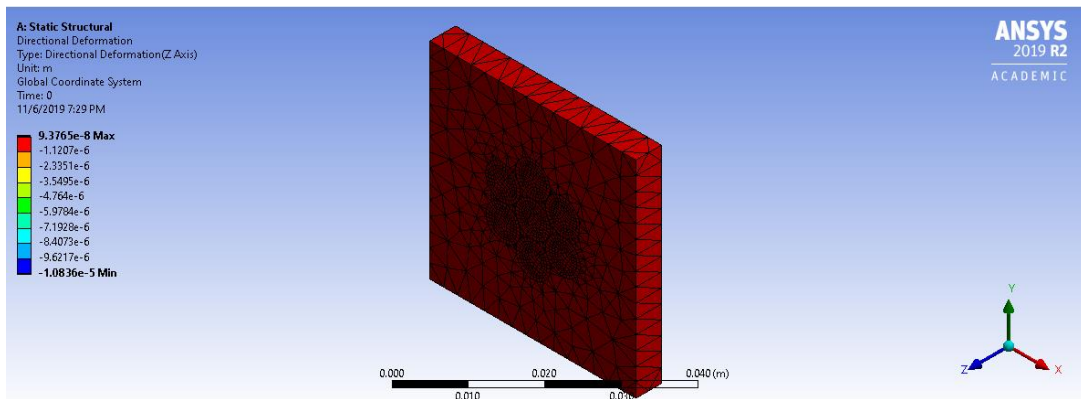


Figure 35. Validation Test 3: Deformation in Z direction after the load is removed.

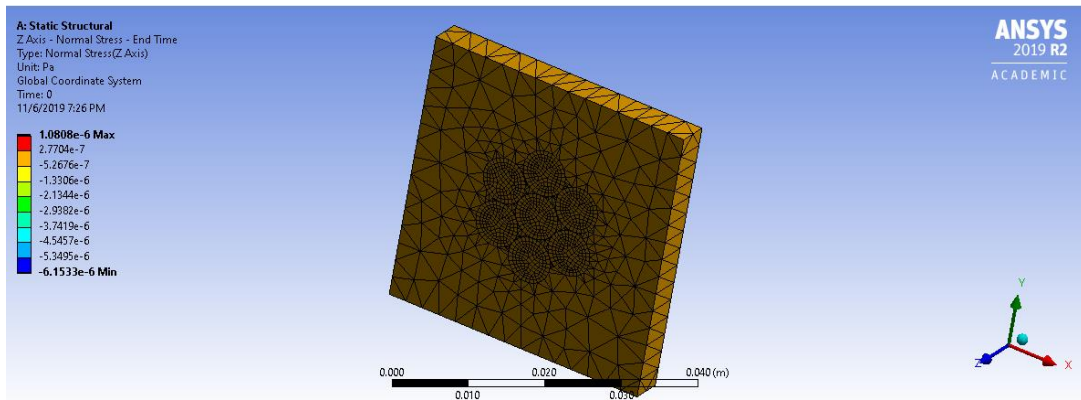


Figure 36. Validation Test 3: Stress in Z direction after the load is removed.

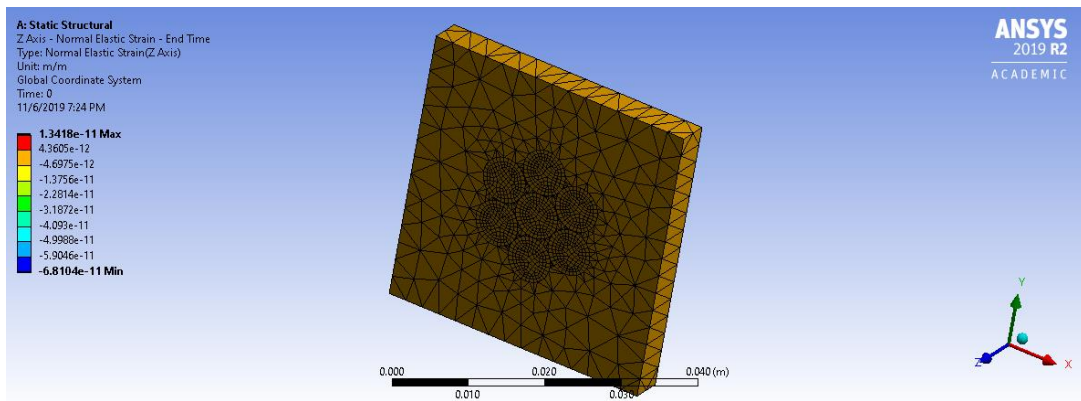


Figure 37. Validation Test 3: Strain in Z direction after the load is removed.

- 4.3. Results

The FEM results provide clear visual representations and in-depth analyses of the two-layer laser shock peening process. In each step, the Z direction displacement, Z direction stress and strain, and von-Mises stress were interpreted. Moreover, the residual stress, residual stress depth, and type of residual stress are also measured for the unloaded condition. In the final step, the hydrostatic stress was calculated in addition to all other stress results. The depth of each measurement was taken from the central circular region and the average of four different depth measurements within the region. For this FEM modeling, there are four steps simulating the two-layer laser shock peening process. Visual representations are shown in Figure 27. Within each of the four steps, there are two sub-steps that simulate the loaded and unloaded laser shock peening conditions. Furthermore, in order to measure the affected depth of each of the steps, a YZ section plane is made and inserted in the middle of the sample. Figure 38 shows the YZ section plane and the place of insertion. The following sections show individual FEM results for each steps and conditions. Table 24 summarizes all the Z-axis displacement, Z-axis Normal Stress and strain, von-Mises stress, hydrostatic stress, residual stress, and depth of plastic stress and residual stress for all the steps.

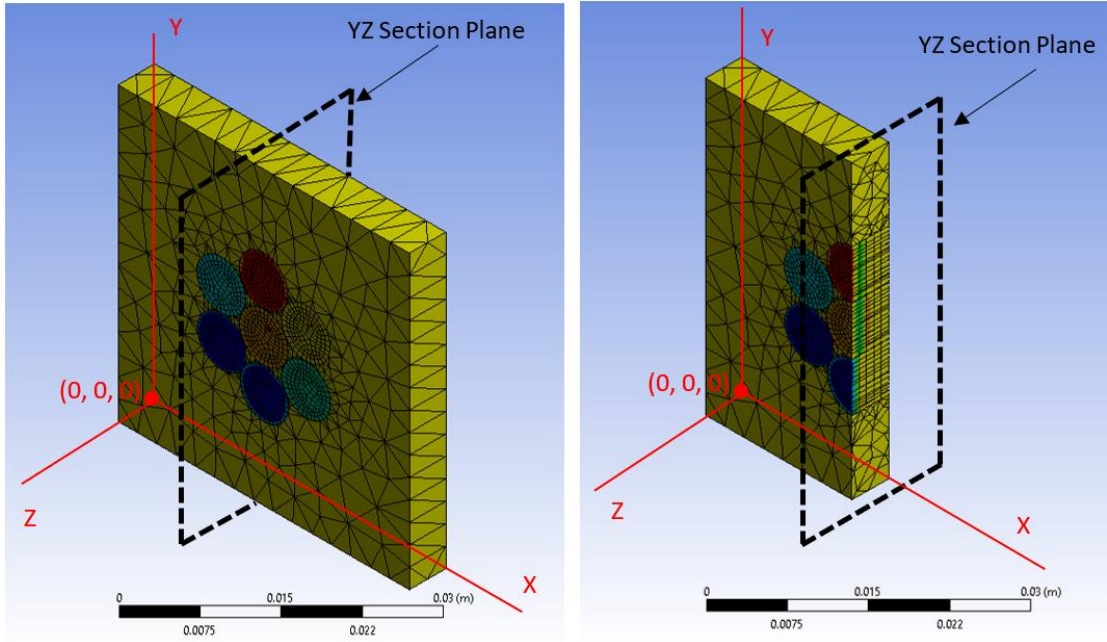


Figure 38. YZ section plane and place of insertion.

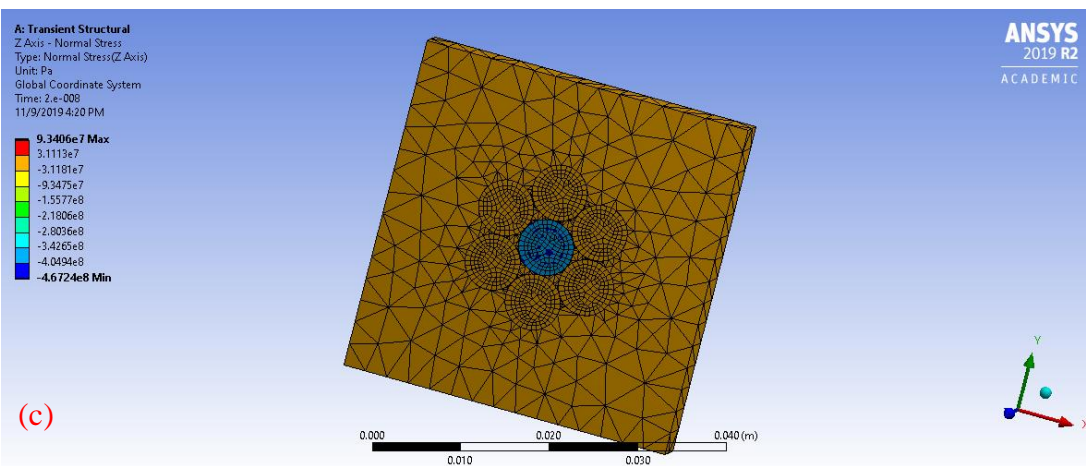
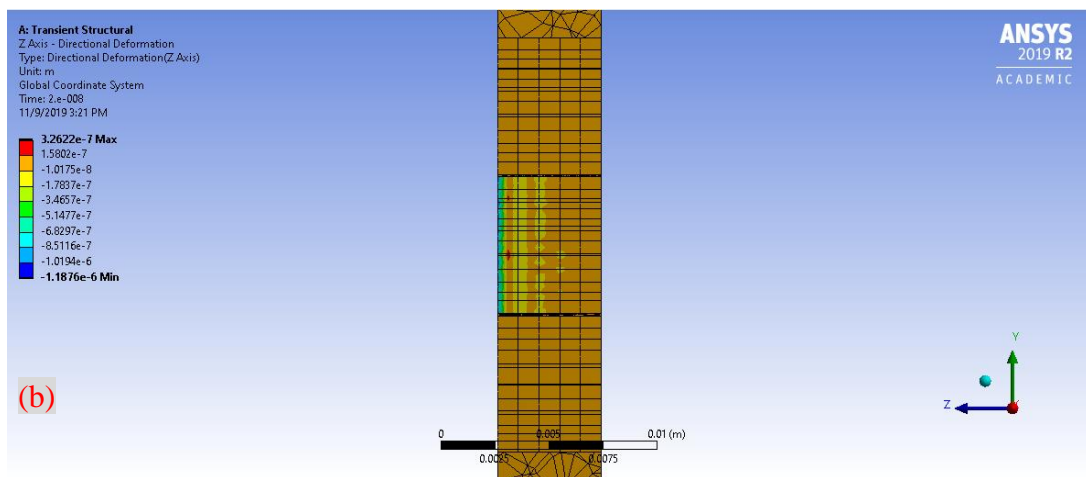
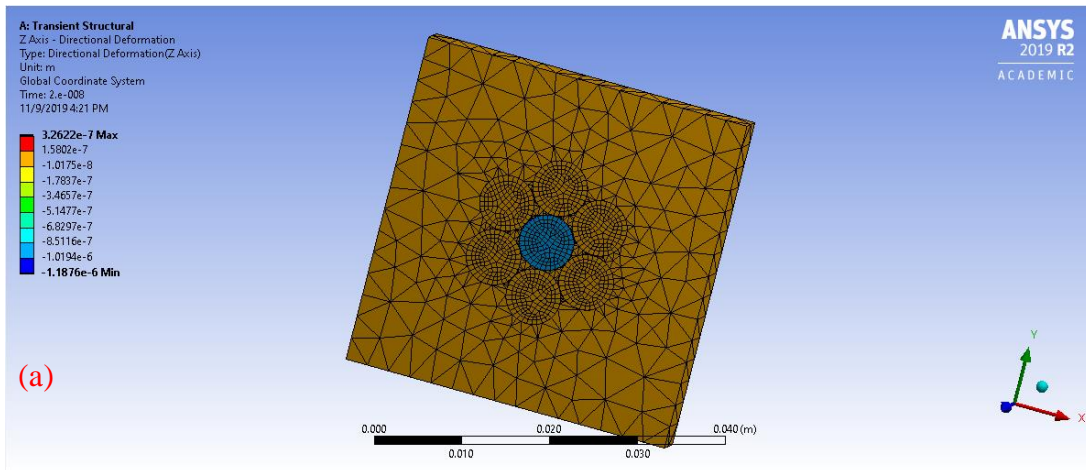
○ 4.3.1. Step 1 Results: Force Applied at the Center

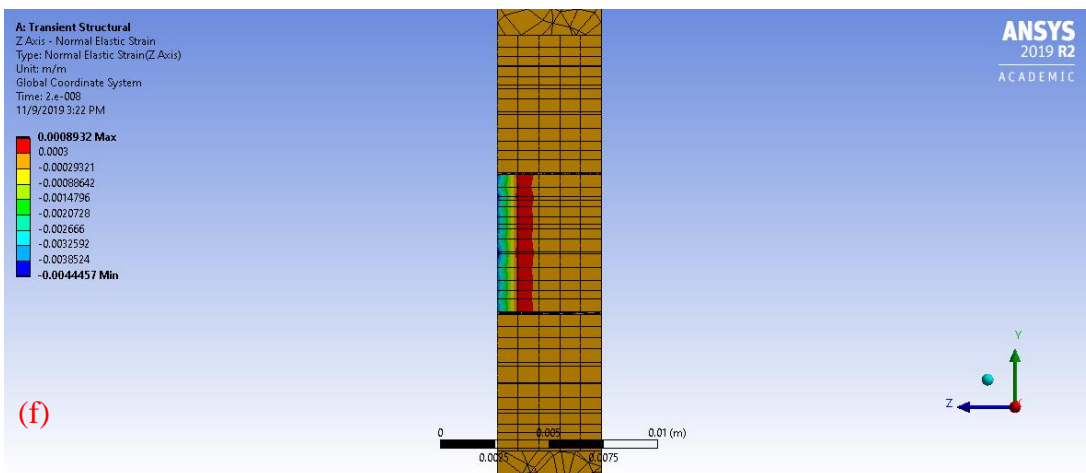
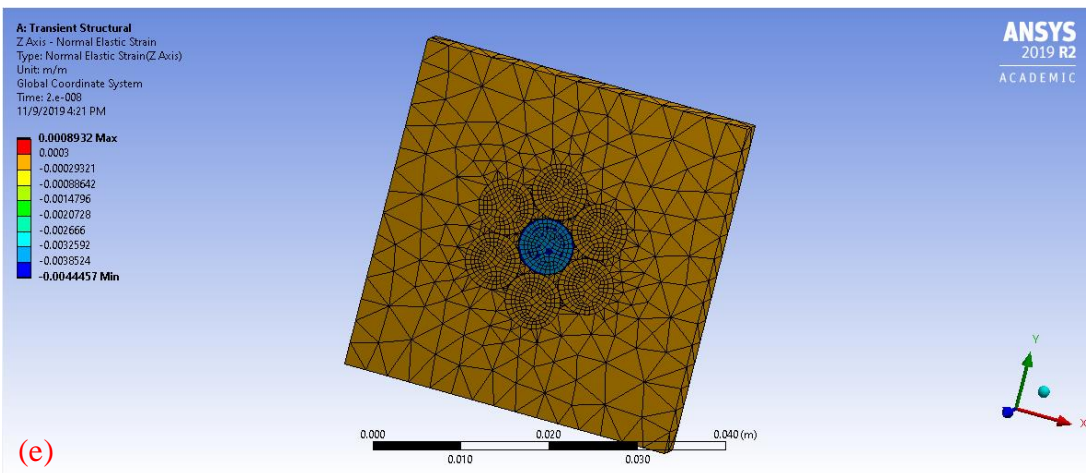
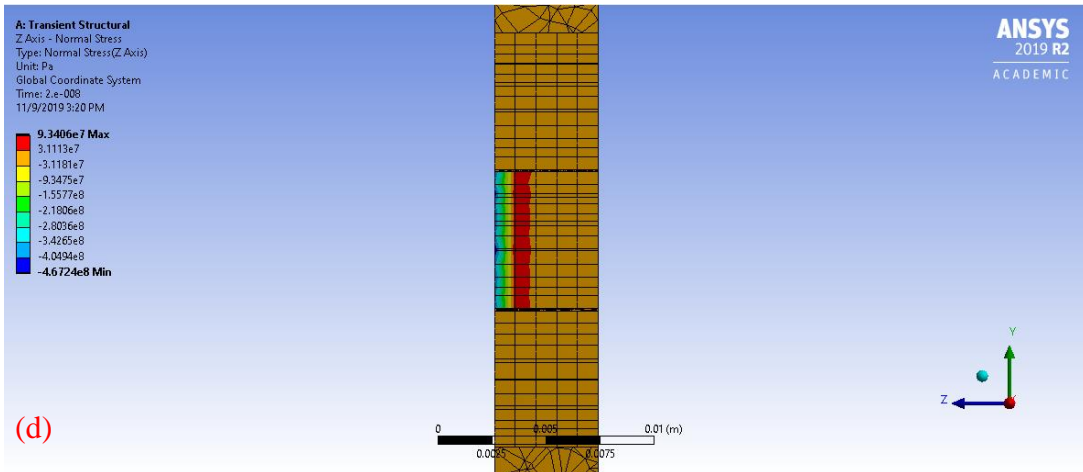
Loading Condition

The FEM results of Z direction displacement, Z direction stress and strain, and von-Mises stress for Step 1 loading condition are shown in Table 16 and Figure 39 a), b), c), d), e), f), g), and h).

Table 16. FEM results of step 1 in the loading condition.

Step 1 Loading Condition		
	Tensile	Compressive
Z Displacement	0.32622 μm	-1.1876 μm
Z Stress	93.406 MPa	-467.24 MPa
Z Strain	$8.9320 \times 10^{-4} \frac{m}{m}$	$-4.4457 \times 10^{-3} \frac{m}{m}$
von-Mises Stress	237.68 MPa	





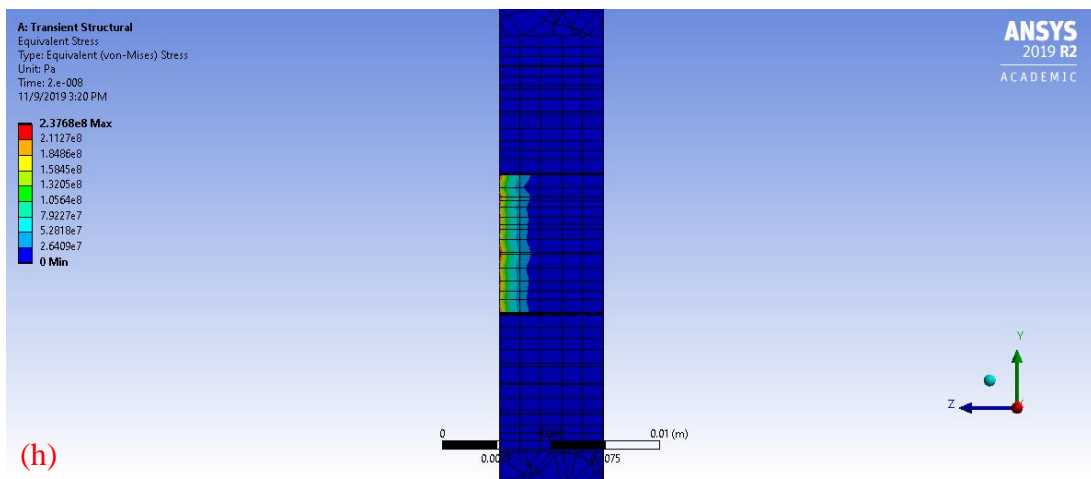
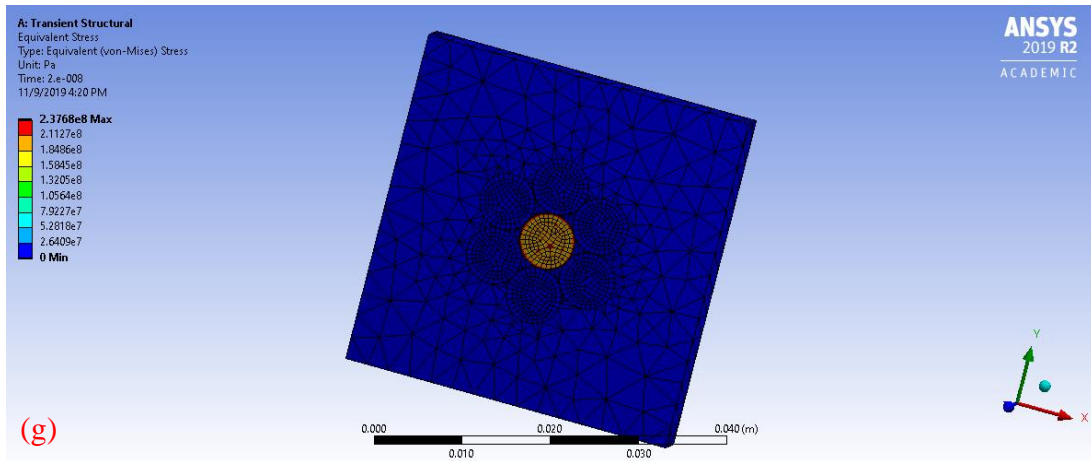


Figure 39. FEM results for Step 1 loading condition. (a) Z direction displacement, (b) Z direction displacement section view, (c) Z stress, (d) Z stress section view, (e) Z strain, (f) Z strain section view, (g) von-Mises stress, and (h) von-Mises stress section view.

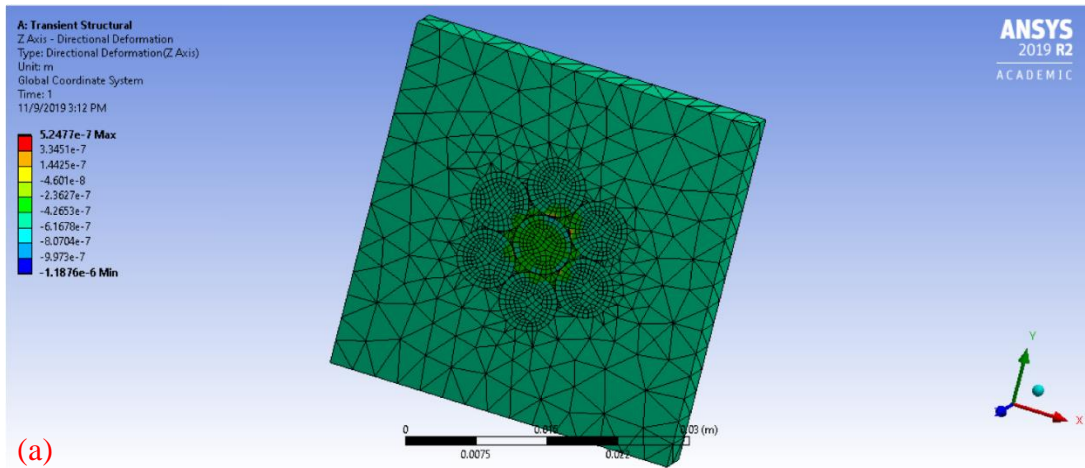
Unloading Condition

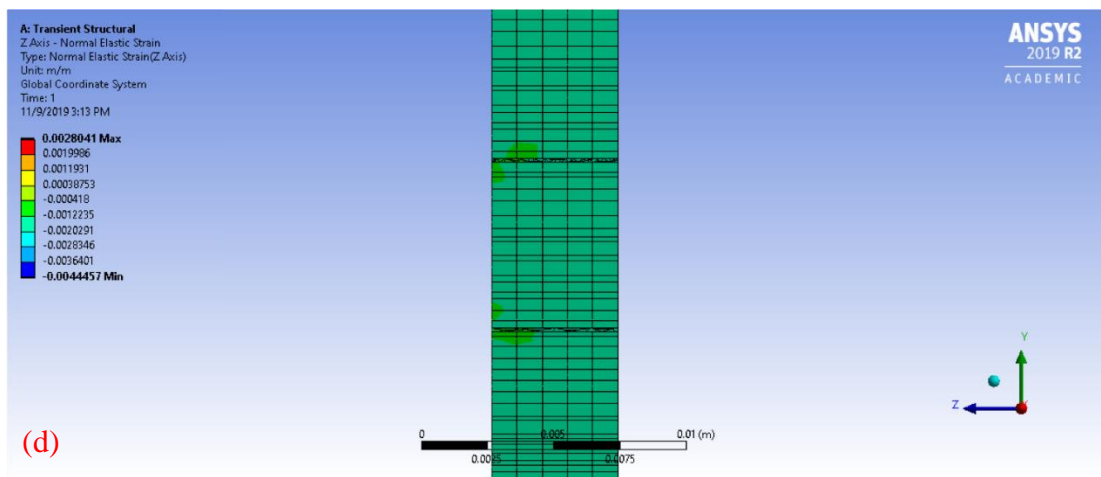
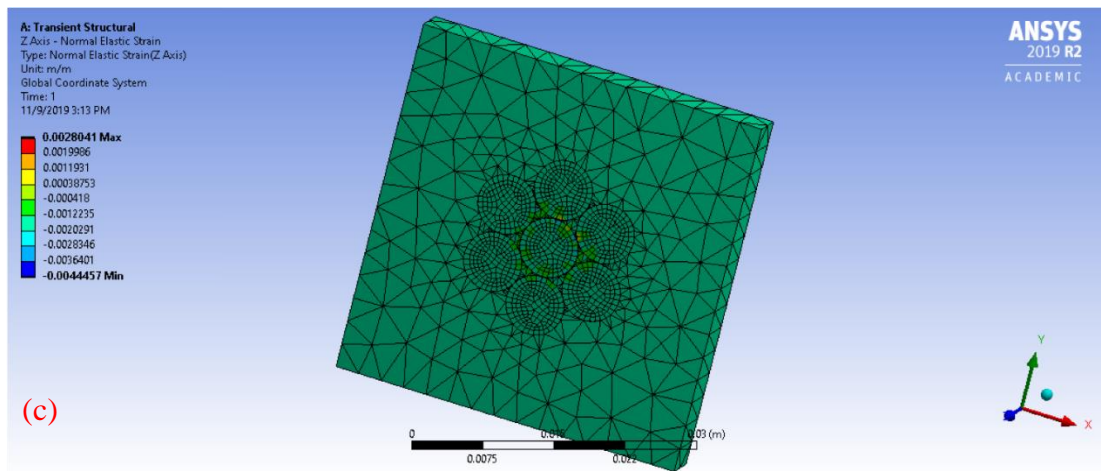
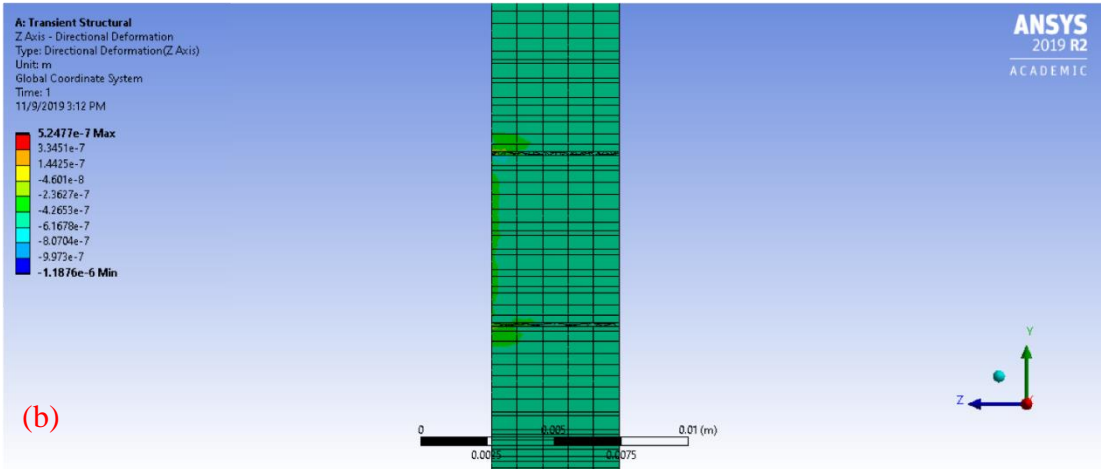
The FEM results of Z direction displacement, Z direction strain, von-Mises stress, and residual stress for Step 1 unloading condition are shown in Table 17 and Figure 40 a), b), c), d), e), and f).

Table 17. FEM results of Step 1 in the unloading condition.

Step 1 Unloading Condition		
	Tensile	Compressive
Z Displacement	$2.1673 \times 10^{-5} \mu m$	$-1.6457 \times 10^{-5} \mu m$
Z Strain	$5.7103 \times 10^{-8} \frac{m}{m}$	$-4.4058 \times 10^{-8} \frac{m}{m}$
von-Mises Stress	0.019106 MPa	

Step 1		
Depth of Stress Beyond the Proportional Limit	N/A (von-Mises stress did not exceed the proportional limit)	
Depth of Residual Stress	0.354 mm	
Residual Stress	Tensile Stress	0.0046751 MPa (Max)
	Compressive Stress	-0.0041163 MPa (Min)





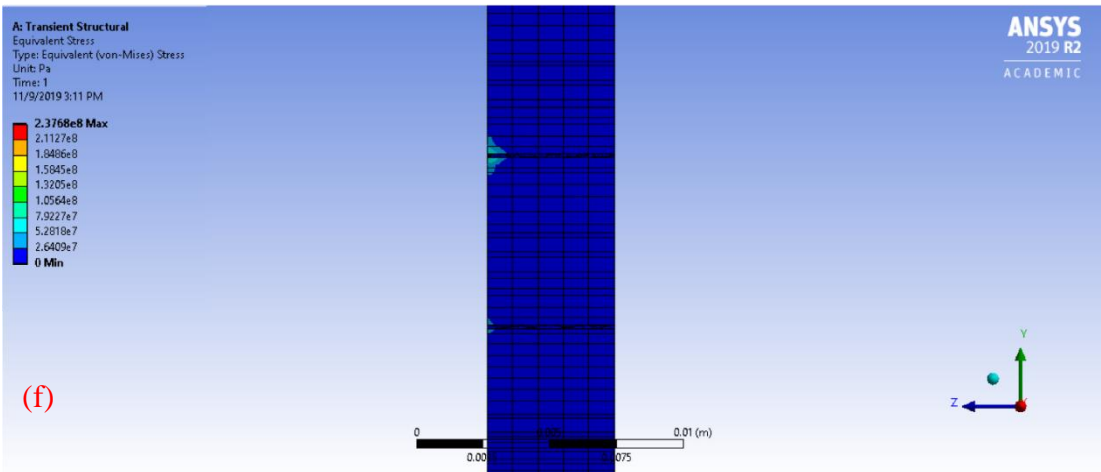
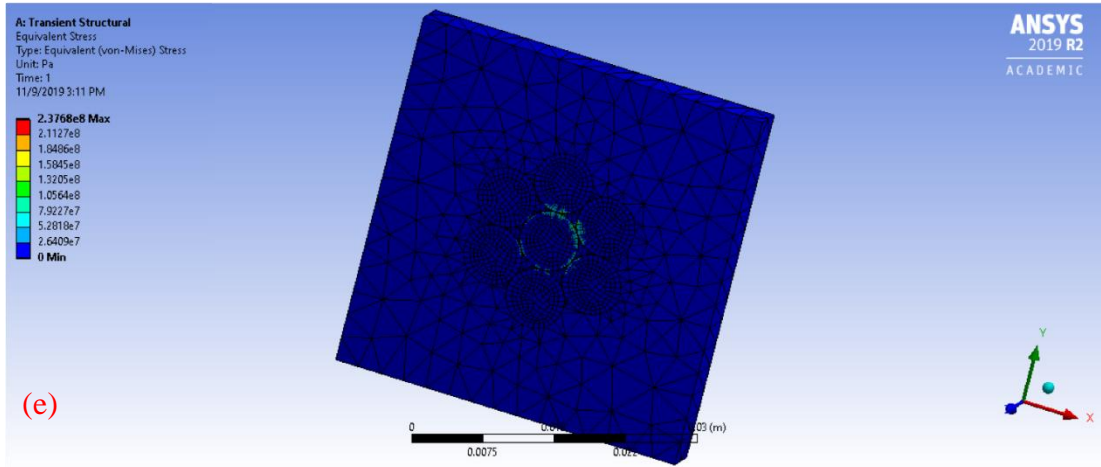


Figure 40. FEM results for Step 1 unloading condition. **(a)** Z direction displacement, **(b)** Z direction displacement section view, **(c)** Z strain, **(d)** Z strain section view, **(e)** von-Mises stress, and **(f)** von-Mises stress section view.

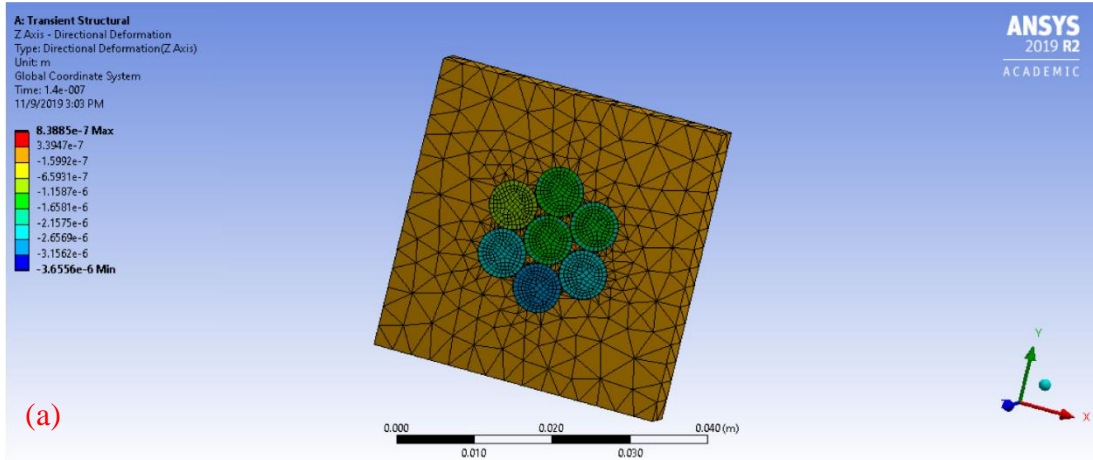
- 4.3.2. Step 2 Results: Force Applied at the Center then Surrounding

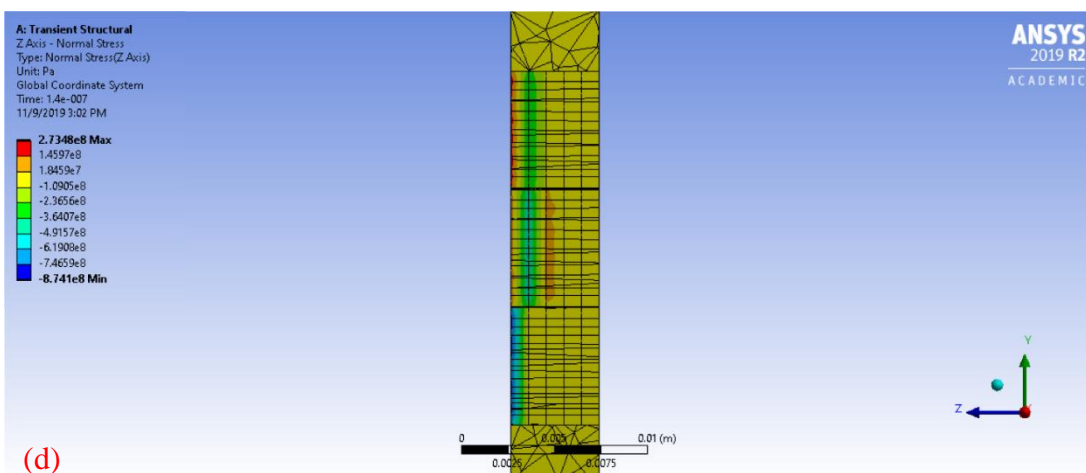
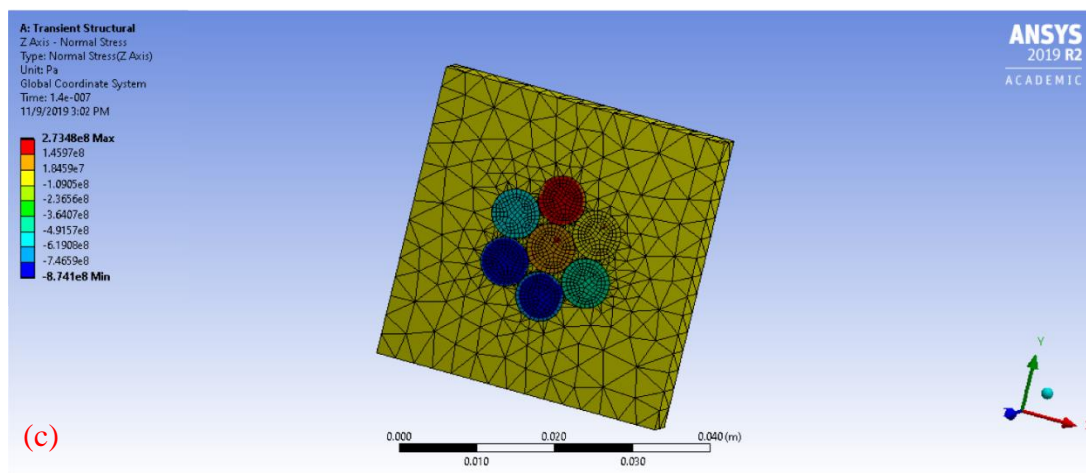
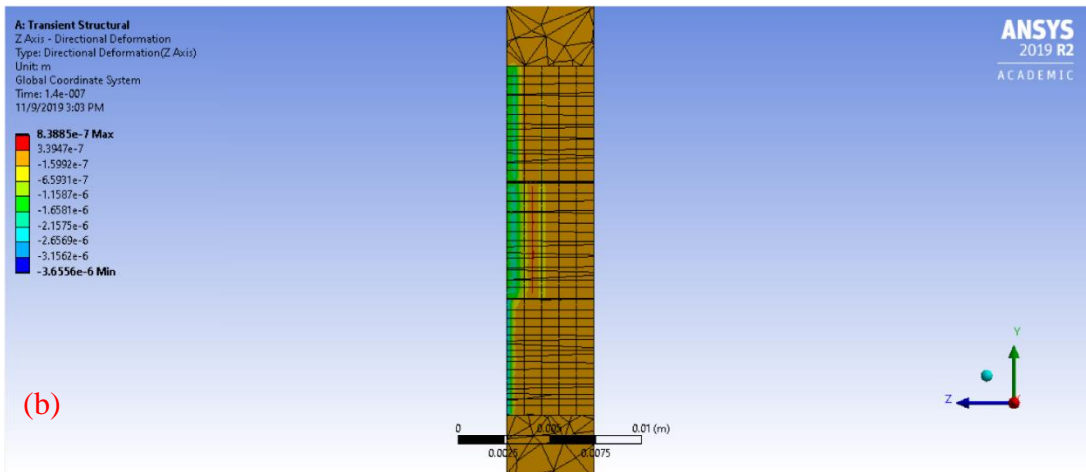
Loading Condition

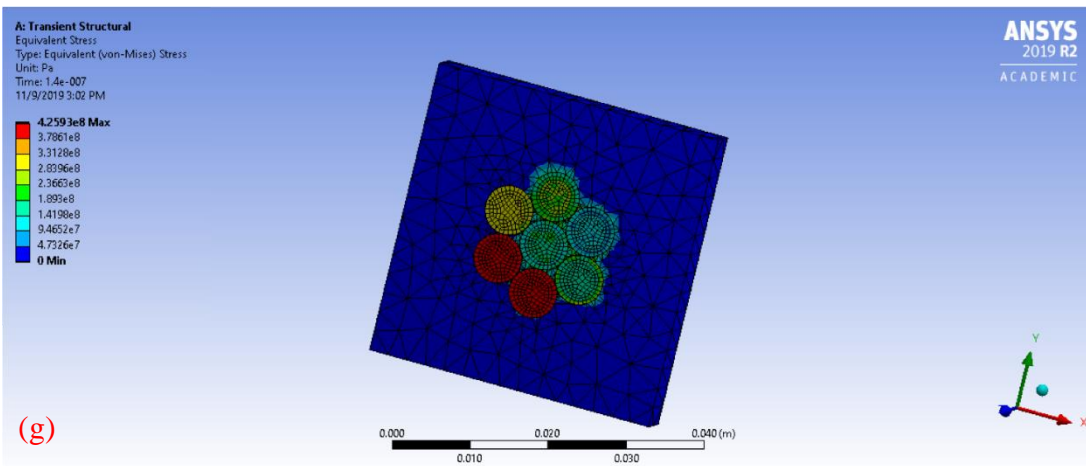
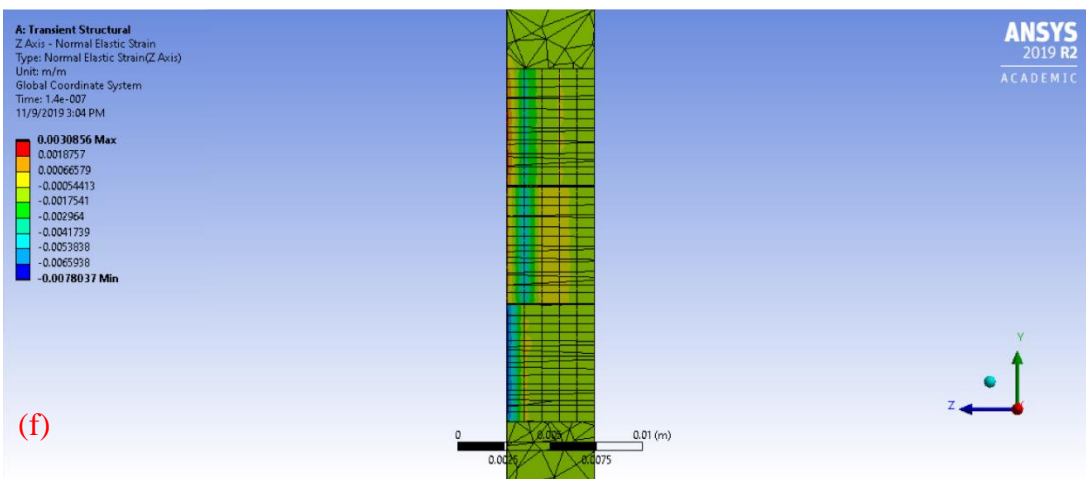
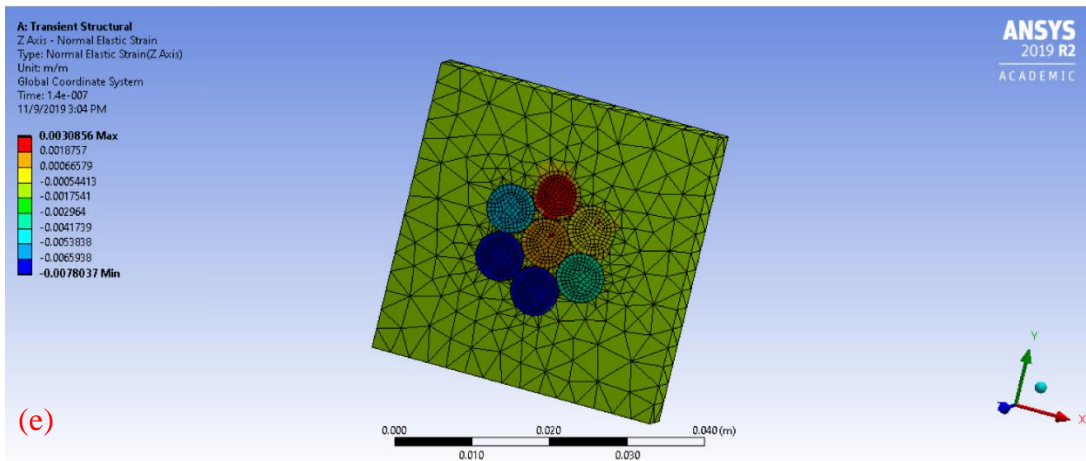
The FEM results of Z direction displacement, Z direction stress and strain, and von-Mises stress for Step 2 loading condition are shown in Table 18 and Figure 41 a), b), c), d), e), f), g), and h).

Table 18. FEM results of Step 2 in the loading condition.

Step 2 Loading Condition		
	Tensile	Compressive
Z Displacement	0.83885 μm	-3.6556 μm
Z Stress	273.48 MPa	-874.10 MPa
Z Strain	$3.0856 \times 10^{-3} \frac{m}{m}$	$-7.8037 \times 10^{-3} \frac{m}{m}$
von-Mises Stress	425.93 MPa	







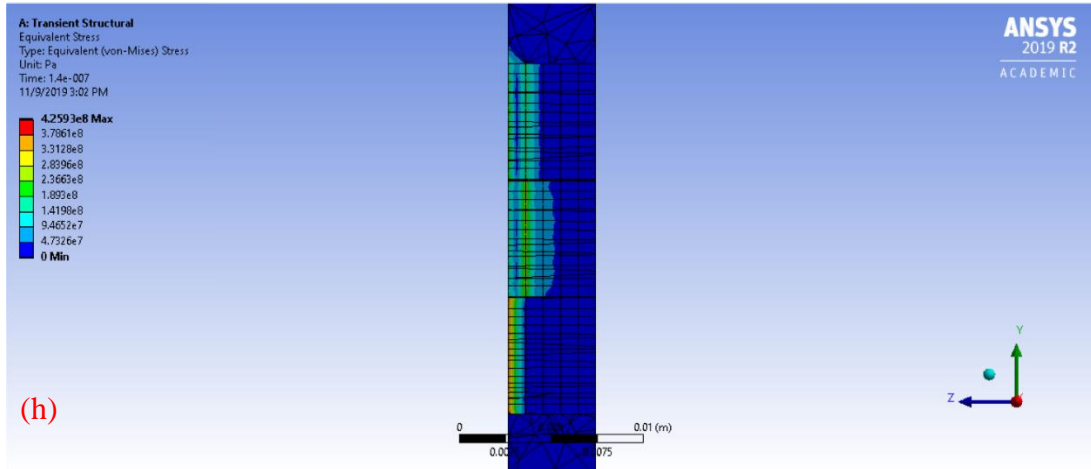


Figure 41. FEM results for Step 2 loading condition. (a) Z direction displacement, (b) Z direction displacement section view, (c) Z stress, (d) Z stress section view, (e) Z strain, (f) Z strain section view, (g) von-Mises stress, and (h) von-Mises stress section view.

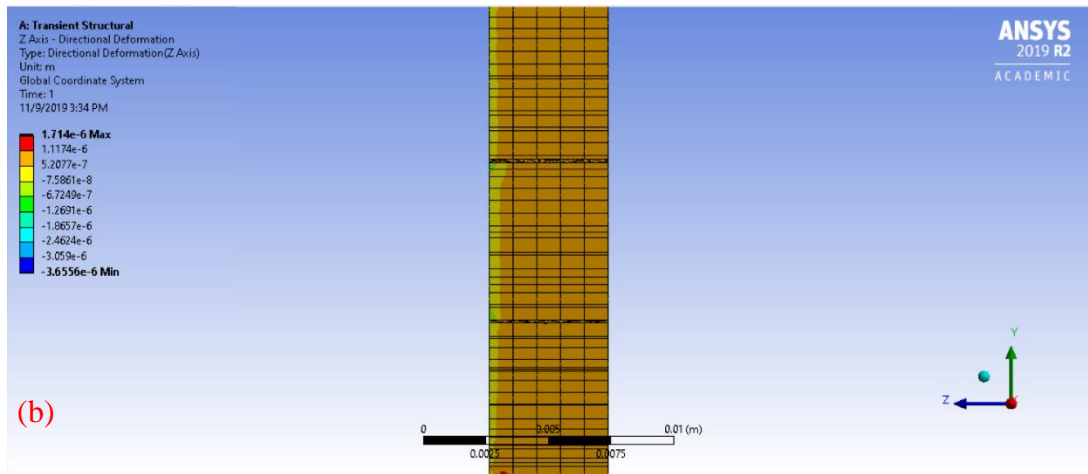
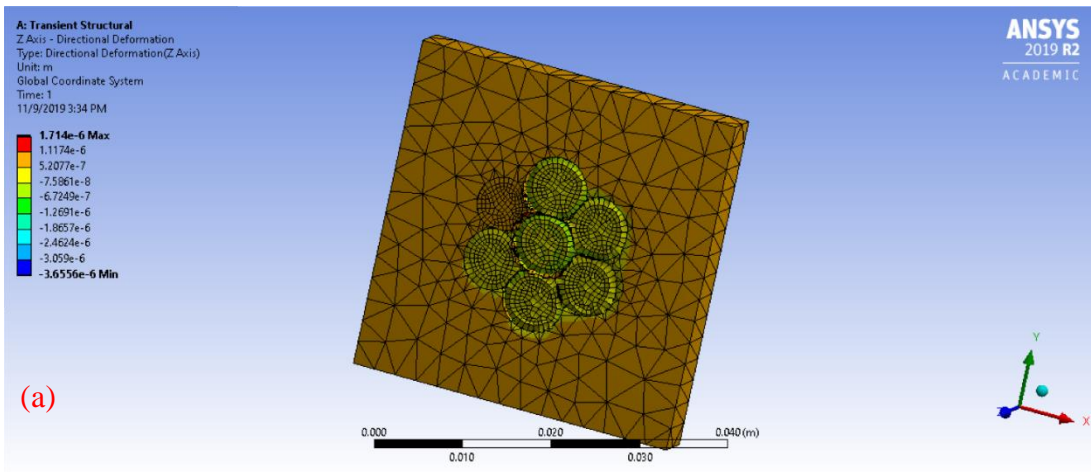
Unloading Condition

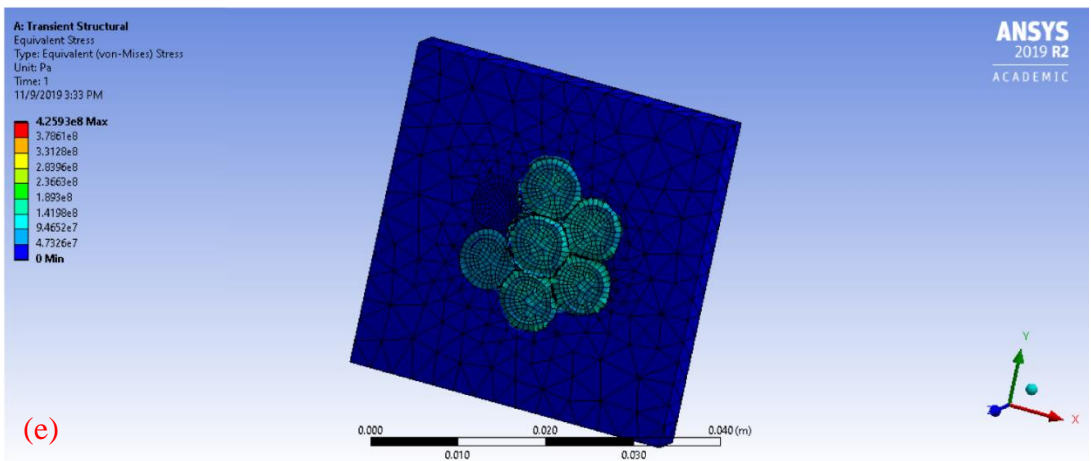
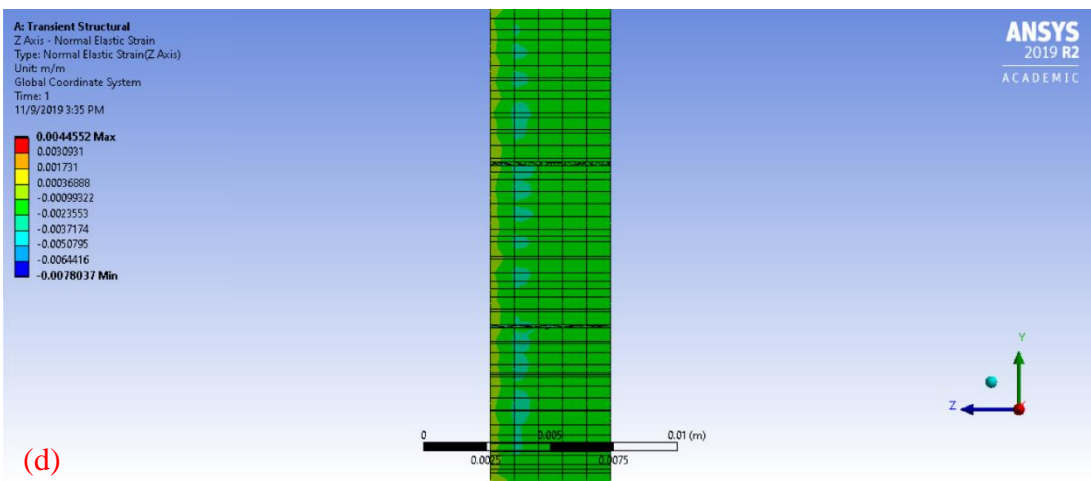
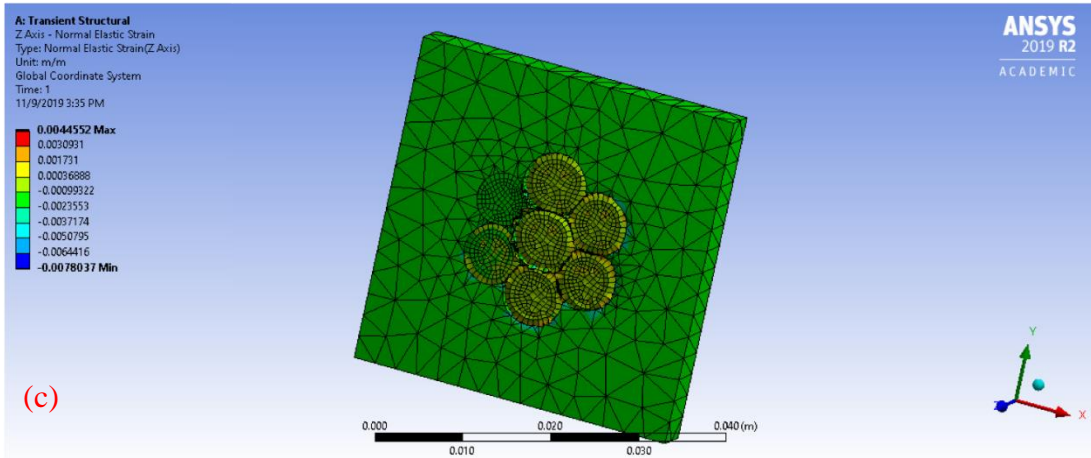
The FEM results of Z direction displacement, Z direction strain, von-Mises stress, and residual stress for Step 2 unloading condition are shown in Table 19 and Figure 42 a), b), c), d), e), and f).

Table 19. FEM results of Step 2 in the unloading condition.

Step 2 Unloading Condition		
	Tensile	Compressive
Z Displacement	$0.38634 \mu\text{m}$	$-1.5645 \mu\text{m}$
Z Strain	$1.1902 \times 10^{-3} \frac{\text{m}}{\text{m}}$	$-9.7193 \times 10^{-4} \frac{\text{m}}{\text{m}}$
von-Mises Stress	173.96 MPa	

Step 2		
Depth of Stress Beyond the Proportional Limit	1.417 mm	
Depth of Residual Stress	0.628 mm	
Residual Stress	Tensile Stress	94.108 MPa (Max)
	Compressive Stress	-77.998 MPa (Min)





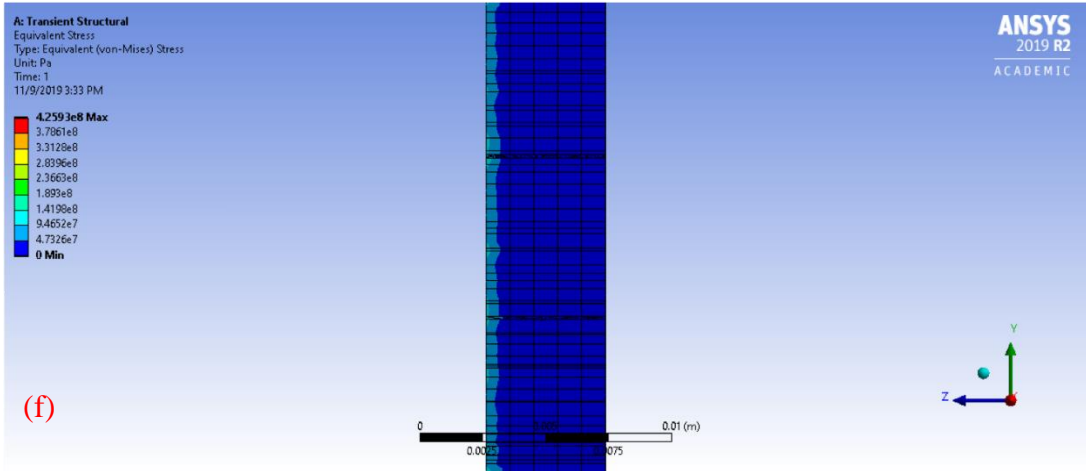


Figure 42. FEM results for Step 2 unloading condition. (a) Z direction displacement, (b) Z direction displacement section view, (c) Z strain, (d) Z strain section view, (e) von-Mises stress, and (f) von-Mises stress section view.

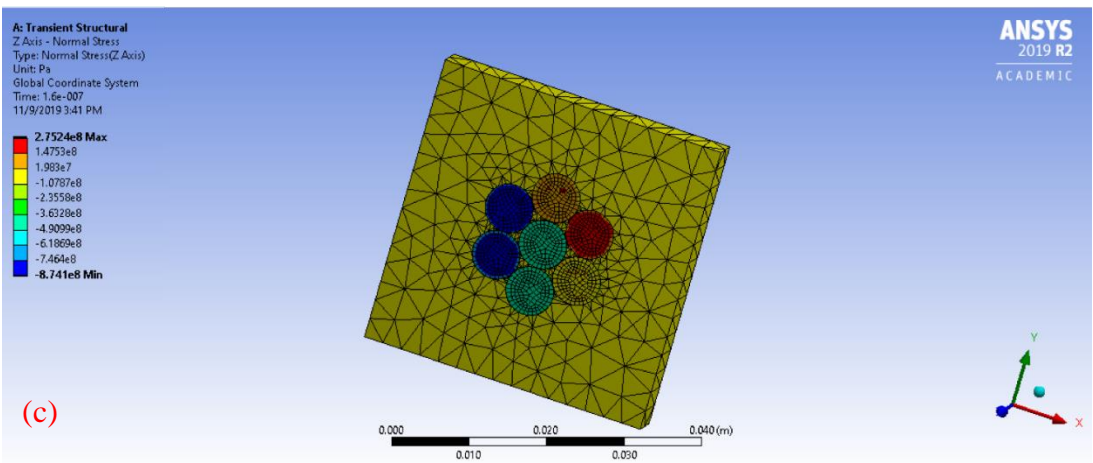
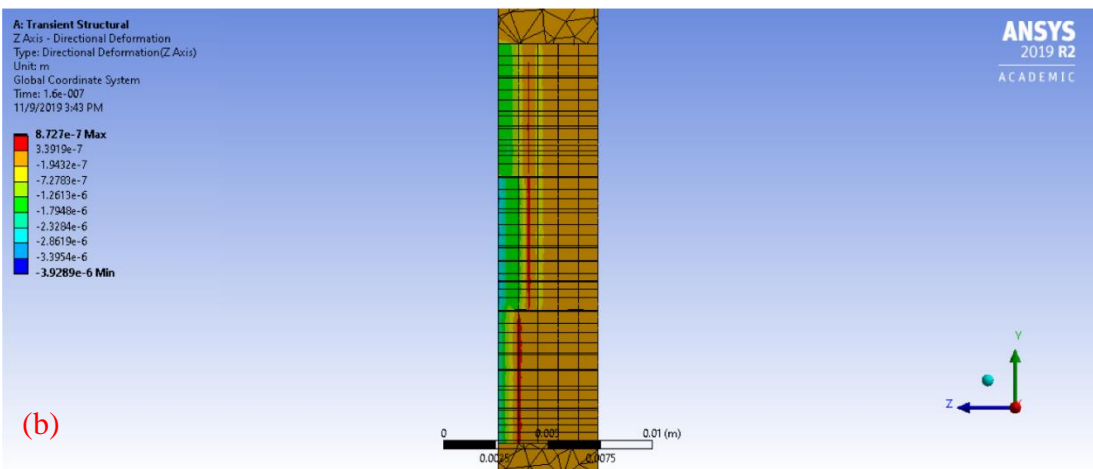
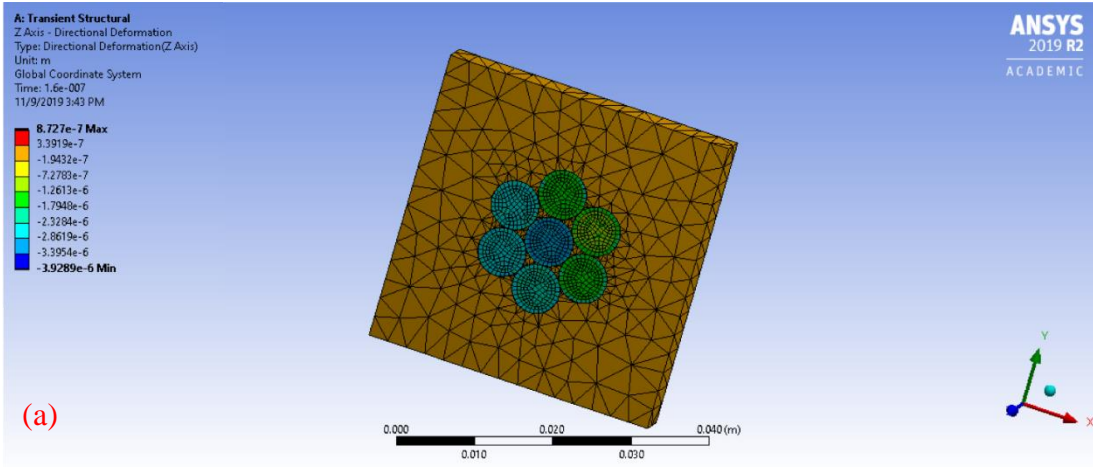
- 4.3.3. Step 3 Results: Force Applied at the Center, then Surrounding, and Back to Center

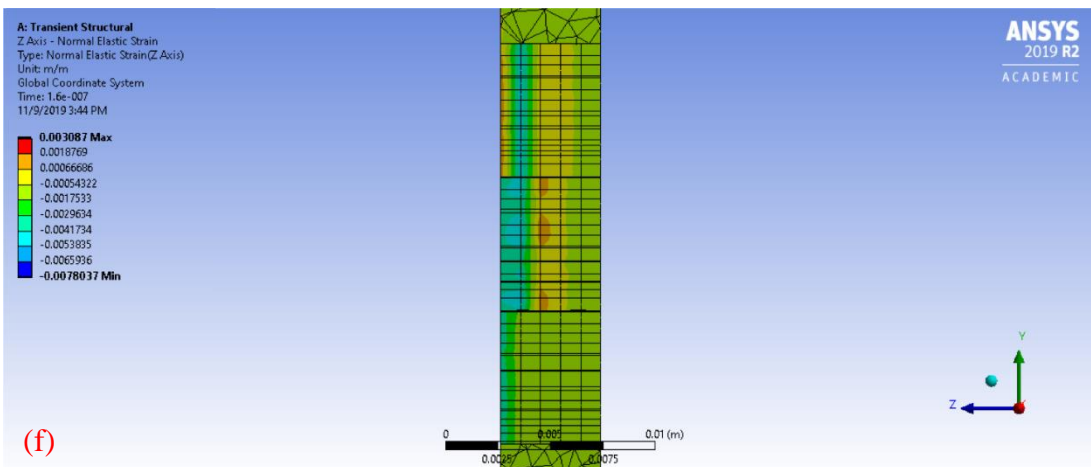
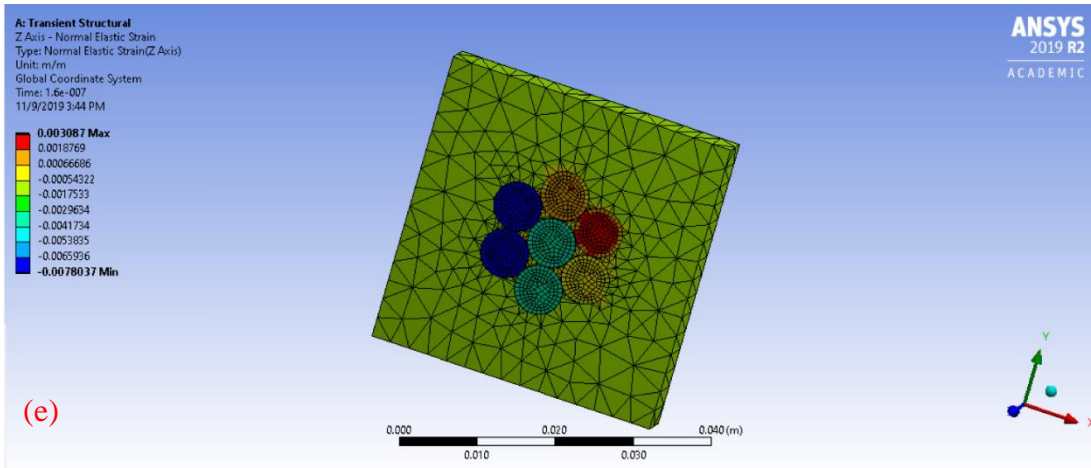
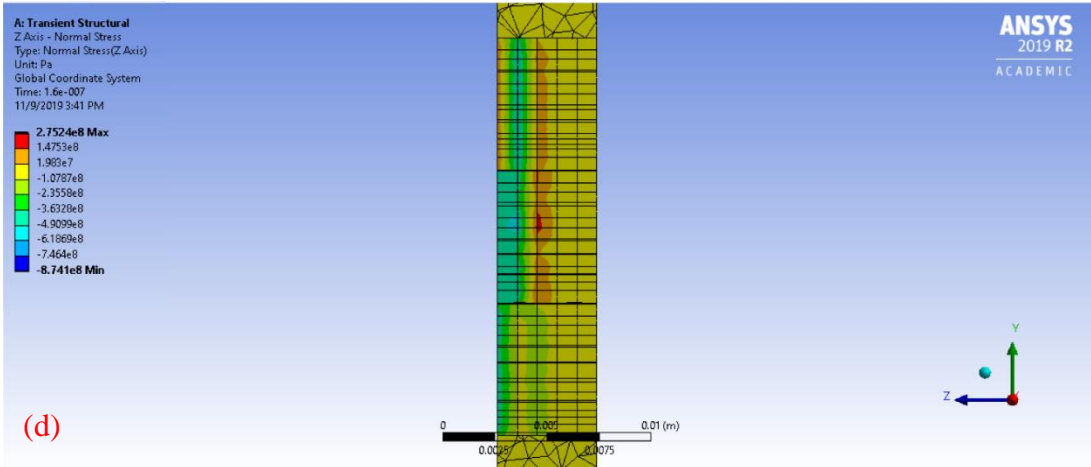
Loading Condition

The FEM results of Z direction displacement, Z direction stress and strain, and von-Mises stress for Step 3 loading condition are shown in Table 20 and Figure 43 a), b), c), d), e), f), g), and h).

Table 20. FEM results of Step 3 in the loading condition.

Step 3 Loading Condition		
	Tensile	Compressive
Z Displacement	0.87270 μm	-3.9289 μm
Z Stress	275.24 MPa	-874.10 MPa
Z Strain	$3.0870 \times 10^{-3} \frac{\text{m}}{\text{m}}$	$-7.8037 \times 10^{-3} \frac{\text{m}}{\text{m}}$
von-Mises Stress	436.62 MPa	





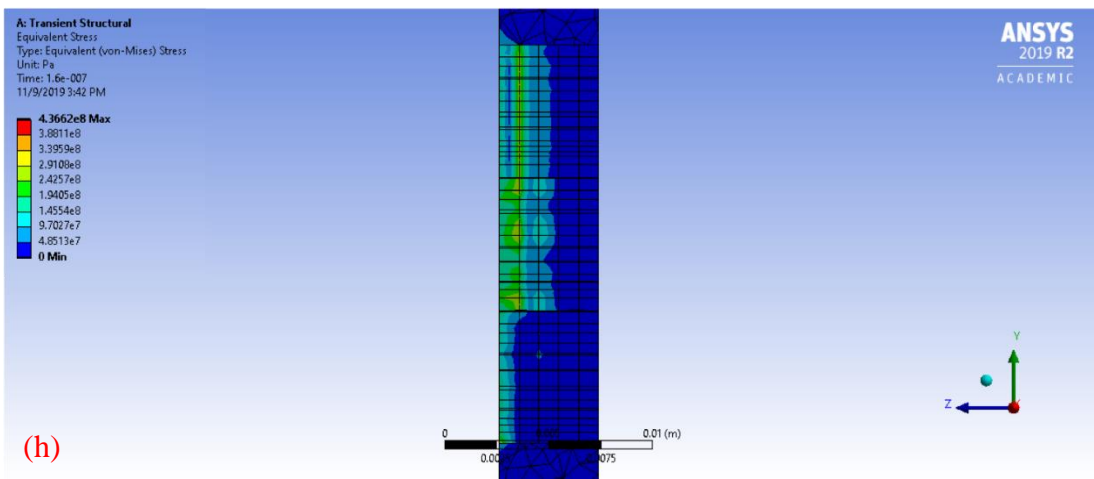
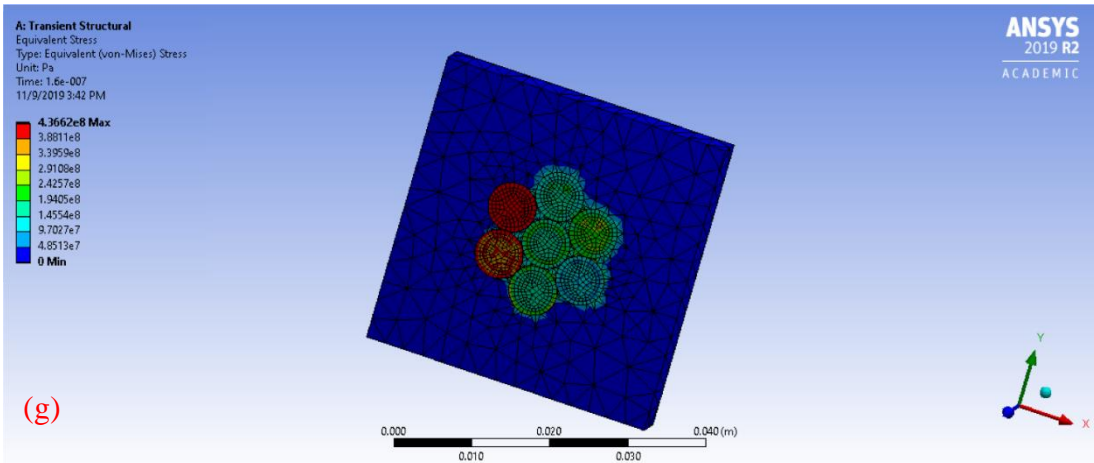


Figure 43. FEM results for Step 3 loading condition. (a) Z direction displacement, (b) Z direction displacement section view, (c) Z stress, (d) Z stress section view, (e) Z strain, (f) Z strain section view, (g) von-Mises stress, and (h) von-Mises stress section view.

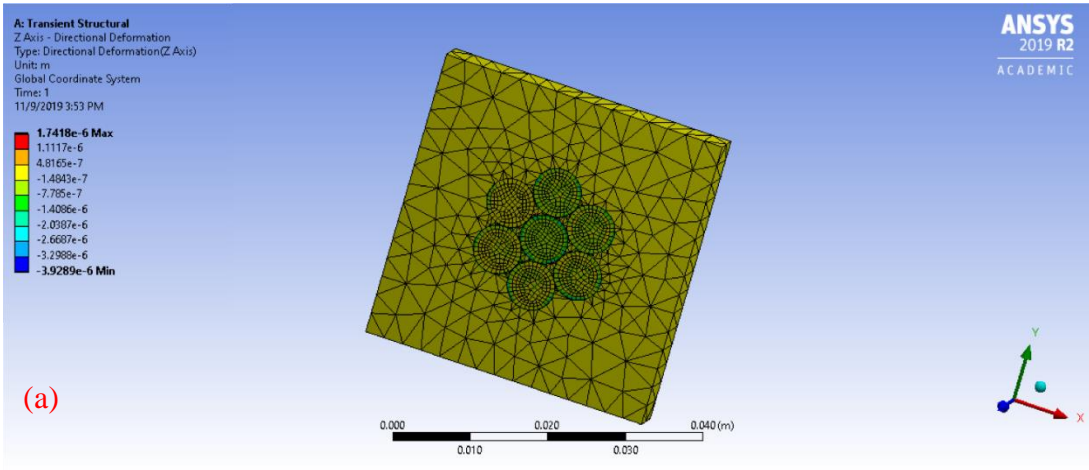
Unloading Condition

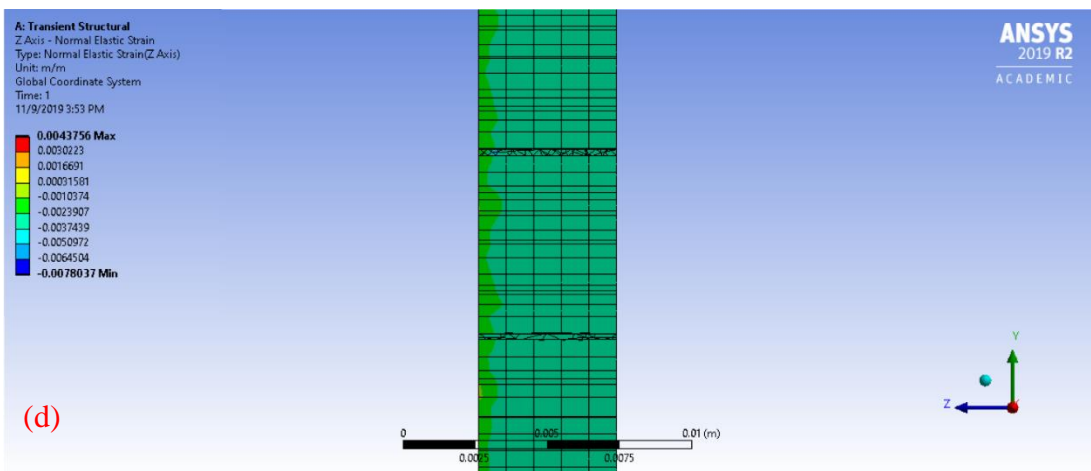
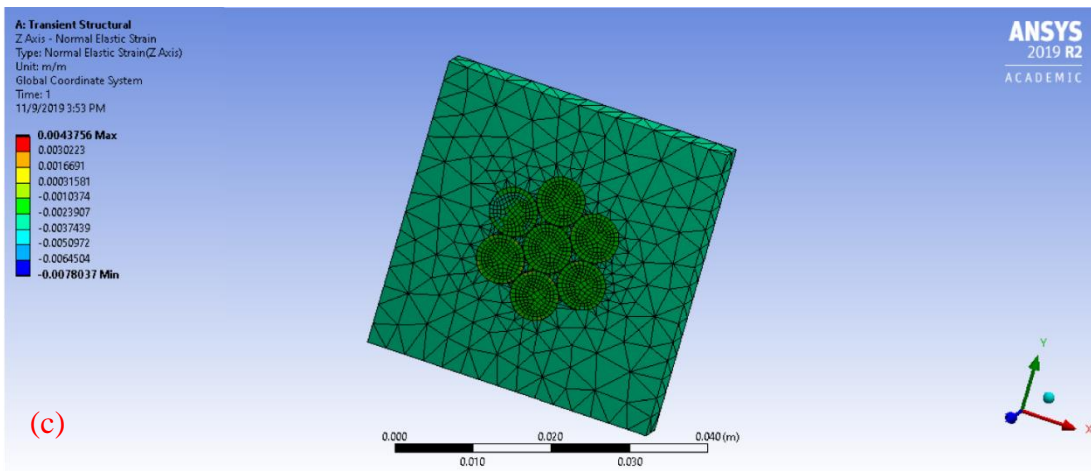
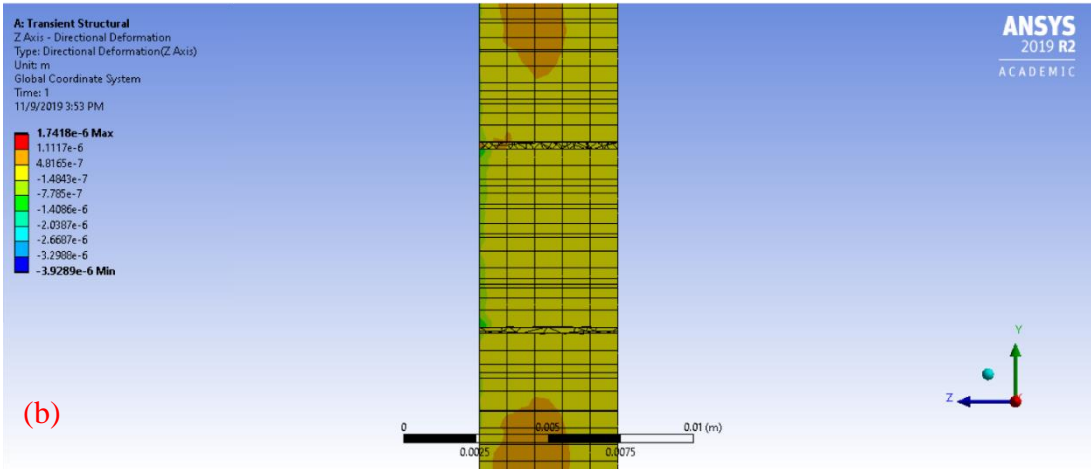
The FEM results of Z direction displacement, Z direction strain, von-Mises stress, and residual stress for Step 3 unloading condition are shown in Table 21 and Figure 44 a), b), c), d), e), and f).

Table 21. FEM results of Step 3 in the unloading condition.

Step 3 Unloading Condition		
	Tensile	Compressive
Z Displacement	0.51369 μm	-1.5886 μm
Z Strain	$2.0613 \times 10^{-3} \frac{m}{m}$	$-1.2576 \times 10^{-3} \frac{m}{m}$
von-Mises Stress	217.23 MPa	

Step 3		
Depth of Stress Beyond the Proportional Limit	1.788 mm	
Depth of Residual Stress	0.653 mm	
Residual Stress	Tensile Stress	173.30 MPa (Max)
	Compressive Stress	-101.68 MPa (Min)





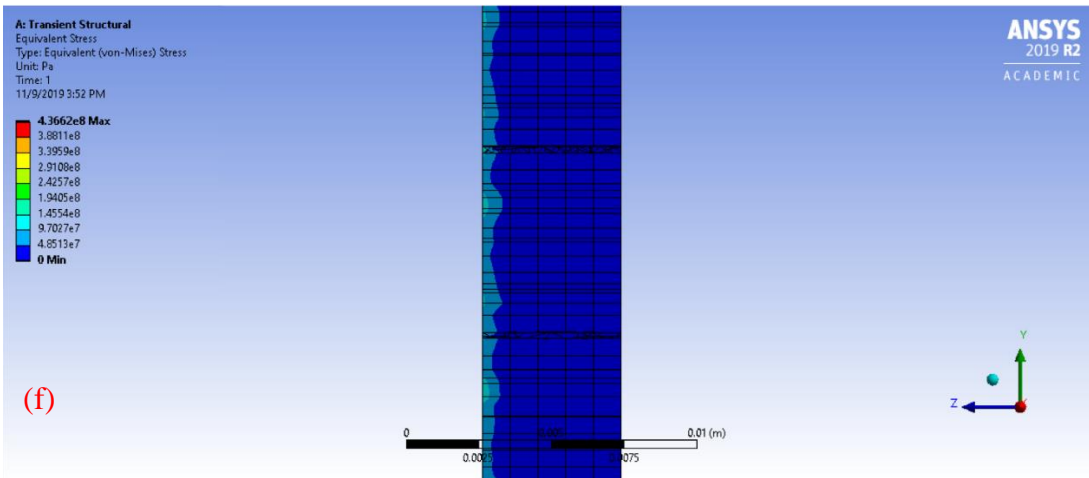
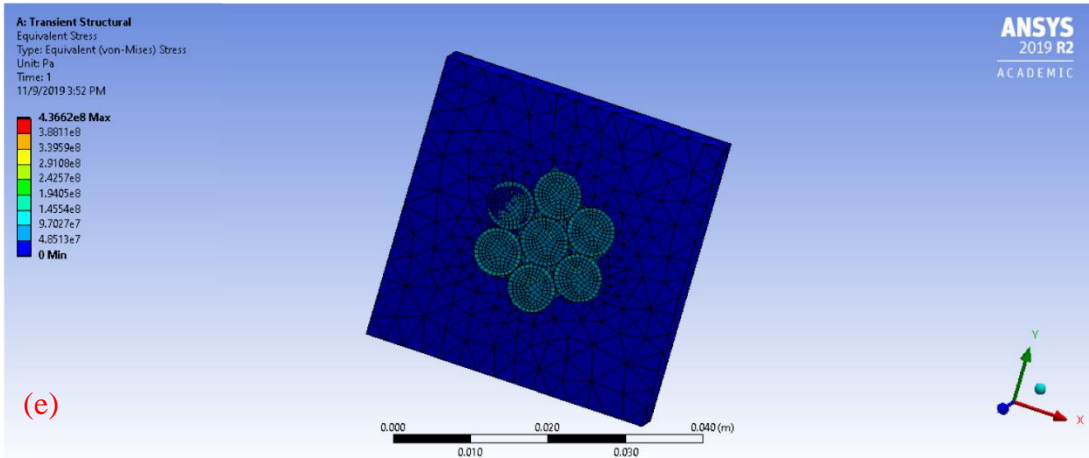


Figure 44. FEM results for Step 3 unloading condition. (a) Z direction displacement, (b) Z direction displacement section view, (c) Z strain, (d) Z strain section view, (e) von-Mises stress, and (f) von-Mises stress section view.

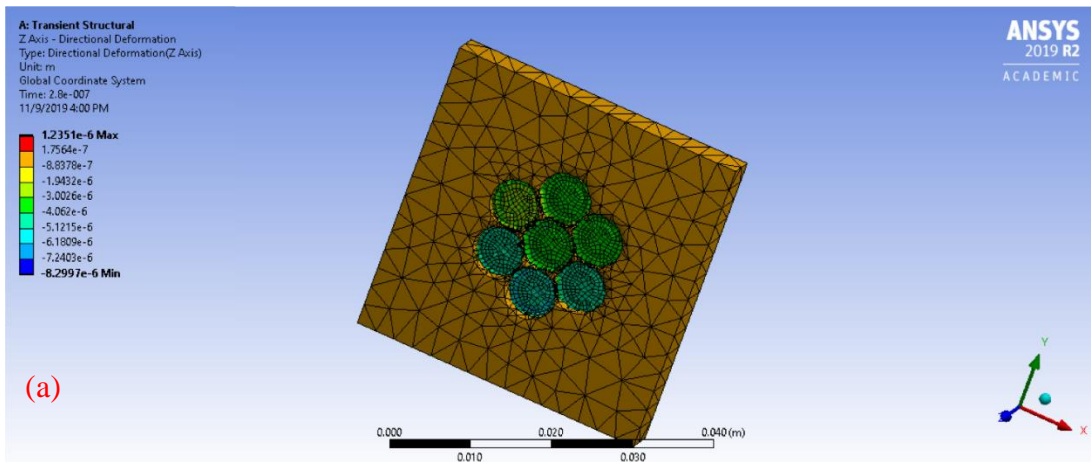
- 4.3.4. Step 4 Results: Force Applied at the Center, then Surrounding, Back to Center and Back to Surrounding

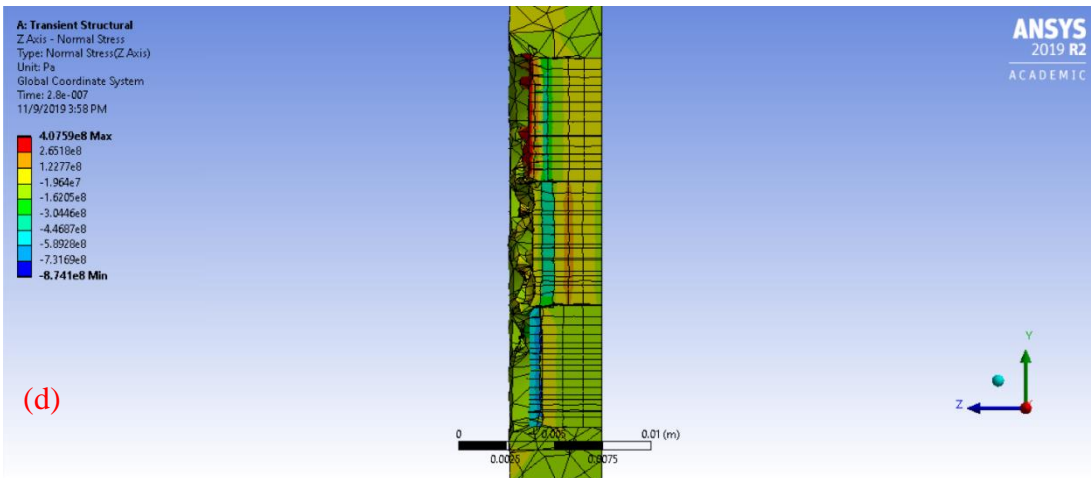
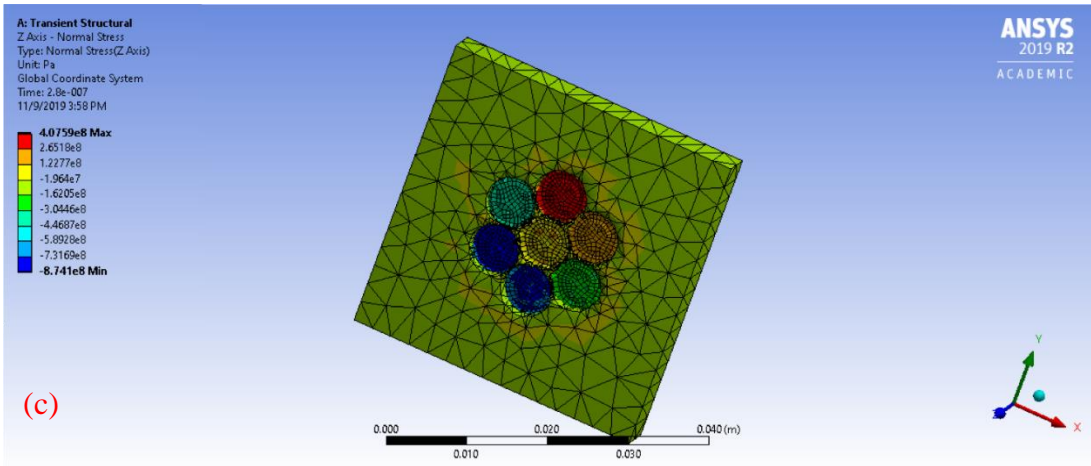
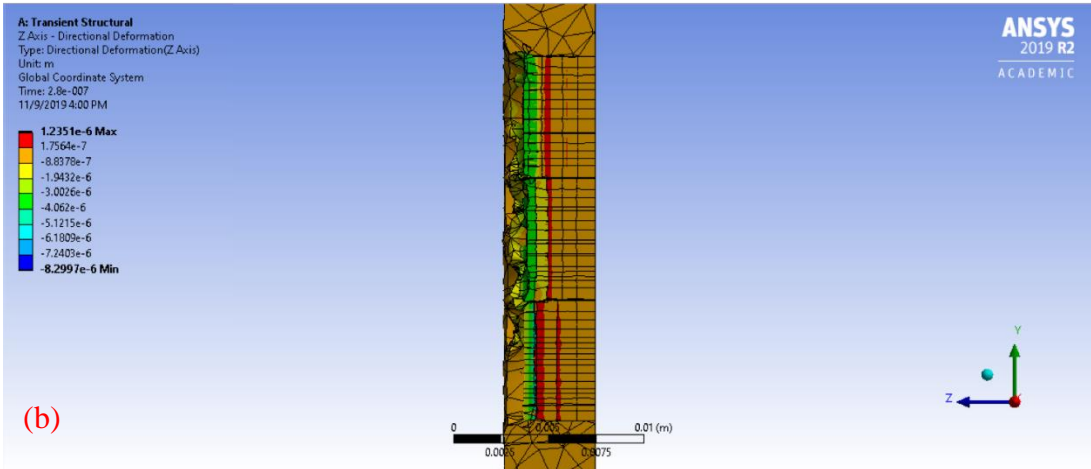
Loading Condition

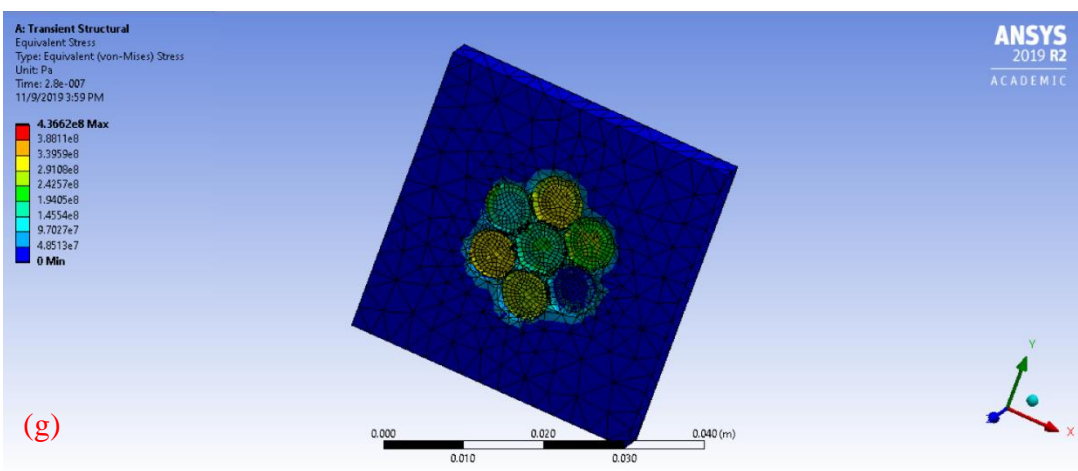
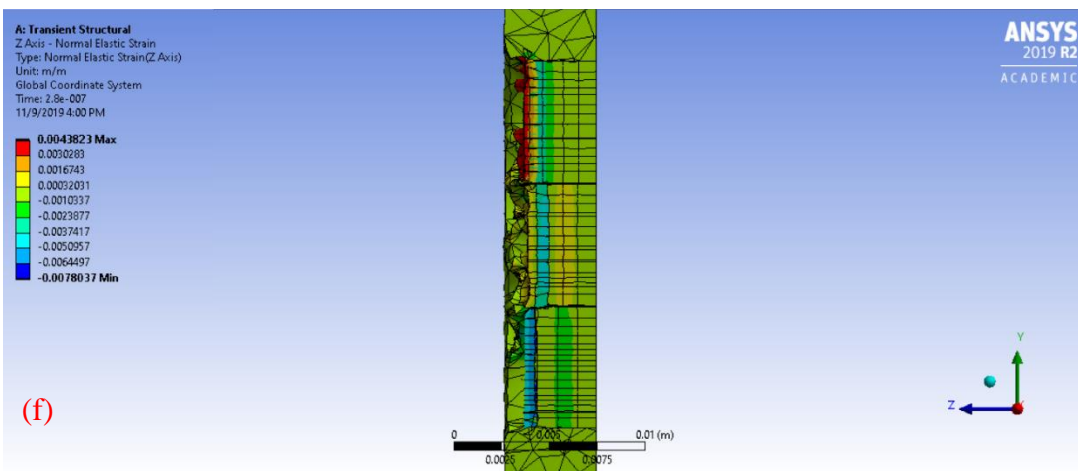
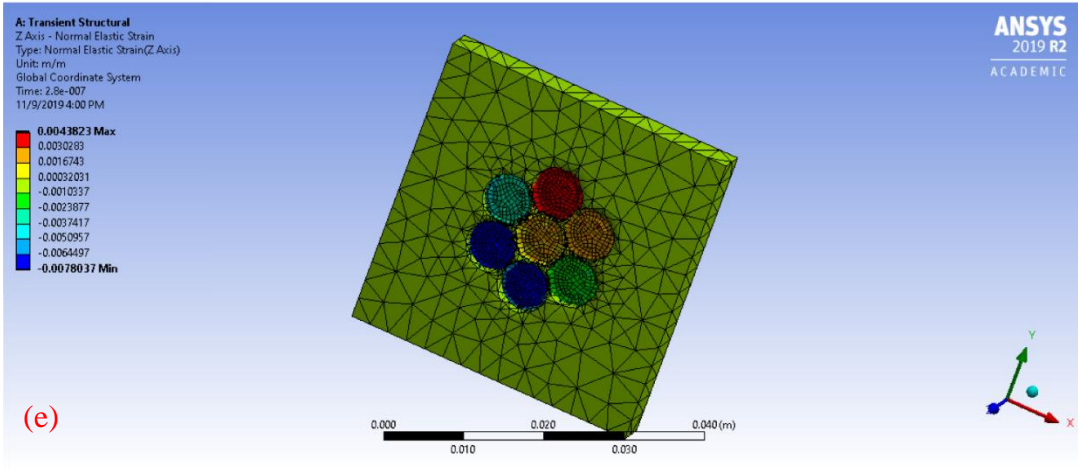
The FEM results of Z direction displacement, Z direction stress and strain, and von-Mises stress for Step 4 loading condition are shown in Table 22 and Figure 45 a), b), c), d), e), f), g), h), i), and j).

Table 22. FEM results of Step 4 in the loading condition.

Step 4 Loading Condition		
	Tensile	Compressive
Z Displacement	1.2351 μm	-8.2997 μm
Z Stress	407.59 MPa	-874.10 MPa
Z Strain	$4.3823 \times 10^{-3} \frac{\text{m}}{\text{m}}$	$-7.8037 \times 10^{-3} \frac{\text{m}}{\text{m}}$
Hydrostatic Stress	268.29 MPa	-660.44 MPa
von-Mises Stress	436.62 MPa	







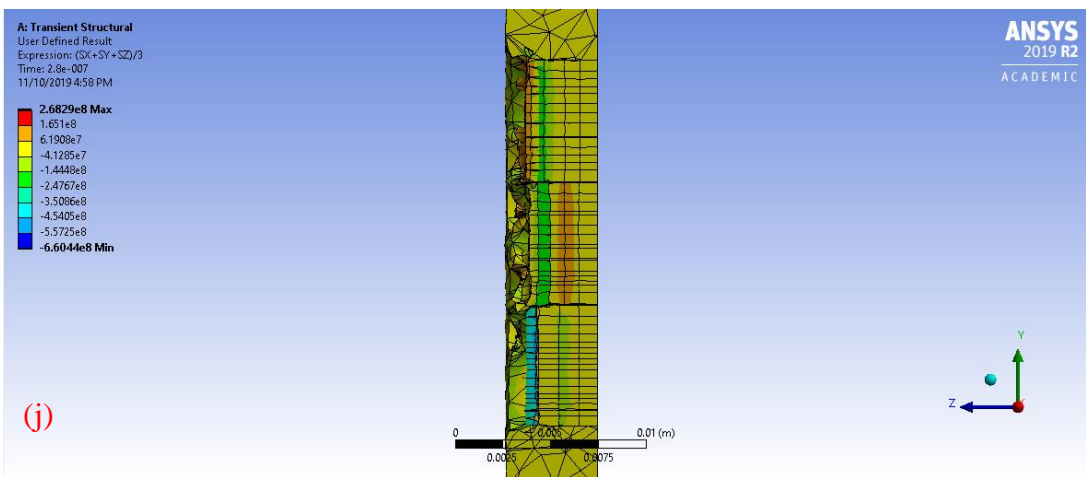
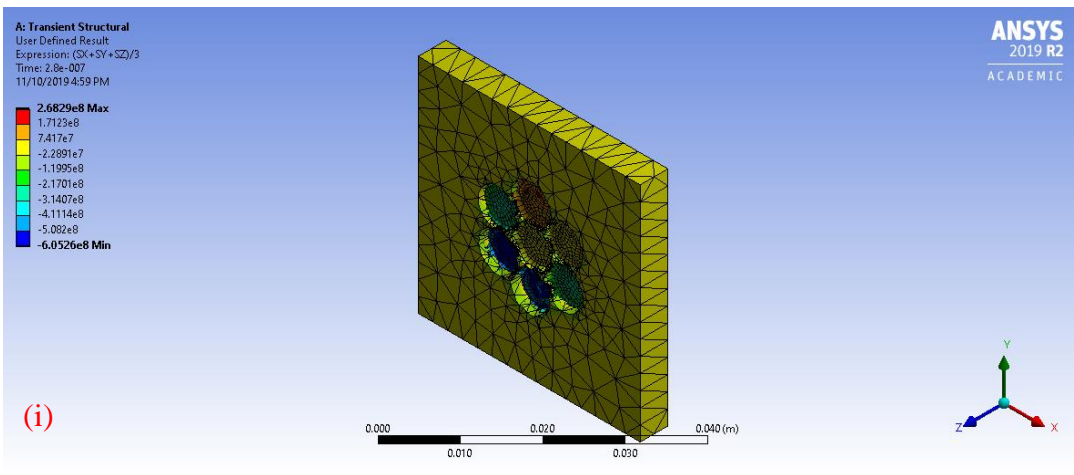
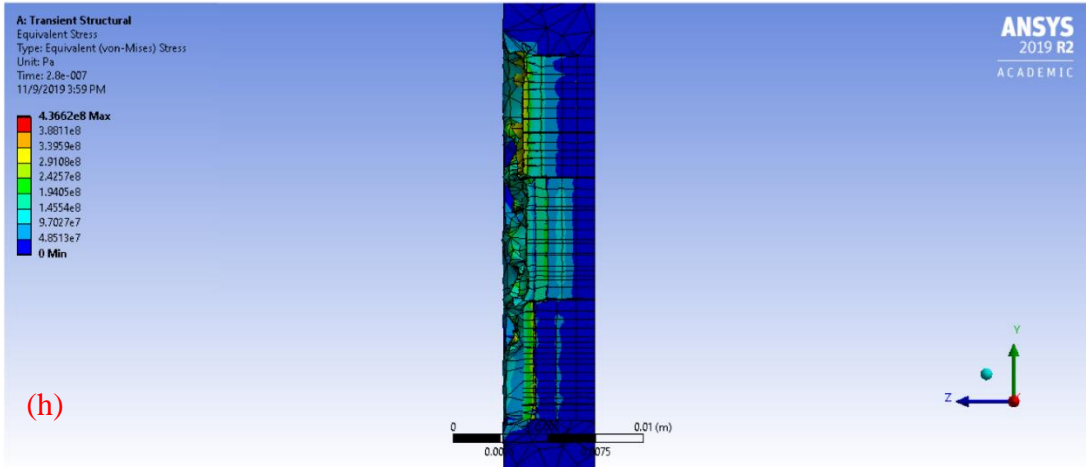


Figure 45. FEM results for Step 4 loading condition. (a) Z direction displacement, (b) Z direction displacement section view, (c) Z stress, (d) Z stress section view, (e) Z

strain, (f) Z strain section view, (g) von-Mises stress, (h) von-Mises stress section view, (i) Hydrostatic stress, and (j) Hydrostatic stress section view.

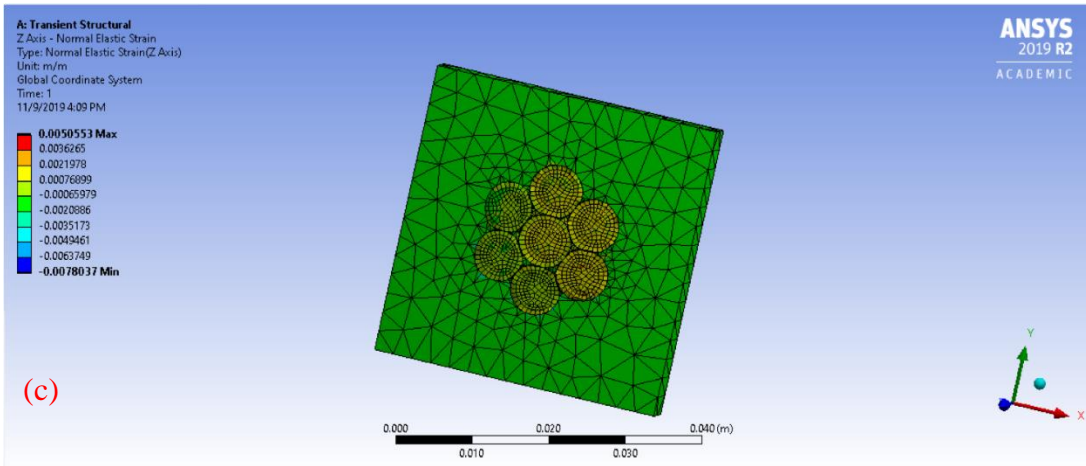
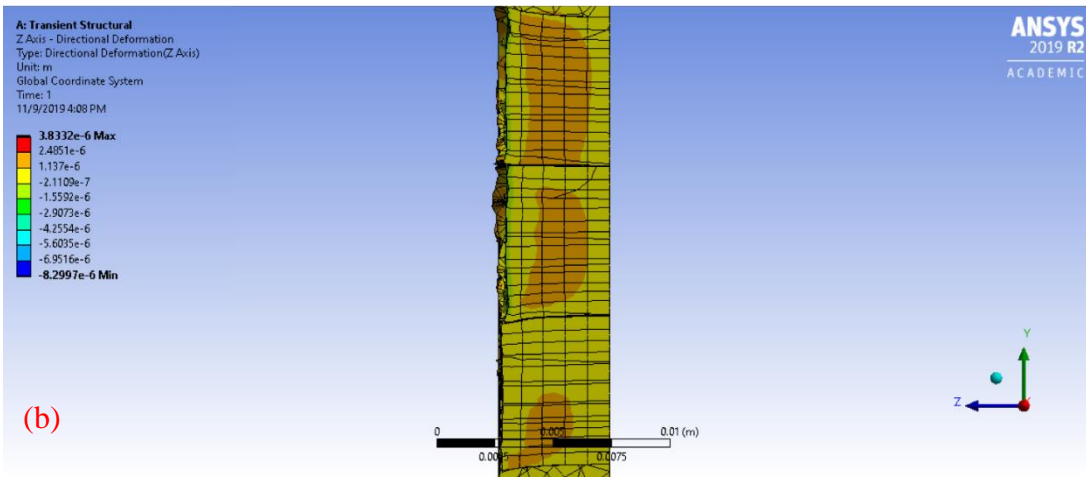
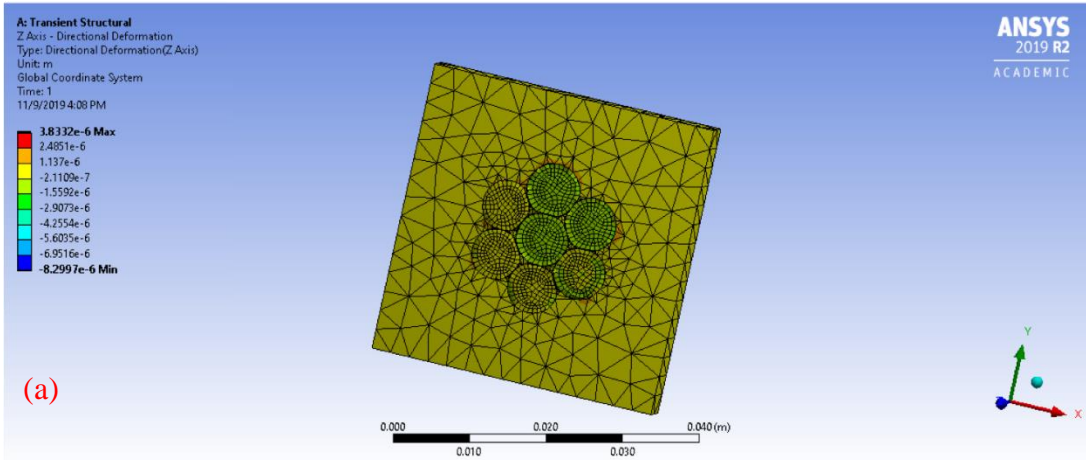
Unloading Condition

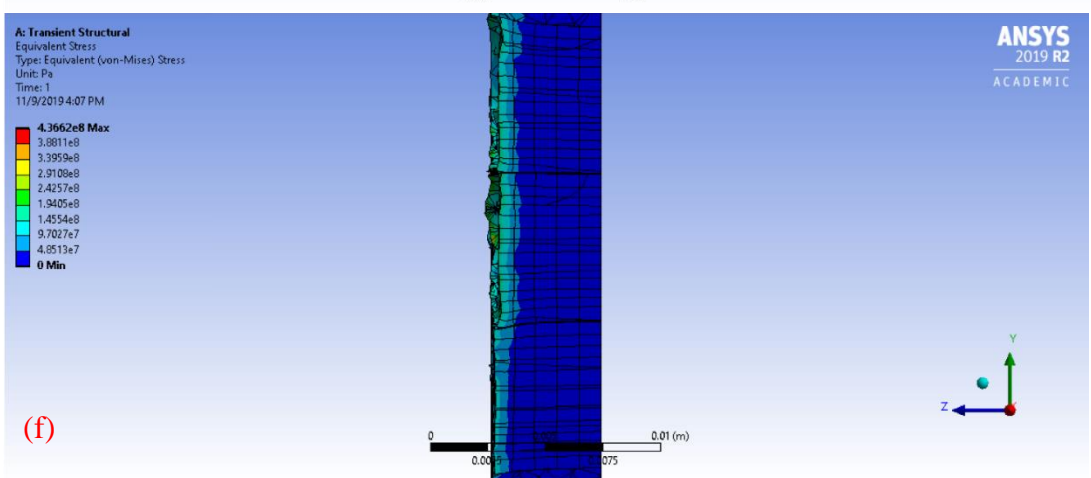
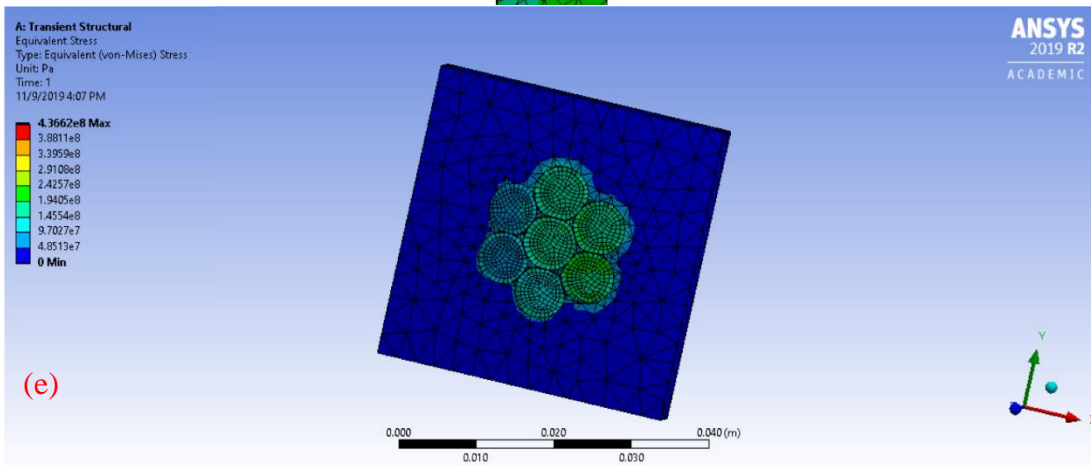
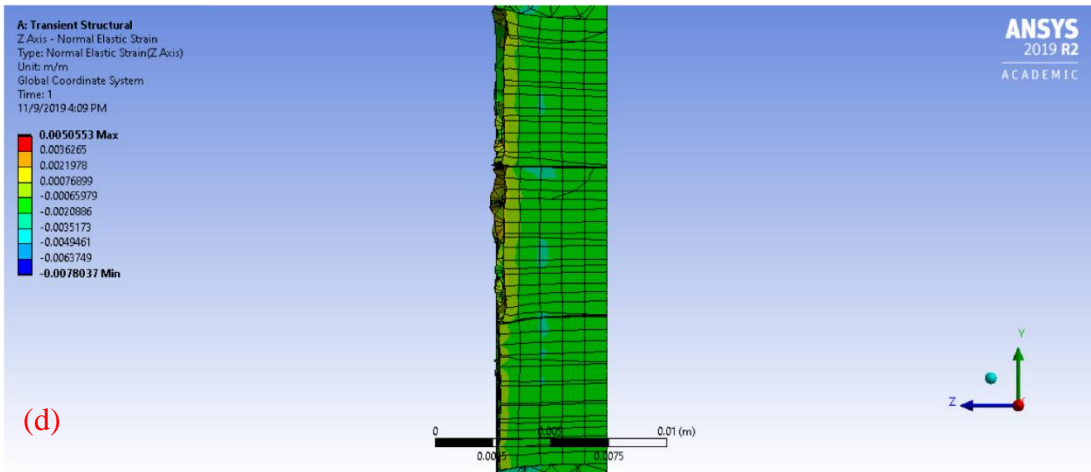
The FEM results of Z direction displacement, Z direction strain, von-Mises stress, residual stress, and hydrostatic stress for Step 4 unloading condition are shown in Table 23 and Figure 46 a), b), c), d), e), f), g), and h).

Table 23. FEM results of Step 4 in the unloading condition.

Step 4 Unloading Condition		
	Tensile	Compressive
Z Displacement	1.5692 μm	-5.1740 μm
Z Strain	$1.9183 \times 10^{-3} \frac{m}{m}$	$-1.6108 \times 10^{-3} \frac{m}{m}$
Hydrostatic Stress	86.598 MPa	-75.800 MPa
von-Mises Stress	224.56 MPa	

Step 4		
Depth of Stress Beyond the Proportional Limit	1.821 mm	
Depth of Residual Stress	1.656 mm	
Residual Stress	Tensile Stress	162.77 MPa (Max)
	Compressive Stress	-116.08 MPa (Min)





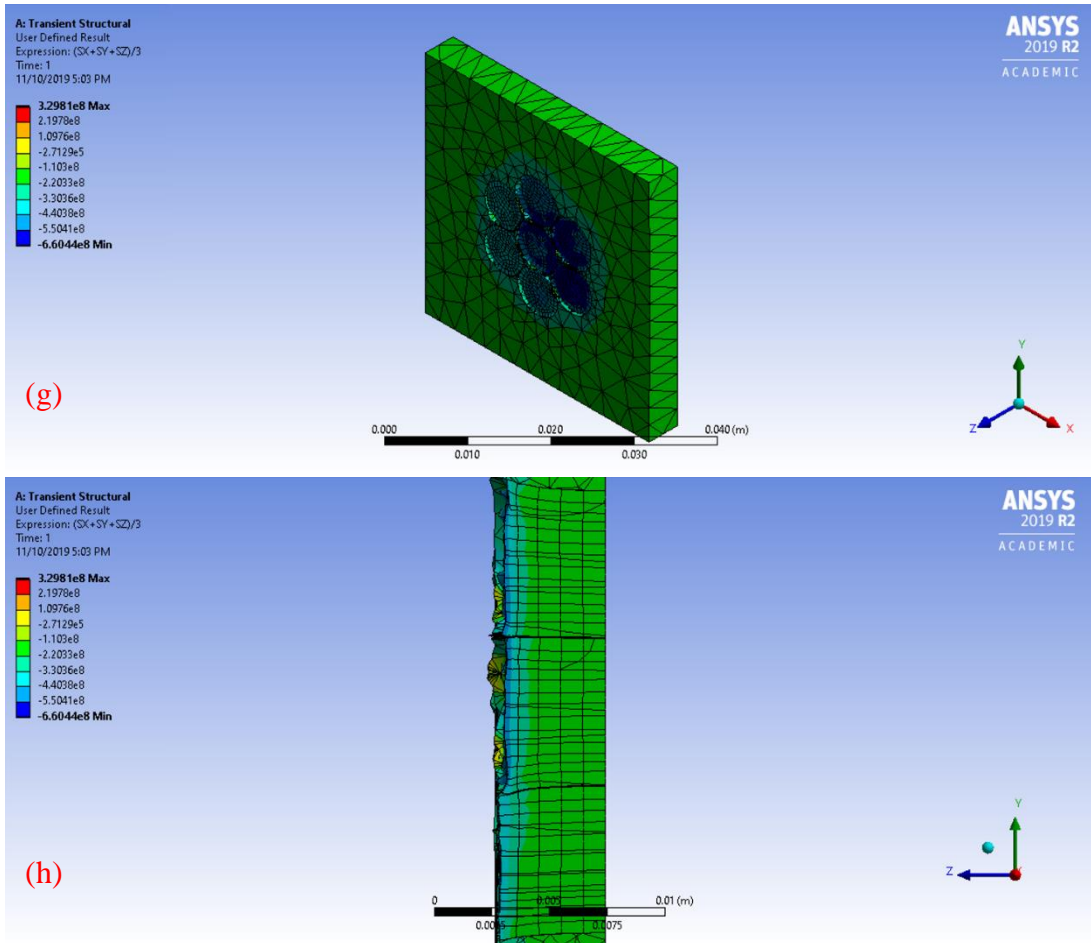


Figure 46. FEM results for Step 4 unloading condition. (a) Z direction displacement, (b) Z direction displacement section view, (c) Z strain, (d) Z strain section view, (e) von-Mises stress, (f) von-Mises stress section view, (g) Hydrostatic stress, and (h) Hydrostatic stress section view.

○ 4.3.5. Summary of All FEM Results

Table 24. FEM results for all steps loading and unloading conditions.

Step 1 Loading Condition		
	Tensile	Compressive
Z Displacement	0.32622 μm	-1.1876 μm
Z Stress	93.406 MPa	-467.24 MPa
Z Strain	$8.9320 \times 10^{-4} \frac{m}{m}$	$-4.4457 \times 10^{-3} \frac{m}{m}$
von-Mises Stress	237.68 MPa	

Step 1 Unloading Condition		
	Tensile	Compressive
Z Displacement	$2.1673 \times 10^{-5} \mu m$	$-1.6457 \times 10^{-5} \mu m$
Z Strain	$5.7103 \times 10^{-8} \frac{m}{m}$	$-4.4058 \times 10^{-8} \frac{m}{m}$
von-Mises Stress	0.019106 MPa	

Step 1		
Depth of Stress Beyond the Proportional Limit	N/A (von-Mises stress did not exceed the proportional limit)	
Depth of Residual Stress	0.354 mm	
Residual Stress	Tensile Stress	0.0046751 MPa (Max)
	Compressive Stress	-0.0041163 MPa (Min)

Step 2 Loading Condition		
	Tensile	Compressive
Z Displacement	0.83885 μm	-3.6556 μm
Z Stress	273.48 MPa	-874.10 MPa
Z Strain	$3.0856 \times 10^{-3} \frac{m}{m}$	$-7.8037 \times 10^{-3} \frac{m}{m}$
von-Mises Stress	425.93 MPa	

Step 2 Unloading Condition		
	Tensile	Compressive
Z Displacement	0.38634 μm	-1.5645 μm
Z Strain	$1.1902 \times 10^{-3} \frac{m}{m}$	$-9.7193 \times 10^{-4} \frac{m}{m}$
von-Mises Stress	173.96 MPa	

Step 2		
Depth of Stress Beyond the Proportional Limit	1.417 mm	
Depth of Residual Stress	0.628 mm	
Residual Stress	Tensile Stress	94.108 MPa (Max)
	Compressive Stress	-77.998 MPa (Min)

Step 3 Loading Condition		
	Tensile	Compressive
Z Displacement	0.87270 μm	-3.9289 μm
Z Stress	275.24 MPa	-874.10 MPa
Z Strain	$3.0870 \times 10^{-3} \frac{m}{m}$	$-7.8037 \times 10^{-3} \frac{m}{m}$
von-Mises Stress	436.62 MPa	

Step 3 Unloading Condition		
	Tensile	Compressive
Z Displacement	0.51369 μm	-1.5886 μm
Z Strain	$2.0613 \times 10^{-3} \frac{m}{m}$	$-1.2576 \times 10^{-3} \frac{m}{m}$
von-Mises Stress	217.23 MPa	

Step 3		
Depth of Stress Beyond the Proportional Limit	1.788 mm	
Depth of Residual Stress	0.653 mm	
Residual Stress	Tensile Stress	173.30 MPa (Max)
	Compressive Stress	-101.68 MPa (Min)

Step 4 Loading Condition		
	Tensile	Compressive
Z Displacement	1.2351 μm	-8.2997 μm
Z Stress	407.59 MPa	-874.10 MPa
Z Strain	$4.3823 \times 10^{-3} \frac{m}{m}$	$-7.8037 \times 10^{-3} \frac{m}{m}$
Hydrostatic Stress	268.29 MPa	-660.44 MPa
von-Mises Stress	436.62 MPa	

Step 4 Unloading Condition		
	Tensile	Compressive
Z Displacement	1.5692 μm	-5.1740 μm
Z Strain	$1.9183 \times 10^{-3} \frac{m}{m}$	$-1.6108 \times 10^{-3} \frac{m}{m}$
Hydrostatic Stress	86.598 MPa	-75.800 MPa
von-Mises Stress	224.56 MPa	

Step 4		
Depth of Stress Beyond the Proportional Limit	1.821 mm	
Depth of Residual Stress	1.656 mm	
Residual Stress	Tensile Stress	162.77 MPa (Max)
	Compressive Stress	-116.08 MPa (Min)

Chapter 5: Discussion

This chapter discusses the effect of laser shock peening process on AA5083-H116 microstructure changes, dislocation behaviors, and $\text{Al}_3\text{Mg}_2 \beta$ phase formation based on the results obtained and observed in the previous chapters. Every result and data point provided valuable details to show the changes made by laser shock peening on AA5083-H116. This chapter is divided into three main sections that cover the discussion of the results from light optical microscopy, transmission electron microscopy (TEM), and finite element method (FEM) modeling.

- 5.1. Optical Microscopy

The results gathered from optical microscope can be summarized into four main points. First, the precipitation of $\text{Al}_3\text{Mg}_2 \beta$ phase increases as the aging temperature increases under the same aging time. Second, the precipitation of $\text{Al}_3\text{Mg}_2 \beta$ phase increases as the aging time increases with the same aging temperature. Third, small amount of $\text{Al}_3\text{Mg}_2 \beta$ phase was already formed in the system. Last, the grain size near the surfaces is smaller as compared to the grain size in the middle of the sample. In order to show the changes made by the laser shock peening process, there are a total of nine pairs of laser shock peened and unpeened samples subjected to the same aging temperature and time. Based on the results shown in Figure 9 – 15, there are no significant changes observed between laser shock peened and unpeened samples. All the four main points summarized from observing microstructure images happened in both laser shock peened and unpeened samples. If only based on the comparison between laser shock peened and unpeened sample light optical microscope images, it

is very difficult to conclude that there are any changes caused by laser shock peening process. However, the maximum useful magnification of a light optical microscope is 1000x, and the changes caused by the laser shock peening process are more observable in the nanometer scale. Therefore, TEM analysis was performed and changes are observed in the TEM images, which is discussed in the next section.

- 5.2. Transmission Electron Microscopy

The TEM images show a clear difference between unaged laser shock peened and unpeened samples, where some phenomena are observed in one type of sample but not on the other sample. This indicates that the changes caused by laser shock peening are at the nanometer scale, which is unlikely to be observable in the optical microscope. This TEM discussion section is further separated into three sections, where each section discusses and analyzes three main changes caused by laser shock peening process observed from the TEM images.

- *5.2.1. Thermal Effect from Laser Shock Peening Process*

It has been observed that there are melt pools consistently appearing on the surface of the laser shock peened sample that did not undergo any artificial aging process. The TEM image of melt pool on the unaged laser shock peened sample can be seen in Figure 20. The melt pools appear on the sample surface imply that the laser shock peening process still generated enough heat to create localized melting on AA5083-H116 surface ($T_{\text{melt}} \sim 591^{\circ}\text{C}$ to 638°C) [11]. With the TEM image showing the appearance of melt pools, the sample near the laser shock peening surface must be

thermally affected. This could lead to the increased diffusivity of atoms and material properties change.

○ 5.2.2. Al_3Mg_2 β Phase Precipitates

Through the TEM analysis, the fine precipitations near and on the dislocations were suspected to be Al_3Mg_2 β phase in the laser shock peened sample, shown in Figure 19(b). With localized melting generated during the laser shock peening process, sample surface experienced a temperature gradient. Higher temperature near the melt pool center and lower temperature away from the melt pool center. Thus, some thermally affected regions experienced a temperature that is above the solvus temperature, and some regions experienced a temperature that is below the solvus temperature. The thermally affected regions that with a temperature that is below the solvus temperature could promote the diffusion and segregation of Mg atoms to the nearest preferential sites and allow the precipitation of Al_3Mg_2 β phase.

The Mg enrichment and segregation preferential site for the unaged laser shock peened sample is at the dislocation as these phenomena could possibly be explained by the following reasons. First, even though the laser pulse from laser shock peening process provides sufficient thermal energy for atomic diffusion, the duration time of each laser pulse is too short for atoms to diffuse in a long distance. The atomic diffusion time is limited by the laser pulse duration time, which only allows Mg atoms to diffuse in a short range to the nearest site that has enough segregation energy. Second, according to C. Hin et al., a dislocation has an equivalent segregation energy to a grain boundary to permit solute enrichment and segregation [68]. Dislocation cores have a naturally disordered structures that give the same segregation energy as a grain

boundary and allow Mg atoms to diffuse and segregate at a dislocation in a short amount of time. Moreover, many studies have shown that a supersaturated solute will segregate and enrich preferentially at dislocation [68 – 73]. The segregation and enrichment of Mg at the dislocation site has a very high possibility that led to the precipitation of $\text{Al}_3\text{Mg}_2 \beta$ phase. As pointed out in Chapter 2 Section 2.5 and Section 2.6, Magnesium segregation and enrichment has been highly suspected to be associated with the formation of $\text{Al}_3\text{Mg}_2 \beta$ phase, but the actual kinetics behind the nucleation and precipitation of $\text{Al}_3\text{Mg}_2 \beta$ phase still requires further research. Lastly, the precipitation of $\text{Al}_3\text{Mg}_2 \beta$ phase can help release some of the strain energy between dislocation and lattice. Dislocations create distortion in the lattice causing strain energy to increase. When the misfitted $\text{Al}_3\text{Mg}_2 \beta$ phase precipitate forms on and/or near the dislocation, part of the distortion strain energy can be reduced with the misfitted precipitates [68, 72, 73]. The actual kinetics and phases involved with the precipitations near and on the dislocations require further investigation and understanding to verify.

- *5.2.3. Dislocation Morphology*

From TEM analysis, there are differences in the dislocation configuration and dislocation density between the unaged laser shock peened and unpeened samples. In Figure 17 and 18, the unaged laser shock peened sample has a preferential orientation for the dislocation lines as compared to the randomly orientated dislocations in the unaged, no laser shock peened sample. The preferred dislocation line direction in the laser shock peened sample could be caused by the plastic deformation generated during the laser shock peening process. During the deformation process, dislocations slip preferentially on a family of planes that contains the highest density of atoms and slip

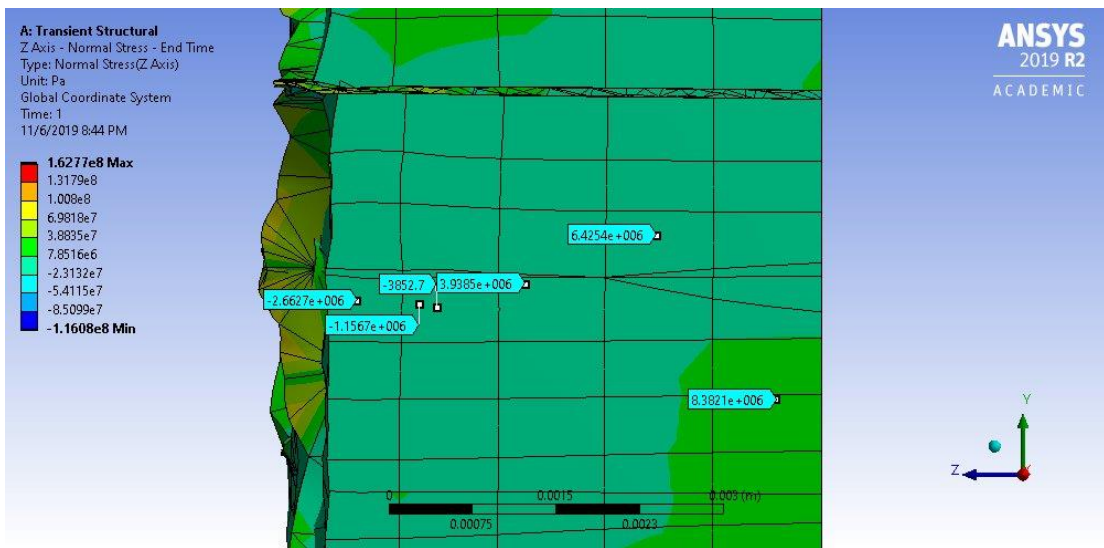
in the direction that has the most closely packed atoms [74]. Compared to the unaged, no laser peened sample, there is no clear dislocation orientation direction due to no additional plastic deformation from the laser shock peening process on the sample. Additionally, laser shock peening process introduced more dislocations near the sample surface as the laser pulse plastically deformed the sample surface. When the high energy laser pulse strikes the sample surface, large distortion of lattice is created and allow dislocations to create. The strength of impact stress that exceeds the yield strength of a material has an increasing relationship with the amount of dislocations generated in the system. In Chapter 3 Section 3.5.8., unaged laser shock peened sample shows a growth in dislocation density compared to unaged, no laser shock peened sample.

- 5.3. Finite Element Method Modeling

The finite element method (FEM) modeling performed in Chapter 4 shows plastic deformation did occur during the laser shock peening process, and it has been confirmed by TEM analysis. As the ANSYS Workbench 19.2 software simulated the impact force of the laser pulse on the sample surface, the stress created on the sample surface exceeded the proportional limit of AA5083-H116 ($2.75 \times 10^8 Pa$). This indicates that the sample surface is being plastically deformed by the laser shock peening process. The FEM model shows an agreement with the plastic deformation characteristic that is observable with the naked eye on the sample surface. Moreover, the FEM results were further confirmed by the TEM analysis on dislocation density and morphology. The agreement and confirmation by material microscopy

characterization allows the FEM simulation to be used as a prediction on material deformation behavior with a given amount of laser beam intensity.

The FEM results also calculated the amount of residual stress left in the sample and the depth of the residual stress. There are both tensile residual stresses (Max 162.77MPa) and compressive residual stresses (Min -116.08MPa) left in the sample after the laser shock peening process. The depth of the compressive residual stress from the laser shock peening surface is about 1.388mm, and the depth of the tensile residual stress is about 3.382mm. Figure 47 shows the transition from residual compressive stress in the sample surface to residual tensile stress in the sample bulk.



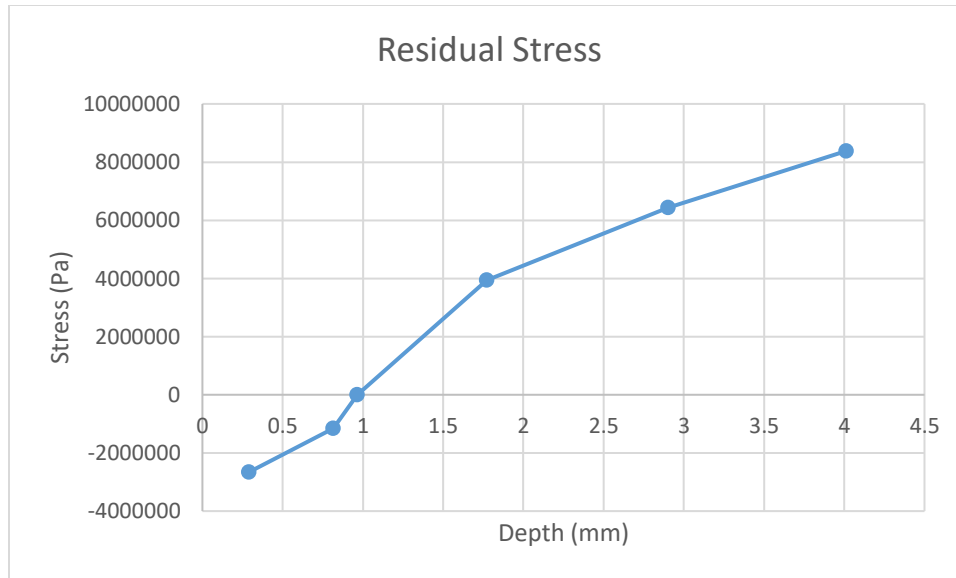
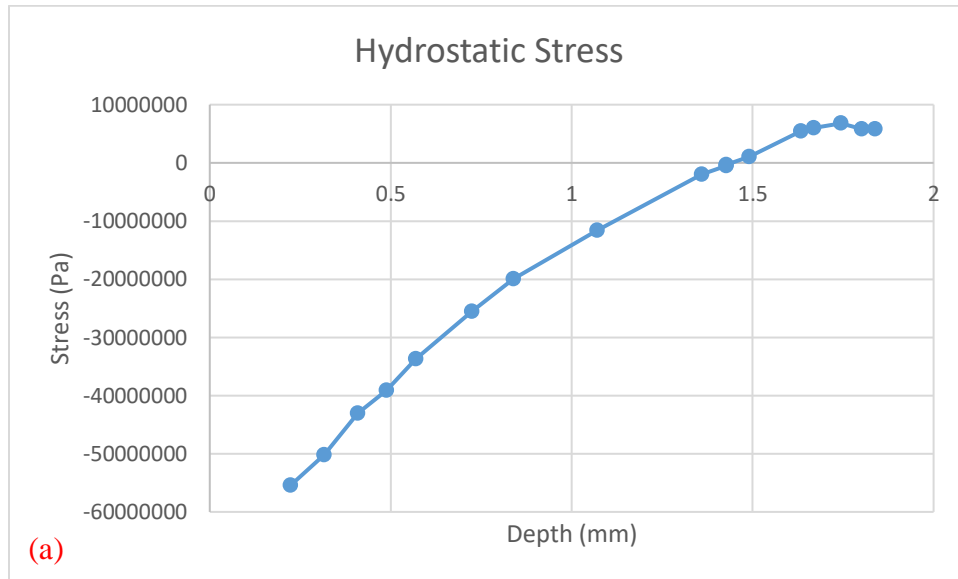


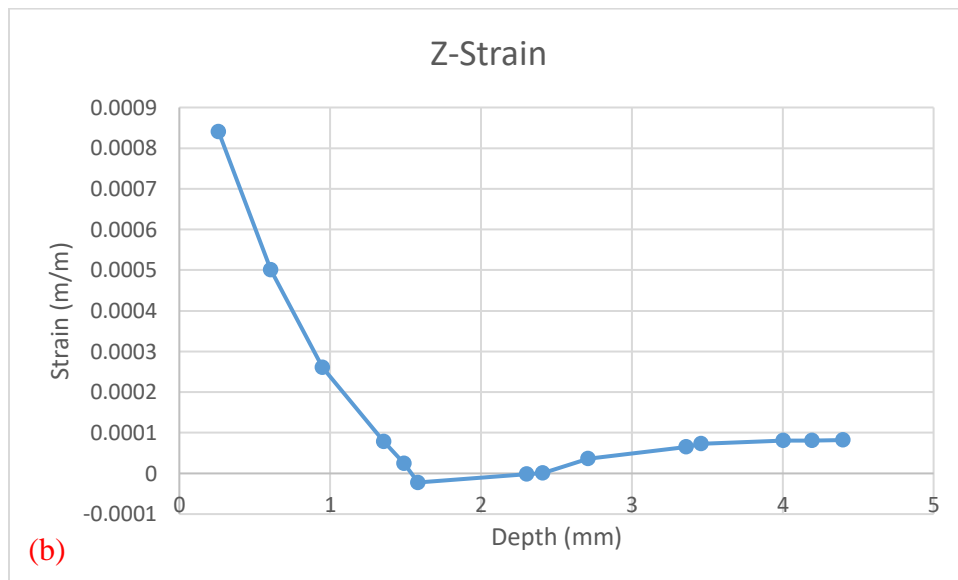
Figure 47. Tensile and compressive residual stress distribution.

The appearance of both compressive and tensile residual stress is due to the interaction between plastic and elastic deformation. During the laser shock peening process, the stress the sample experiences increases gradually during the force loaded condition, then the stress decreases after the force is removed. Only for a portion of the time during the laser shock peening process does the sample experience a stress that is greater than the material's proportional limit. This causes some parts of the sample to be permanently deformed. Since some regions experienced plastic deformation and other regions experienced elastic deformation, the tensile and compressive residual stresses are formed due to the interaction between plastic and elastic deformation. When the load is removed from the sample, the elastic regions of the sample tried to come back to its original shape, but the plastic regions constrained the movement of the material. Thus, tensile residual stress seems to be near the middle toward the end of the sample depth as the sample was more plastically deformed around that region. Additionally,

the phenomenon of the interaction between elastic and plastic deformation also has similar effect on the hydrostatic stress, Z direction strain, and von-Mises stress, shown in Figure 48 (a), (b), and (c).



(a)



(b)

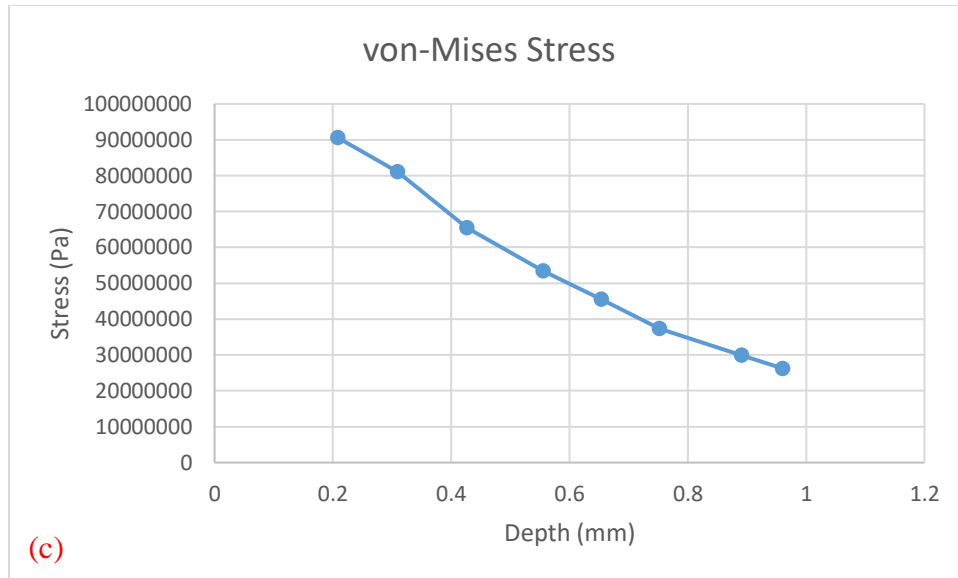


Figure 48. Graphical representations of (a) hydrostatic stress, (b) Z-direction strain, and (c) von-Mises stress changed through the sample thickness with the elastic and plastic deformation interaction.

Chapter 6: Conclusions

- 6.1. Summary and Conclusions

This research explores the effect of laser shock peening process on AA5083-H116 with a focus on the microstructural evolution and dislocation morphology changes. As the detrimental problems of sensitization of $\text{Al}_3\text{Mg}_2 \beta$ phase along grain boundaries and stress corrosion cracking of the 5xxx series aluminum have drawn a great amount of concerns, the main goals of this research is to provide results and data on the effectiveness of laser shock peening on AA5083-H116 and allow the results to be used in the future studies on whether or not the laser shock peening process helps to prevent and reduce $\text{Al}_3\text{Mg}_2 \beta$ phase sensitization and stress corrosion cracking.

Within this research, a total of 28 samples were being evaluated on the effect and alteration on AA5083-H116 caused by the laser shock peening process. The testing samples can be categorized into laser shock peened samples and no laser shock peened sample. There are 18 samples laser shock peened and 10 no laser shock peened samples. During the artificial aging process, 17 laser shock peened samples and 9 no laser shock peened samples were aged to cause sensitization of the $\text{Al}_3\text{Mg}_2 \beta$ phase. A laser shock peened and unpeened sample were unaged to allow for the direct comparison of laser shock peening on the material. The artificial aging process aged the samples in four different temperatures (70°C, 100°C, 150°C, and 175°C) with a range of aging times. After the aging process, the sample were characterized with light optical microscopy and a few selective samples were analyzed with transmission electron microscope (TEM). Grain size measurements (ASTM E112) and dislocation density

measurements were later performed to validate the phenomena observed in light optical microscopy images and TEM images. The laser shock peening process was simulated using the finite element method (FEM), which provided supplementary data to further understand the results gathered from light optical microscopy images and TEM images. In addition, the FEM model gave predictions on material mechanical behaviors with various changes in the laser pulse energy intensity.

Based on the results presented in Chapter 3 and Chapter 4 and the analysis performed in Chapter 5, several important conclusions and possible explanations can be drawn, and are listed below:

1. The observation through optical microscope, both laser shock peened and unpeened samples experienced the similar effects with different aging processes. The precipitation of $\text{Al}_3\text{Mg}_2 \beta$ phase increases as the aging temperature and time increases. Furthermore, prior to the sensitization aging process, both types of samples have pre-existing $\text{Al}_3\text{Mg}_2 \beta$ phase presented in the microstructure. All samples experienced the same grain size variation within the sample: a small grain size near the surface and a larger grain size in the middle of the sample.
2. As the optical microscopy image analysis did not show any differences between laser shock peened and unpeened samples, it can be concluded that the most observable laser shock peening effects are at a nanometer scale and higher-magnification techniques, such as TEM, are required to observe changes.

3. At the nanometer scale, several effects caused by laser shock peening process are observed. In the unaged laser shock peened sample, melt spots formed consistently across the sample surface. Melt spots were created from the high energy intensity laser beam during the laser shock peening process. This occurs despite the fact that the laser shock peening process is a cold work process and the water and black opaque overlays are applied on the sample surface to prevent any thermal effects and alterations. If localized melting is occurring, the thermal energy generated during each laser pulse would increase the atomic diffusivity.
4. With the thermal energy introduced to the sample surface by the laser shock peening process and increased atomic diffusion, fine precipitations were observed near and on the dislocations. This is only observed in the unaged laser shock peened sample. The fine precipitations were suspected to be Al_3Mg_2 β phase, and further analysis is required to confirm the identity of those fine precipitations. The phenomena of fine precipitations observed near and on the dislocations could possibly be explained by the following reasons.
 - Due to the naturally disordered structure of dislocation cores, the segregation energy of dislocation is the same as grain boundary, which allows segregation and enrichment of Mg atoms at dislocations.
 - It is highly suspected that the precipitation of Al_3Mg_2 β phase at dislocations is caused by the enrichment of Mg atoms at

dislocations. The actual kinetics of Al_3Mg_3 beta phase nucleation and formation are still under debate.

- Additionally, the precipitation of misfitted Al_3Mg_2 β phase around dislocation helps to reduce the distortion strain energy caused by dislocation formation, reducing the energy of nucleation.
5. For the laser shock peened sample, the dislocation density increased, and the dislocation lines are all orientated in a preferential direction. The increase in dislocation density and preferential direction of dislocation lines is created by the plastic deformation process from laser shock peening, and dislocations will slip on a close-packed plane and in close-packed direction.
 6. The FEM model confirms during the laser shock peening process, the sample surface is being plastically deformed by the high energy laser pulse. The stress generated at the sample surface exceeds the proportional limit of the material and created both tensile and compressive residual stresses. The creation of both tensile and compressive residual stresses is due to the interaction between plastic and elastic deformation. The plastic deformed region inhibits the elastic region to elastically recover to material's original shape, which creates tensile and compressive residual stresses within the material after the laser shock peening process.

- 6.2. Future Works

This research focused on the effect of laser shock peening process on samples that have either been artificially aged first or unaged at all. The results and conclusions provide better understanding of the effect of laser shock peening process on AA5083-H116 microstructural evolution and dislocation morphology changes, and can also be beneficial for applications that want to use the laser shock peened 5xxx series aluminum alloys as structural material. The study of the laser shock peening process on 5xxx series aluminum alloys can be further expanded by conducting a reverse heat treatment and laser shock peening process of this research and performing corrosion testing such as stress corrosion cracking (SCC) test, to observe the effect of laser shock peening process on material SCC resistance. Therefore, the future works of this project are suggested in the following:

1. Perform a reverse heat treatment and laser shock peening process, where the as-received 5xxx series aluminum alloys sample is first artificially aged to create $Al_3Mg_2 \beta$ phase. Next, apply laser shock peening process to the sample. Conduct the same material characterizations with light optical microscopy and TEM. Compare the results to see any changes between testing sequences.
2. As intergranular stress corrosion cracking (IGSCC) is a major concern with the 5xxx series aluminum alloys, it would be worthwhile to perform a stress corrosion cracking (SCC) sea water immersion test and understand the effect of laser shock peening process on material's corrosion and intergranular corrosion properties. The SCC sea water immersion test

should perform on both kinds of heat treatment and laser shock peening sequences. First sequence, laser shock peened the sample then age. Second sequence, aged the sample prior to laser shock peening process.

3. For future FEM study, additional variables can be applied onto the FEM model, such as the thermal effect caused by laser shock peening and the effect of water and black opaque overlays on sample. With such additional variables, the FEM model can provide a more detailed insight on the sample's mechanical properties. Moreover, besides creating an as-received aluminum sample FEM model, a FEM model with both aluminum matrix and Al_3Mg_2 β phase precipitates will provide more understanding on sensitized materials.
4. For TEM analysis, a complete analysis and phase identification of the fine precipitations near and on the dislocations observed in this project should be performed and further understand the kinetic phenomena behind the precipitations and the preferred precipitation locations.
5. Investigate whether the fine precipitations observed near and on the dislocations are detrimental to the material.
6. Perform TEM analysis on the aged laser shock peened and unpeened samples to observe the effect of laser shock peening process.

Chapter 7: References

- [1] J. Gilbert Kaufman, "Introduction to Aluminum Alloys and Tempers," *ASM International*, 2000.
- [2] N. A. Oguocha, O. J. Adigun, and S. Yannacopoulos, "Effect of Sensitization Heat Treatment on Properties of Al-Mg Alloy AA5083-H116," *Journal of Materials Science*, vol. 43, no. 12, pp. 4208-4214, Jun. 2008.
- [3] Ronald L. Holtz, Peter S. Pao, Robert A. Bayles, Thomas M. Longazel, and Ramasis Goswami, "Corrosion-Fatigue Behavior of Aluminum Alloy 5083-H131 Sensitized at 448K," *Metallurgical and Materials Transactions A*, vol. 43, no. 8, pp. 2839-2849, Aug. 2012.
- [4] Alton J. Banks, "Aluminum: What's the Use?" *Journal of Chemical Education*, vol. 69, no. 1, pp. 18, Jan 1992.
- [5] F.C. Campbell, "Elements of Metallurgy and Engineering Alloys," *ASM International*, pp. 487-508, 2008.
- [6] Sharma, Mala M., and Ziemian, Constance W., "Pitting and Stress Corrosion Cracking Susceptibility of Nanostructured Al-Mg Alloys in Natural and Artificial Environments," *Journal of Materials Engineering and Performance*, vol. 17, no. 6, pp. 870-878, Dec 2008.
- [7] A. V. Mikhailovskaya, I. S. Golovin, A. A. Zaitseva, V. K. Portnoi, P. Dröttboom, and J. Cifre, "Effect of Mn and Cr additions on kinetics of recrystallization and parameters of grain-boundary relaxation of Al-4.9Mg alloy," *The Physics of Metals and Metallography*, vol. 114, no. 3, pp. 246-255, Jul 2012.
- [8] Atlas Steels, "Aluminum Alloy Data Sheet 5083," *Atlas Steels*, pp. 1-3, Oct 2013.
- [9] N. A. Oguocha, O. J. Adigun, and S. Yannacopoulos, "Effect of Sensitization Heat Treatment on Properties of Al-Mg Alloy AA5083-H116," *Journal of Materials Science*, vol. 43, no. 12, pp. 4208-4214, Jun 2008.
- [10] Ronald L. Holtz, Peter S. Pao, Robert A. Bayles, Thomas M. Longazel, and Ramasis Goswami, "Corrosion-Fatigue Behavior of Aluminum Alloy 5083-H131 Sensitized at 448K," *Metallurgical and Materials Transactions A*, vol. 43, no. 8, pp. 2839-2849, Aug 2012.
- [11] ASM Aerospace Space Specification Metals Inc., "Aluminum 5083-H116; 5083-H321," *ASM Aerospace Space Specification Metals Inc.*, 2019.
- [12] R. Zhang, S.P. Knight, R.L. Holtz, R. Goswami, C.H.J. Davies, and N. Birbilis. "A Survey of Sensitization in 5xxx Series Aluminum Alloys." *Corrosion*, 72 (2016)
- [13] R. H. Jones, D. R. Baer, M. J. Danielson, and J. S. Vetrano. "Role of Mg in the Stress Corrosion Cracking of an Al-Mg Alloy." *Metallurgical and Materials Transactions A*, 32A (2001) 1699-1711.

- [14] Ramasis Goswami and Ronald L. Holtz, "Transmission Electron Microscopic Investigations of Grain Boundary Beta Phase Precipitation in Al 5083 Aged at 373K," *Metallurgical and Materials Transactions A*, vol. 44, no. 3, pp. 1279-1289, Mar 2013.
- [15] J. L. Searles, P. I. Gouma, and R. G. Buchheit, "Stress Corrosion Cracking of Sensitized AA5083," *Metallurgical and Materials Transactions A*, vol. 32, no. 11, pp. 2859-2867, Nov 2001.
- [16] Ronald L. Holtz, Peter S. Pao, Robert A. Bayles, and Thomas M. Longazel, "Corrosion Fatigue of Al 5083-H131 Sensitized at 70, 100, and 175°C and Relation to Microstructure and Degree of Sensitization," *Metallurgical and Materials Transactions A*, vol. 43, no. 8, pp. 1-11, Aug 2011.
- [17] R. Goswami, G. Spanos, P. S. Pao, and R.L. Holtz, "Microstructural Evolution and Stress Corrosion Cracking Behavior of Al-5083," *Metallurgical and Materials Transactions A*, vol. 42, no. 2, pp. 348-355 Feb 2011.
- [18] Ying-Kai Lin, Shing-Hai Wang, Ren-Yu Chen, Tso-Sheng Hsieh, Liren Tsai, and Chia-Chin Chiang, "The Effect of Heat Treatment on the Sensitized Corrosion of the 5383-H116 Al Mg Alloy," *Materials*, vol. 10, no. 3, pp. 1-9, Mar 9.
- [19] Yakun Zhu, "Characterization of Beta Phase Growth and Experimental Validation of Long-Term Thermal Exposure Sensitization of AA5XXX Alloys," Master's Thesis, The University of Utah, Salt Lake City, Utah, 2013.
- [20] J. C. Chang and T. H. Chuang, "Stress-Corrosion Cracking Susceptibility of the Superplastically Formed 5083 Aluminum Alloy in 3.5 Pct NaCl Solution," *Metallurgical and Materials Transactions A*, vol. 30, no. 12, pp. 3191-3199, Dec 1999.
- [21] R. H. Jones. "The Influence of Hydrogen on the Stress-Corrosion Cracking of Low Strength Al-Mg Alloys." *JOM*, vol. 55, no. 2, pp. 42-46, Feb 2003.
- [22] R.K. Gupta, R. Zhang, C.H.J. Davies, and N. Birbilis, "Influence of Mg Content on the Sensitization and Corrosion of Al-xMg(-Mn) Alloys," *Corrosion*, vol. 69, no. 11, pp. 1081-1087, Nov 2013.
- [23] R.H. Jones, D.R. Baer, M.J. Danielson, and J.S. Vetrano, "Role of Mg in The Stress Corrosion Cracking of an Al-Mg Alloy," *Metallurgical and Materials Transactions A*, vol. 32A, pp. 1699-1711, Jul 2001.
- [24] R. Goswami, G. Spanos, P.S. Pao, and R.L. Holtz, "Precipitation Behavior of the β phase in Al-5083," *Materials Science and Engineering A*, vol. 527, no. 4-5, pp. 1089-1095, Feb 2010.
- [25] R. Zhang, S.P. Knight, R.L. Holtz, R. Goswami, C.H.J. Davies, and N. Birbilis, "A Survey of Sensitization in 5xxx Series Aluminum Alloys," *Corrosion*, vol. 72, no. 2, pp. 144-159, Feb 2016.
- [26] Ramasis Goswami and Ronald L. Holtz, "Transmission Electron Microscopic Investigations of Grain Boundary Beta Phase Precipitation in Al 5083 Aged at

- 373K,” *Metallurgical and Materials Transactions A*, vol. 44, no. 3, pp. 1279-1289, Mar 2013.
- [27] J. L. Searles, P. I. Gouma, and R. G. Buchheit, “Stress Corrosion Cracking of Sensitized AA5083,” *Metallurgical and Materials Transactions A*, vol. 32, no. 11, pp. 2859-2867, Nov 2001.
- [28] Ronald L. Holtz, Peter S. Pao, Robert A. Bayles, and Thomas M. Longazel, “Corrosion Fatigue of Al 5083-H131 Sensitized at 70, 100, and 175°C and Relation to Microstructure and Degree of Sensitization,” *Naval Research Laboratory*, pp. 1-11, 2011.
- [29] R. Goswami, G. Spanos, P. S. Pao, and R.L. Holtz, “Microstructural Evolution and Stress Corrosion Cracking Behavior of Al-5083,” *Metallurgical and Materials Transactions A*, vol. 42, no. 2, pp. 348-355 Feb 2011.
- [30] D.R. Harries and A.D. Marwick, “Non-equilibrium Segregation in Metals and Alloys,” *Phil. Tans. R. Soc.*, vol. 295, pp. 197-207, 1980.
- [31] J.B. Rellick and C.J. McMahon, “Intergranular Embrittlement of Iron-Carbon Alloys by Impurities,” *Metallurgical Transactions*, vol. 5, no. 11, pp. 2439-2450, Nov 1974.
- [32] M. de Hass and J.Th.M. De Hosson, “Grain Boundary Segregation and Precipitation in Aluminum Alloys,” *Scripta Mater.*, vol. 44, pp. 281-286, 2001.
- [33] J. S. Vetrano, R. E. Williford, S. M. Bruemmer, and R. H. Jones, “Influence of Microstructure and Thermal History on The Corrosion Susceptibility of AA5083,” *TMS Annual Meeting: Automotive Alloys*, 1997.
- [34] C. Lea and C. Molinari, “Magnesium Diffusion, Surface Segregation and Oxidation in Al-Mg Alloys,” *Journal of Materials Science*, vol. 19, no. 7, pp. 2336-2352, Jul 1984.
- [35] F.J. Esposito, C.S. Zhang, P.R. Norton, and R.s. Timsit, “Segregation of Mg to the Surface of an Al-Mg Single Crystal Alloy and Its Influence On the Initial Oxidation at Room Temperature,” *Surface Science*, vol. 302, no. 1-2, pp. 109-120, Jan 1994.
- [36] D. R. Baer, C. F. Windisch Jr., M. H. Engelhard, M. J. Danielson, R. H. Jones, and J. S. Vetrano, “Influence of Mg on the Corrosion of Al,” *Journal of Vacuum Science and Technology*, vol. 18, no. 1, pp. 131-136, Jan 2000.
- [37] R.H. Jones, D.R. Baer, M.J. Danielson, and J.S. Vetrano, “Role of Mg in the Stress Corrosion Cracking of an Al-Mg Alloy,” *Metallurgical and Materials Transactions A*, vol. 32A, pp. 1699-1711, Jul 2001.
- [38] I. N. A. Oguocha, O. J. Adigun, S. Yannacopoulos, “Effect of Sensitization Heat Treatment on Properties of Al-Mg Alloy AA5083-H116,” *Journal of Materials Science*, vol. 43, no. 12, pp. 4208-4214, Jun 2008.
- [39] Yusheng Ding, Kunyuan Gao, Hui Huang, Shengping Wen, Xiaolan Wu, Zuoren Nie, Shanshan Guo, Rui Shao, Cheng Huang and Dejing Zhou, “Nucleation and

- evolution of β phase and corresponding intergranular corrosion transition at 100–230 °C in 5083 alloy containing Er and Zr,” *Materials and Design*, vol. 174, no. 15, pp. 1-11, Jul 2019.
- [40] Baker H and Okamoto H, “Alloy phase diagrams,” *ASM International*, ASM Handbook, Ohio, pp. 501, 1992.
- [41] ASM Internation, “Heat Treating of Aluminum Alloys,” *ASM Handbook*, pp. 841-879, 1991.
- [42] M.J. Starink and A.M. Zahra, “The Kinetics of Isothermal β' Precipitation in Al-Mg Alloys,” *Journal of Materials Science*, vol. 34, pp.1117-1127, 1999.
- [43] Masahiro Kubota, “Identification of β Phase Particles in an Isothermally Aged Al-10mass% Mg-0.5mass% Ag Alloy,” *Materials Transactions*, vol. 46, no. 11, pp. 2437-2442, 2005.
- [44] Gaosong Yi, Yakun Zhu, David A. Cullen, Alexander T. Derrick, and Michael L. Free, “Precipitates in Long Term Aging Al 5083,” *TMS Light Metals*, Feb 2014.
- [45] P. van Mourik, N. M. Maaswinkel, Th. H. de Keijser, and E.J. Mittemeijer, “Precipitation in Liquid-Quenched Al-Mg Alloys; A Study Using X-Ray Diffraction Line Shift and Line Broadening,” *Journal of Materials Science*, vol. 24, no. 10, pp. 3779-3786, Oct 1989.
- [46] D. Hamana, L. Baziz, and M. Boucheur, “Kinetics and Mechanism of Formation and Transformation of Metastable β' -Phase in Al-Mg Alloys,” *Materials Chemistry and Physics*, vol. 84, no. 1, pp. 112-119, Mar 2004.
- [47] Yaya Zheng, Binghui Luo, Zhenhai Bai, Juan Wang, and Yuan Yin, “Study of the Precipitation Hardening Behavior and Intergranular Corrosion of Al-Mg-Si Alloys with Differing Si Contents,” *Metals*, vol. 7, no. 10, pp. 1-12, Sep 2017.
- [48] Hong He, Long Zhang, Shikang Li, Xiaodong Wu, Hui Zhang, and Luoxing Li, “Precipitation Stages and Reaction Kinetics of AlMgSi Alloys during the Artificial Aging Process Monitored by In-Situ Electrical Resistivity Measurement Method,” *Metals*, vol. 8, no. 1, pp. 1-12, Jan 2018.
- [49] J. Buczynski and R.G. Kelly, “Characterization of the Beta Phase in 5xxx Aluminum Alloys,” University of Virginia, pp. 1-5, Jun 2015.
- [50] M Bernole, J Raynal, and R Graf, “Structure and Orientation of Precipitates Appearing in Quenched Al-Mg Alloys with 10 pct Magnesium,” *J. Microsc*, vol. 8, pp. 831-840, 1969.
- [51] P. Peyre and R. Fabbro, “Laser Shock Processing: A Review of the Physics and Applications,” *Optical and Quantum Electronics*, vol. 27, pp. 1213-1239, 1995.
- [52] P. Peyre, A. Sollier, I. Chaieb, L. Berthe. E. Bartnicki, C. Braham, and R. Fabbro, “FEM Simulation of Residual Stresses Induced by Laser Peening,” *The European Physical Journal Applied Physics*, vol. 23 pp. 83 – 88, 2003.
- [53] J.Z. Lu, K.Y. Luo, D.K. Yang, X.N. Cheng, J.L. Hu, F.Z. Dai, H. Qi, L. Zhang, J.S. Zhong, Q.W. Wang, and Y.K. Zhang, “Effects of Laser Peening on Stress

- Corrosion Cracking of ANSI 304 Austenitic Stainless Steel,” *Corrosion Science*, vol. 60, pp. 145 – 152, 2012.
- [54] Kopeliovich Dmitri. “Laser Peening.” *Substances & Technologies*, 2013.
- [55] I.N. Shiganov, A.I. Misurov, D.M. Melnikov, “Laser Shock Peening of Welded Joints,” *Journal of Physics*, conf. series 1109, 2018.
- [56] E. Hoffman, “Metal Fatigue Improvement with Stress Waves,” *LSP Technologies*, Jan 2017 [57] Wu Wei. “Study of Sensitization in AA5083 Aluminum Alloy.” *University of Manchester*, Dissertation, (2017).
- [58] R. Zhang, S.P. Knight, R.L. Holtz, R. Goswami, C.H.J. Davies, and N. Birbilis, “A Survey of Sensitization in 5xxx Series Aluminum Alloys,” *Corrosion*, vol. 72, 2016.
- [59] Ronald L. Holtz, Peter S. Pao, Robert A. Bayles, and Thomas M. Longazel, “Corrosion Fatigue of Al 5083-H131 Sensitized at 70, 100, and 175°C and Relation to Microstructure and Degree of Sensitization,” *Naval Research Laboratory*, pp. 1-11, 2011.
- [60] Ramasis Goswami and Ronald L. Holtz. “Transmission Electron Microscopic Investigations of Grain Boundary Beta Phase Precipitation in Al 5083 Aged at 373K.” *Metallurgical and Materials Transactions A*, vol. 44, pp. 1279-1289, 2013.
- [61] J. L. Searles, P. I. Gouma, and R. G. Buchheit. “Stress Corrosion Cracking of Sensitized AA5083.” *Metallurgical and Materials Transactions A*, vol. 32A, pp. 2859-2867, 2001.
- [62] R. Goswami, G. Spanos, P. S. Pao, and R.L. Holtz, “Microstructural Evolution and Stress Corrosion Cracking Behavior of Al-5083,” *Metallurgical and Materials Transactions A*, vol. 42A, pp. 348-355, 2011.
- [63] S. Iric and A.O. Ayhan, “Dependence of Fracture Toughness on Rolling Direction in Aluminum 7075 alloys,” *Acta Physica Polonica A*, vol. 132, no. 3-II, pp. 892-895, 2017.
- [64] Kangsik Kim, Jongyoung Lee, Hyojin Kim, and Zonghoon Lee, “Quantitative Evaluation of Dislocation Density in Epitaxial GaAs Layer on Si Using Transmission Electron Microscopy,” *Applied Microscopy*, vol. 44, no. 2, pp. 74-78, Jun 2014.
- [65] S. Morito, J. Nishikawa, T. Maki, “Dislocation Density within Lath Martensite in Fe-C and Fe-Ni Alloys,” *ISIJ International*, vol. 43, no. 9, pp. 1475-1477, 2003.
- [66] Patrick Summers, Brian Lattimer, and Scott Case, “Residual Constitutive Behavior of Aluminum Alloys after Fire Exposure,” *Fire Safety Science*, vol. 11, pp. 612-625, Jan 2014.
- [67] L. Berthe, R. Fabbro, P. Peyre, L. Tollier, and E. Bartnicki, “Shock Waves from a Water-Confined Laser-Generated Plasma,” *Journal of Applied Physics*, vol. 82, Jun 1997.

- [68] Heterogeneous precipitation on dislocations: effect of the elastic field on precipitate morphology
- [69] R. Bullough, R. C. Newman, J. Wakefield, and J. B. Willis, "Precipitation on a Dislocation," *Nature*, vol. 183, pp. 34-35, 1959.
- [70] F. Perrard, P. Donnadieu, A. Deschamps, and P. Barges, "TEM Study of NbC Heterogeneous Precipitation In Ferrite," *Journal of Philosophical Magazine*, vol. 86, no. 27, pp. 4271-4284, 2006.
- [71] Ichiro Yonenaga and Koji Sumino, Influence of Oxygen Precipitation Along Dislocations on the Strength of Silicon Crystals," *Journal of Applied Physics*, vol. 80, no. 2, pp. 734, 1996.
- [72] Frank S. Ham, "Stress-Assisted Precipitation on Dislocations," *Journal of Applied Physics*, vol. 30, no. 6, pp. 915, 1959.
- [73] C. Hin, Y. Brechet, P. Maugis, and F. Soisson, "Kinetics of Heterogeneous Dislocation Precipitation of NbC in Alpha-Iron," *Acta Materialia*, vol. 56, no. 19, pp. 5535-5543, Nov 2008.
- [74] Derek Hull and David Bacon, "Introduction to Dislocations," *Butterworth-Heinemann*, fifth Edition, Feb 2011.